Nonresonant Optical Nonlinearities In GaAs/AlGaAs Multiple Quantum Well Waveguides

by

Frances Ruth Laughton

September 1991

A Thesis submitted to the Faculty of Engineering of the University of Glasgow for the degree of Doctor of Philosophy

ACKNOWLEDGEMENTS

While it was at times hard to envisage an end to the work contained in this thesis, I have no doubt that one of the key factors in its completion was the encouragement I received from many different people in the department, and for that I am extremely grateful. I have been very fortunate to be able to count many of my colleagues also as friends, and I would like to mention particularly Karen McIlvaney, Mary O'Neill and Andy Jennings.

The excellent technical support in the department has been crucial, and I would like to thank Lois Hobbs for teaching me both photolithography and bridge! I am very grateful to Stewart Fairbairn of the Electronic Workshop and to Harry Anderson, George Thornton and the other staff in the Mechanical Workshop for deciphering my drawings and somehow managing to make the jobs up correctly! Thanks also to Dave Clifton, Dave Lawson and Ray Darkin, who put up patiently with my paranoid requests for just one more calibration run before dry etching my waveguides, to John Cochrane who took the photoluminescence spectra and to Dave Gourlay, who took the Scanning Electron Micrographs for me.

Over my years in the department, John Davies has given a superb set of lecture series on quantum mechanics, which greatly added to my understanding of the subject, and for which I am very grateful. Thanks also to Richard de la Rue for his advice and encouragement, and to Clivia Sotomayor-Torres and Stewart Aitchison for reading and constructively criticising parts of this thesis. I would like to thank Ray Hutchins for his concern for my welfare throughout my time in Glasgow, and for his interest in my progress.

I am grateful to Prof. J. Lamb for the use of the departmental facilities. Thanks are also due to BNR Europe Ltd (formerly STC Technology Ltd.) for my CASE sponsorship, and for the use of their facilities, and especially to Kevin Byron, my industrial supervisor, who has been very generous in lending us equipment. I am also very grateful to John Marsh, my departmental supervisor, who has always made time to see me, and has been unfailingly optimistic! His encouragement, interest and advice have been invaluable throughout my research and writing up this thesis.

Most of all, I have appreciated the support of my family. I would like to thank my husband, Mike, who has managed to live with me through the past four years, and who has been at various times a source of encouragement, a shoulder to cry on, a punch bag and someone with whom to celebrate! Thanks also to our parents, Stewart and Janet Darlow and Charles and Barbara Laughton, for their care and understanding.

TABLE OF CONTENTS

Chapter 3: Waveguide design and fabrication

Chapter 4: Experimental set-up

Chapter 5: Nonlinear absorption theoretical model

Chapter 6: Nonlinear absorption experiments and fitting to the theoretical model

Chapter 7: Nonlinear refractive index experiments

ABSTRACT

This thesis describes experiments performed to investigate nonlinear absorption and refractive index changes in GaAs/AlGaAs Multiple Quantum Well (MQW) waveguides. Nonlinear transmission experiments were first carried out with a single Nd^{3+}:YAG laser beam at 1.06 μm and, when the experiments were analysed, the TPA coefficient, β, was calculated to be 2.2×10^{-10} m W^{-1} for TM polarisation and 2.7×10^{-10} m W^{-1} for TE polarisation. This analysis to calculate β was done in the usual way of many studies of two-photon absorption (TPA) in semiconductors, that is neglecting the effect of free carrier absorption (FCA). An intuitive theoretical model was derived to include the effect of FCA in the waveguide and when the same nonlinear transmission experiments were analysed using this new model, β was found to be 1.3×10^{-10} m W^{-1} and 2.0×10^{-10} m W^{-1} for TM and TE polarisations respectively.

Pump-probe experiments have also been performed, and the change in probe transmission measured as a function of both pump intensity and pump-probe delay time. The results from these experiments can also be successfully fitted to the model. We have seen that, for relatively low peak pump input intensities of approximately 4.5×10^{11} Wm^{-2}, there is a 35% decrease in transmission of the probe beam when the pump beam is present and overlapping in time. TPA is generally considered to have a deleterious effect on the performance of nonlinear optical switches, but for this low peak pump input intensity the recovery time of this absorption modulation is limited only by the laser pulsewidth. At higher peak pump input intensities of about 1.5×10^{12} W m^{-2}, there is a 70% decrease in the transmission of the probe beam when the pump beam is present and overlapping in time, but the recovery time of the modulation is now much slower, as it is limited by the carrier lifetime.

Nonlinear refractive index measurements have been made at 1.06 μm using a time-division interferometer, and n_2 measured to be about -3×10^{-17} m^2W^{-1} for a TM pump and TE probe. When measured as a function of pump-probe delay time, the refractive index change is seen to contain a positive component when the pump and probe pulses are very close to each other in time, which corresponds to an intensity-dependent nonlinear refractive index of $n_2\approx2\times10^{-17}$ m^2W^{-1}.

CONTENT OF THE THESIS

Chapter One is an introduction to the thesis. It outlines the advantages of all-optical devices over their electronic counterparts for signal processing, with particular reference to modulators and switches. The various materials used for nonlinear waveguide devices are discussed and GaAs/AlGaAs Multiple Quantum Well (MQW) material introduced.

Chapter Two provides the theoretical background to the work. Linear absorption in bulk and MQW semiconductor material is described, and this is followed by an outline of the two-level atomic model, which is used as a basis for the introduction to all-optical nonlinearities involving both real and virtual transitions.

Chapter Three describes the processes involved in fabricating the waveguides used in this work, from the waveguide theory and numerical methods necessary to design the material to the material growth, photolithography and etching of the ribs.

Chapter Four is concerned with the laser system used and with the characterisation of the waveguides prior to any nonlinear optical experiments. An autocorrelation trace of the modelocked YAG laser pulses is given. The Peltier temperature controller on which the waveguides were mounted is described, as are the methods of sequential cleaving and Fabry-Pérot transmission used to measure the loss of the waveguides. It is shown how measurements of photoluminesence and of transmission near the excitonic resonances are used to assess material quality, and plots are shown for the material used.

Chapter Five derives an intuitive theoretical model for nonlinear absorption in a waveguide. This includes the effect of free carrier absorption as well as that of two-photon absorption, and the nonlinear absorption equations are solved for the cases of both a single beam propagating through a waveguide and also a pump-probe set-up.

Chapter Six presents the nonlinear absorption experiments in GaAs/AlGaAs MQW waveguides. Nonlinear absorption experiments were carried out both for a single beam and also for pump and probe beams, when the nonlinear absorption of the probe was measured as a function of both the pump-probe delay time and also the pump intensity. All the resulting graphs were fitted successfully to the theoretical model of Chapter Five.

Chapter Seven outlines the measurements of the nonlinear change in refractive index of the waveguides. The various improvements and modifications made to the Mach-Zehnder interferometer in order to make these measurements are described, and a time-resolved plot of the change in refractive index presented, which is fitted to theory.

Chapter Eight summarises the content and results of this thesis, discusses conclusions to be drawn from the nonlinear absorption and refractive index experiments and suggests directions for future work.

CHAPTER ONE
INTRODUCTION

"I have heard articulate speech produced by sunlight! I have heard a ray of the sun laugh and cough and sing!" enthused Alexander Graham Bell about his latest invention, the "photophone", made in 1880, just four years after the telephone. This encoded sound onto a beam of light, by reflecting sunlight from a mirror which vibrated in response to the voice. This light then travelled to the receiver, where it was detected, and converted back to sound. Despite the photophone never finding commercial use, Bell considered it the greatest of all his inventions.

At present, light is primarily used to carry information between the electronic systems which process the information, in a similar way to Bell's photophone. Even though optical fibre communication systems are used very extensively, the input and output signals are generally electrical. The electrical signal is encoded onto the light beam by a modulator at one end of an optical fibre, and then demodulated back to an electrical signal at the output (Fig. 1.1). However, the electronic components used for signal detection and processing are not fast enough to take advantage of the total available bandwidth of the optical fibre. All-optical signal processing has several advantages over electronic processing, in that it has the capability of a much higher processing speed, which implies a much greater achievable bandwidth than electronic circuits. There is also a capability for a high level of parallel processing by means of Wavelength or Time Division Multiplexing, which increases processing efficiency, and there are no problems of interaction between signals by electrical or magnetic coupling.

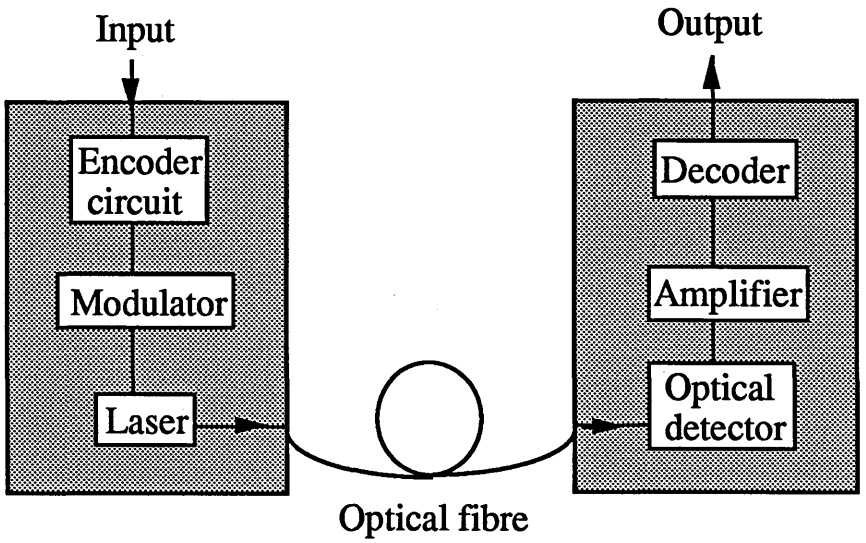

Fig. 1.1 Components of an optical fibre communication system

In order to carry out all-optical signal processing, optically-induced changes in certain properties of nonlinear materials, e.g. the absorption coefficient or refractive index, are necessary. This chapter will briefly outline the mechanisms by which light-induced changes occur in the optical properties of nonlinear materials. Two examples of nonlinear optical devices are discussed, and the most extensively used materials for nonlinear optical waveguide devices are reviewed and compared. The optical properties of semiconductor Multiple Quantum Well material are introduced and several examples given of successful devices already made using Multiple Quantum Wells.

1.1: NONLINEAR OPTICS NOTATION

It is assumed in linear optics that the optical properties of a material, for example its susceptibility, absorption coefficient and refractive index, remain constant when light falls on the material, and that the polarisation **P** of the medium is directly proportional to the optical electric field **E**. As **E** becomes more intense, however, this approximation becomes invalid. **P** is no longer linear with **E** and so the material's optical properties change as a function of the intensity of the light.

Provided that **P** is "small", **P(E)** may be expanded as a Taylor series:

$$P(E) = P(0) + \left(\frac{\delta P}{\delta E}\right)_{E=0} E + \frac{1}{2!}\left(\frac{\delta^2 P}{\delta E^2}\right)_{E=0} E^2 + ... \qquad (1.1)$$

The first term on the right hand side of this equation, the spontaneous polarisation, P(0), is zero for all materials except ferroelectrics. The second term is equal to $\varepsilon_0\chi^{(1)}$, the linear susceptibility, the third term is the second-order susceptibility, and so on. In general, when **P** and **E** are represented as vectors and the susceptibilities as tensors, the polarisation of the medium may be written as *(Miller 1981)*

$$P_i = \varepsilon_0 \chi^{(1)}_{ij} E_j + \chi^{(2)}_{ijk} E_j E_k + \chi^{(3)}_{ijkl} E_j E_k E_l + ... \qquad (1.2)$$

There are many nonlinear optical effects which have been observed in many different materials, and their relative strengths in each material are determined by the values of each nonlinear susceptibility $\chi^{(n)}$. Because the nonlinear susceptibilities $\chi^{(2)}$, $\chi^{(3)}$, etc. are much smaller than their linear counterpart $\chi^{(1)}$, nonlinear effects are not seen unless laser light is used. In order to observe a nonlinear response, an optical electric field is needed of the order of 1 kV/cm, corresponding to an intensity of about 2.5 kW/cm^2, to compensate for the small nonlinear susceptibility *(Shen 1984)*, and this intensity is generally only obtainable from lasers.

1.2: SECOND-ORDER NONLINEAR EFFECTS

The second-order nonlinear susceptibility, $\chi^{(2)}$, leads to effects such as second-harmonic generation, three wave mixing, optical rectification, parametric amplification and the Pockel's electro-optic effect. It is always zero in centrosymmetric crystals and non-crystalline materials such as glasses, liquids and gases. The reason for this can be understood by considering the centrosymmetric molecule shown in Fig. 1.2.

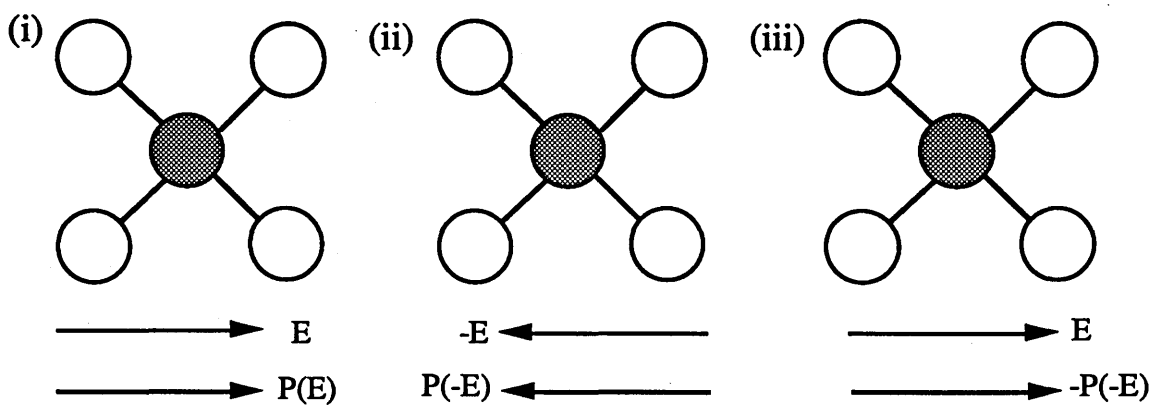

Fig. 1.2 Polarisation induced in a centrosymmetric molecule by an electric field

When an electric field is applied to this molecule, a polarisation is induced in the same direction as the field and when the direction of the electric field is reversed, the direction of the polarisation is also reversed. Because the molecule is centrosymmetric, the magnitude of the polarisation must be the same for either direction of the field, and so it may be seen from Fig. 1.2 that P(E)=-P(-E). Referring back to Eqn. 1.2, in order for this to be true, $\chi^{(2)}=0$.

In a linear medium, it may be imagined that the electric field of a light beam of frequency ω induces the electrons to behave as driven, damped harmonic oscillators, oscillating at frequency ω, so that the polarisation in the crystal is of this same frequency *(Dalven 1980)*. In a nonlinear medium with non-zero $\chi^{(2)}$, the frequency of the light beam mixes with itself due to the nonlinearity. Because of this, as well as a strong component in the polarisation at frequency ω, there are also two other weaker components induced, one at frequency 2ω and the other dc. This is the mechanism for second-harmonic generation and optical rectification. In the same way, a nonlinear medium can mix waves of different frequencies, so that if two light beams of frequencies ω_1 and ω_2 are incident on a nonlinear medium, the induced polarisation contains components at frequencies $\omega_1 \pm \omega_2$ as well as ω_1 and ω_2.

1.3: THIRD-ORDER EFFECTS

The third-order nonlinear susceptibility, $\chi^{(3)}$, leads to effects such as third-harmonic generation, four-wave mixing, optical phase conjugation, the Kerr electro-optic effect, two-photon absorption, the Raman effect and the intensity-dependent refractive index change. This is also the term relevant to the ac Quantum Confined Stark Effect.

An expression for the intensity-dependent refractive index change may be easily obtained by considering a material whose second-order susceptibility is negligible. Its induced polarisation may be written as

$$P = \varepsilon_0 \chi^{(1)} E + \chi^{(3)} E^3 \tag{1.3}$$

Let E be of the form

$$E(t) = E_1 e^{j\omega t} + c.c. \tag{1.4}$$

The nonlinear intensity-dependent refractive index n_2 is defined by the equation

$$n = n_0 + n_2 I \tag{1.5}$$

where n_0 is the linear refractive index and I is the light intensity. By inserting Eqn. 1.4 into Eqn. 1.3 and relating P and E to the refractive index n, an expression can be found for n_2 *(Bhumbra 1990)* :

$$n_2 (S.I.) = \frac{\chi^{(3)}}{2c\, n_0^2 \varepsilon_0} \tag{1.6}$$

where c is the velocity of light and ε_0 is the permittivity of free space, both in S.I. units. So, if a material has a non-zero third-order susceptibility $\chi^{(3)}$, there will be a change in the refractive index under the application of intense light.

1.4: THE KRAMERS-KRÖNIG RELATIONS

The Kramers-Krönig relations state that the real and imaginary parts of a response function to a driving force are not independent of each other. They are based on the principle of causality, i.e. that the cause of an action precedes its effect, and are only applicable if the response is linear with the force. The susceptibility is the response function describing the response **P** to a driving force **E**, and so its real and imaginary parts are related to each other by the equations

$$\chi_1(\omega) = \frac{2}{\pi} \wp \int_0^\infty \frac{\Omega}{(\Omega^2 - \omega^2)} \chi_2(\Omega) d\Omega \quad \ast \tag{1.7}$$

$$\chi_2(\omega) = -\frac{2}{\pi} \wp \int_0^\infty \frac{\omega}{(\Omega^2 - \omega^2)} \chi_1(\Omega) d\Omega \tag{1.8}$$

where χ_1 is the real part of the susceptibility, and χ_2 is the imaginary part *(Abragam 1961)*. It is seen from these relations that if the real part of the susceptibility is known at all frequencies Ω, then the imaginary part at any individual frequency ω can be calculated, and vice versa.

The real part of the susceptibility is related to the refractive index, and the imaginary part to the absorption coefficient and so, by substituting the relations between them into the Kramers-Krönig relations, a new set of relations may be obtained. The change in the refractive index Δn at a particular frequency is related to the change in absorption coefficient $\Delta\alpha$ at all frequencies by

$$\Delta n(\omega) = \frac{c}{\pi} \wp \int_0^\infty \frac{\Delta\alpha(\Omega)}{\Omega^2 - \omega^2} d\Omega \tag{1.9}$$

This means that if there is a change in the absorption coefficient under the application of intense light, then there must also be a change in the material's refractive index, although not necessarily at the same wavelength. The analogous equation can be found for the relationship between the change in $\Delta\alpha$ at a particular frequency and the change in Δn at all frequencies.

The Kramers-Krönig relations are very useful in the field of nonlinear optics, but they are only approximate in this case, as one of the inherent assumptions in them is that the response is directly proportional to the driving force.

$\ast$ Here $\wp$ denotes the principal part of the integral. This means that the integral is evaluated over all values of Ω between 0 and ∞, except for at the singularity, i.e. when $\Omega=\omega$.

1.5: EXAMPLES OF DIFFERENT TYPES OF NONLINEAR OPTICAL DEVICES

Two devices which are vital building blocks for optical communications are modulators and switches, and the following sections will describe these in more detail.

1.5.1: MODULATORS

In order to convey information by means of light, it is necessary to impose a time-varying alteration of some measurable property of the light, e.g. its intensity, wavelength, polarisation or phase. This modulation may be "direct", analogous to flicking a light bulb switch on and off, or "indirect", analogous to putting the light bulb in a box, and opening and closing the box lid.

An example of direct modulation is seen when a semiconductor laser beam's intensity is altered by altering the excitation current passed through the semiconductor. This can be achieved for frequencies up to at least 30 GHz *(Lau et al. 1984)*, but there are several disadvantages to this type of modulation, namely that the choice of laser source is limited, it is difficult to obtain an analogue type of modulation, and it is unsuitable for use in a more complicated device, with more than one stage of modulation.

The modulation described in this thesis is of the indirect type. This occurs when the light causes a change in a physical property of the material through which it is travelling, and then this change in the material in turn causes a change in some measurable property of the light itself. For example, an all-optical amplitude modulator can be made if the electric field of an intense light beam alters the absorption coefficient of a material, and hence the intensity of light transmitted by the material is changed by means of a nonlinear optical effect. In a similar way, an all-optical phase modulator can be made if the electric field of an intense light beam alters the refractive index, and hence the optical length, of a material, by means of a nonlinear optical effect, so that the phase of the light transmitted by the material is altered.

1.5.2: SWITCHES

In opto-electronics, switching is said to occur when a change in a physical property of the material through which the light is travelling causes the position of the maximum of the light intensity to move in space. An example of a switch is the

directional coupler, which consists of two parallel waveguides positioned very close to each other. When a static electric field is applied, the refractive index of the material is altered locally by means of the electro-optic effect, and the strength of the electric field can determine out of which guide the light emerges.

In an all-optical directional coupler, the same result is obtained when the refractive index of the material is altered by a nonlinear optical effect due to the electric field of an intense optical beam. The directional coupler is designed so that light of low intensity is coupled between the guides and emerges from the opposite guide from the one into which it was launched. When the light is of high intensity, the refractive index is altered locally in the guide into which the beam was launched. This difference in refractive index between the two guides means that the coupling between them is broken, and so high-intensity light emerges from the guide into which it was launched. In this way, the intensity of the light determines from which of the guides the beam emerges *(Li Kam Wa et al. 1985, Jin et al. 1988, Jin et al. 1990, Finlayson et al. 1988).*

1.6: MEASURES OF MERIT FOR MODULATORS AND SWITCHES

Desirable properties for modulators are a broad bandwidth, large modulation depth, low insertion loss and low power requirement. The last two conditions apply equally to switches, and the equivalent to the first two are short switching times and a low degree of crosstalk *(Hammer 1979)*. These four requirements are traded against each other, depending on the specific systems requirement. An example of a figure of merit sometimes used is the specific energy, which is defined for an intensity modulator as the drive power required per unit bandwidth to obtain a modulation depth of 70%.

In order to fulfil these requirements, a good material for nonlinear optical modulators or switches must therefore have a fast response time, be resistant to optical damage at the intensities necessary for operation and be highly nonlinear at the desired wavelength, while still possessing a sufficiently small absorption coefficient that the device's insertion loss is not too great *(Smith 1984)*. In Section 1.8, various materials which have been used for nonlinear optical waveguide devices will be compared, with particular reference to these desirable characteristics.

1.7: NONLINEAR OPTICAL EFFECTS IN WAVEGUIDES

Optical waveguides confine light to the higher refractive index material of the guiding region. The small cross-sectional waveguide area leads to very high intensities of light for moderate power levels, so that nonlinear optical effects are enhanced in waveguide structures compared to bulk material. Their other major advantage over bulk samples is that the light is not diffracted, as it would be when travelling through free space or bulk material. This means that the light can propagate for comparatively long distances (of the order of centimetres) and this increase in interaction length results in even weak nonlinear effects adding up to useful levels *(Stegeman and Seaton 1985)*.

1.8: MATERIALS USED FOR NONLINEAR OPTICAL WAVEGUIDES

1.8.1: LITHIUM NIOBATE

Lithium Niobate has been used for many years as a nonlinear optical material. The higher refractive index for the guiding region is normally achieved either by high-temperature diffusion of titanium into a $LiNbO_3$ substrate or by proton exchange in benzoic acid *(Al-Shukri et al. 1985)*. Because it is a noncentrosymmetric material, it is used for second harmonic generation *(De Micheli and Papuchon 1985* and *Sohler 1990)*, as well as for TM-TE mode conversion *(Hinkov et al. 1988)* and for electro-optic and acousto-optic modulators *(Papuchon 1990)*. The first all-optical picosecond waveguide modulator was a Mach-Zehnder interferometer device fabricated in $LiNbO_3$, which theoretically acts as a XOR, AND or NOT gate (Fig. 1.3) *(Haus and Whitaker 1984)*. It was found to demonstrate some of these features but, because the peak power was not high enough, it did not operate as a XOR gate.

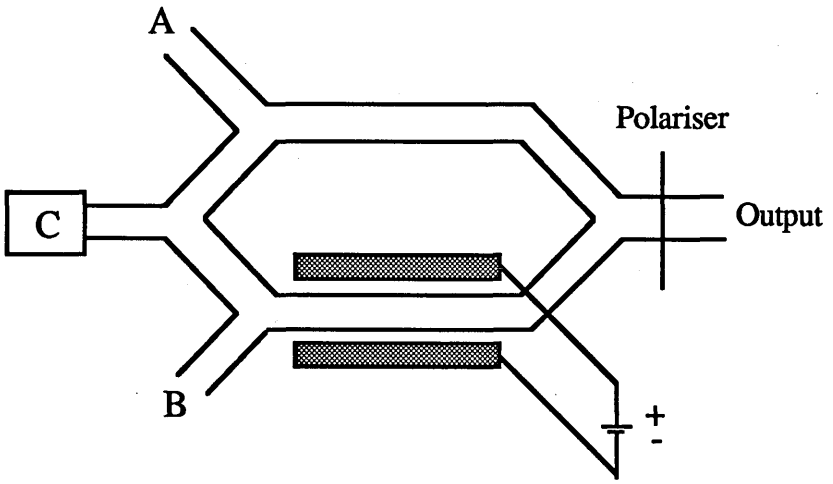

B \ A	0	1
0	0	1
1	1	0

Truth table

Fig. 1.3 Optically modulated Mach-Zehnder interferometer *(Haus and Whitaker 1984)*

1.8.2: ORGANIC MATERIALS

Organic materials have been observed to possess very large nonlinear optical susceptibilities. The electro-optic coefficient of MNA, a molecule based on a benzene ring structure, has been shown using second harmonic generation experiments to be about 67×10^{-12} mV^{-1}, about twice as high as that of Lithium Niobate *(Lipscomb et al. 1981)*. Particular polymers, known as polydiacetylenes, possess a very large third-order susceptibility with subpicosecond response times. Because the polymers are long chains of molecules, the π electrons are delocalised along the one-dimensional carbon backbone, and it has been estimated *(Carter et al. 1985)* that $\chi^{(3)}$ is proportional to L^6, so that if the wave function is changed from two atoms to just four atoms, $\chi^{(3)}$ is increased by a factor of almost 100. The intensity-dependent refractive index, n_2, has been measured in the polydiacetylenes to be about 10^{-16} m^2/W. Methods of processing polydiacetylenes into waveguides are still being developed, but both slab and channel waveguides have been fabricated by a variety of techniques *(Townsend et al. 1988)*, and all-optical phase modulation of electronic origin has been observed *(Thakur and Krol 1990)*.

Liquid crystals are generally centrosymmetric, and so do not exhibit second-order nonlinear optical processes, but several third-order effects have been observed in them. The electronic contribution to their nonlinearity is similar to that for ordinary organic liquids but, because there is a strong correlation between the molecules, molecular reorientation, caused by either a dc or optical electric field, leads to extremely high refractive index changes (as large as about 0.01-0.1 for a dc field of 100 V/cm or for an optical intensity of 100 W/cm^2) *(Khoo and Shen 1985)*. Their greatest disadvantage for use in practical devices is that their response times are very slow, of the order of microseconds.

1.8.3: GLASSES

Waveguides can be fabricated in glasses by several methods. In the process of ion exchange, the glass, containing both sodium and potassium ions, is placed in a bath of potassium nitrate, so that potassium ions replace some of the sodium ions in the glass, and so increase the refractive index. The method most widely used, however, is to pull the glass (usually silica) into a cylindrical fibre, whose refractive index in its core is increased by the addition of dopants, such as germania, over that of its cladding.

Most nonlinear optical processes in glasses are third-order, although very efficient second-harmonic generation has been observed in silica fibres: this is despite

silica being centrosymmetric and also a difficult material in which to achieve phase-matching *(Farries et al. 1987)*. The reason that second-harmonic generation takes place is that dopants, such as germania, can create a periodic distribution of colour centres, and hence a periodic change in the second-order nonlinear susceptibility, which leads to phase-matching being achieved. Third-order effects which have been observed in glass waveguides and fibres include the Raman and Brillouin effects, group velocity dispersion *(Marcuse and Lin 1981)*, self-phase modulation and the Kerr effect, that is the intensity-dependence of the refractive index *(Byron 1987 and White et al. 1988)*.

An all-fibre optical fibre 'AND' gate has been successfully demonstrated *(Kimura et al. 1986)*, as has a 1.97 GHz multi/demultiplexer *(Morioka et al. 1987)*, an ultrafast all-optical fibre modulator *(Halas et al. 1987)* and several fibre switches operating by means of the optical Kerr effect *(Friberg et al. 1987, Penty et al. 1988 and LaGasse et al. 1989)*. The intensity-dependent refractive index n_2 is about 10^{-20} m^2/W in silica fibres, which is several orders of magnitude smaller than most other materials discussed in this section. However, because of the extremely low absorption coefficient of about 10^{-5} cm^{-1}, it is possible to use very great lengths of fibre, and so, even despite such a low value for n_2, optical fibre has led to some of the most promising nonlinear optical devices yet demonstrated.

Another particularly promising material is semiconductor-doped glass, which is glass containing small (10-100 nm) crystallites of CdS_xSe_{1-x} *(Cullen et al. 1986)*. In this material, n_2 is about 10^{-14} m^2/W, and also has a response time of the order of a few picoseconds *(Banyai et al. 1989 and Ainslie et al. 1987)*, but this is at the expense of greatly increased absorption of about 8 cm^{-1}.

Although glasses, other than semiconductor-doped glass, are not suitable for compact devices, they are ideal for applications, such as telecommunications, where the length of nonlinear medium used is not important, as great lengths of fibre can then be used to enhance the nonlinear effects.

1.8.4: SEMICONDUCTORS

Most of the research into nonlinear optical guided wave devices has been carried out in semiconductors, because of the potential benefits of monolithic integration with semiconductor lasers. Semiconductor growth and processing are now well understood and reproducible, and the GaAs/$Al_xGa_{1-x}As$ material system in particular has the great advantage that the aluminium fraction x can be altered without affecting the lattice constant of the $Al_xGa_{1-x}As$ so much as to introduce significant strain at the GaAs

interface. Altering x changes both the band gap and refractive index of the $Al_xGa_{1-x}As$ layer. Waveguiding occurs in a layer of higher refractive index material (such as GaAs) when it is surrounded by a material of lower refractive index (such as $Al_xGa_{1-x}As$), and so x can be tailored to produce the ideal refractive index difference between the layers which will confine the light optimally.

Several nonlinear optical devices have been demonstrated in GaAs/AlGaAs bulk material, but recently most attention has been given to semiconductor Multiple Quantum Well (MQW) material. This consists of very thin layers (of the order of 100 Å) of a lower band gap material (e.g. GaAs) sandwiched between layers of about the same thickness of a higher band gap material (e.g. $Al_xGa_{1-x}As$). Because of the potential discontinuities at the boundaries between the layers, the electrons and holes are partially confined in the well material, and this quantum confinement leads to the existence of excitonic features in MQW material even at room temperature (see Chapter 2 for a more detailed account of the theory of MQW material).

This exciton persistence at room temperature leads to effects such as the dc Quantum Confined Stark Effect (dc QCSE), which occurs when a dc electric field is applied to a MQW structure, and which has been used for electro-optic modulators *(Wood 1990)*. In a similar way, the ac Quantum Confined Stark Effect (ac QCSE) occurs when an optical electric field is applied to a MQW structure, and has been shown to produce ultrafast all-optical modulation (< 500 fs recovery time) in a GaAs/AlGaAs directional coupler *(Jin et al. 1990)*. Optically bistable waveguide devices have been made which use the dc QCSE in conjunction with a negative resistance device, and produce an on/off ratio of 19:1 with a frequency of 100 GHz for an optical power of 1 mW and a bias voltage of -5 V *(Sakaki et al. 1988)*. All-optical waveguide switches have also been demonstrated for both horizontal *(Li Kam Wa et al. 1985)* and vertical couplers *(Berger et al. 1988)*. The intensity-dependent refractive index n_2 of GaAs/AlGaAs is highly wavelength-dependent. It has been measured in GaAs/AlGaAs MQW waveguides to be about -10^{-11} m^2/W at 850 nm, at which wavelength the absorption coefficient α was 20 cm^{-1} *(Li Kam Wa et al. 1985)*, and $-3x10^{-15}$ m^2/W and $-4x10^{-16}$ m^2/W for TM and TE polarisations respectively at 1.06 μm *(White et al. 1990)*.

The other main semiconductor system of major interest is InP/InGaAsP, mainly because its band gap can be tailored so as to lie at a minimum in both the loss and dispersion spectra of silica fibres. An optical AND gate has been reported at 1.3 μm using a bistable Fabry-Pérot InGaAsP/InP laser amplifier, and several material systems have been chosen for phase modulators based on the dc QCSE, including InGaAsP/InP *(Tsang and White 1990)* and InGaAs/InP *(Koren et al. 1987)*. The ac QCSE has also

been observed in InGaAs/InP MQW material *(Tai et al. 1987)*, a directional coupler has been demonstrated at 1.15 μm in a GaAs/InGaAs strained-layer superlattice *(Das et al. 1987)* and an InGaAs/ InP MQW absorption modulator using the dc QCSE has been shown to have a modulation depth of 19 dB *(Bryce et al. 1991)*.

1.9: SUMMARY OF CHAPTER ONE AND OBJECTIVES FOR THE WORK CONTAINED IN THIS THESIS

Nonlinear optical devices have been shown to have several advantages over electronic devices for signal processing. The basic formalism of nonlinear optics has been outlined, and some second-order and third-order nonlinear effects described. The Kramers-Kronig relations have been stated, together with the conditions for their use. Two nonlinear optical devices, modulators and switches, have been described and the requirements for them listed. Lastly, the materials used for nonlinear optical waveguide devices have been compared and discussed, with reference to successful devices in the literature.

The purpose of the experimental work described in this thesis was to investigate nonlinear absorption and phase modulation in GaAs/AlGaAs MQW waveguide structures at 1.06 μm. The reasons for choosing this material system were the strength of its nonlinear optical processes and its suitability for monolithic integration with semiconductor lasers and electronic systems. The particular operating wavelength was chosen because, although the nonlinearities of the material are much weaker at this wavelength than close to the bandedge, the material's absorption coefficient and response time are also much smaller.

CHAPTER TWO

THEORY OF LINEAR AND NONLINEAR ABSORPTION IN SEMICONDUCTORS

2.1 BULK SEMICONDUCTORS

2.1.1: LINEAR ABSORPTION IN BULK SEMICONDUCTORS

Absorption occurs when photons of energy $\hbar\omega$ are used to excite electrons or holes with energy E_i to a higher energy state E_f, so that

$$E_f = E_i + \hbar\omega \tag{2.1}$$

The absorption coefficient depends on the transition rate of electrons from one energy state to another due to photons of various energies, and this can be calculated using Fermi's Golden Rule *(Eisberg 1964)*. This rule is derived using perturbation theory, and states that the transition rate from an initial state i to a final state f due to a perturbation of the form $V\exp(-i\omega t)$, which could represent photons, phonons or another form of excitation, is given by *(Davies 1987)*

$$\text{Transition Rate} = \frac{2\pi}{\hbar}|V_{fi}|^2 n(E_f) \tag{2.2}$$

where $E_f = E_i + \hbar\omega$, $V_{fi} = \int \Psi_f^* V(t) \Psi_i$, and $n(E_f)$ is the density of states at energy E_f. V_{fi} is known as the matrix element or overlap integral between two energy states, and is extremely important in optical processes, as its magnitude determines the strength and selection rules of optical processes.

Figs. 2.1(a) and (b) show typical absorption spectra for a semiconductor over a very large range of photon energies. The most important part of the spectra for the study of semiconductors is the absorption edge at about 1 μm (i.e. about 1 eV), and this is the region in which the absorption of photons results in the transition of electrons from the top of the valence band to the bottom of the conduction band. For photon energies $h\nu$ just greater than the band gap E_g, the density of states (and so, by Fermi's Golden Rule, the absorption coefficient) is proportional to $(h\nu - E_g)^{1/2}$ *(Omar 1975)*.

Absorption of photons of higher energy, up to about 5 eV, results in electron transitions from deeper in the valence band or to higher energies in the conduction band.

Further into the ultra-violet spectrum, i.e. at higher energies, plasma effects are seen due to the valence band electrons behaving like a plasma of free particles, and photon energies greater than about 15 eV can cause the inner-shell electrons to be excited into the conduction band *(Hodgson 1970)*.

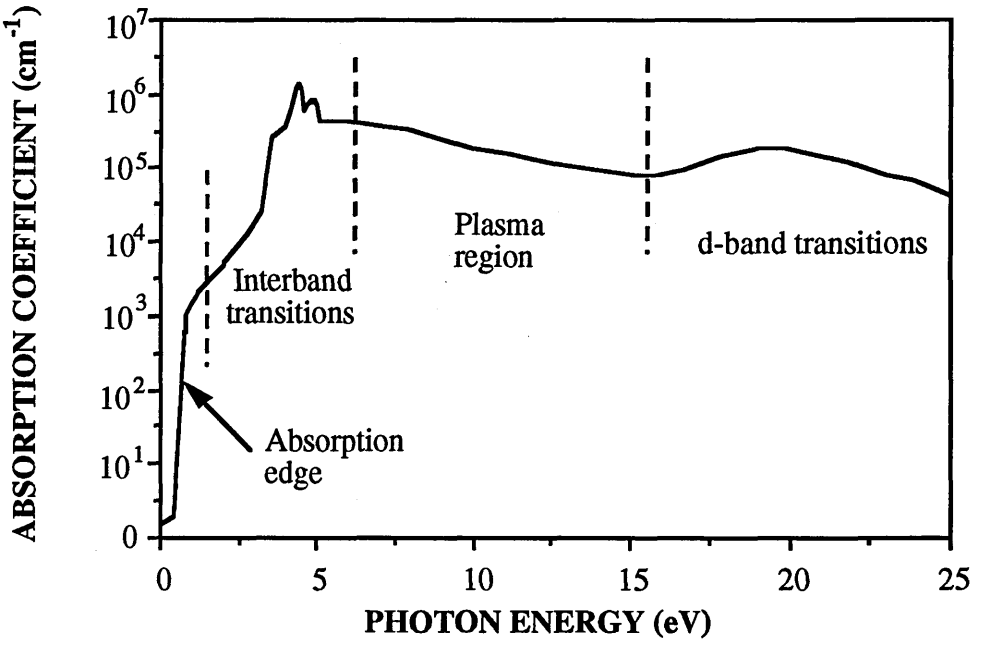

Fig. 2.1(a) Typical semiconductor ultraviolet absorption spectrum (after *Moss 1973*)

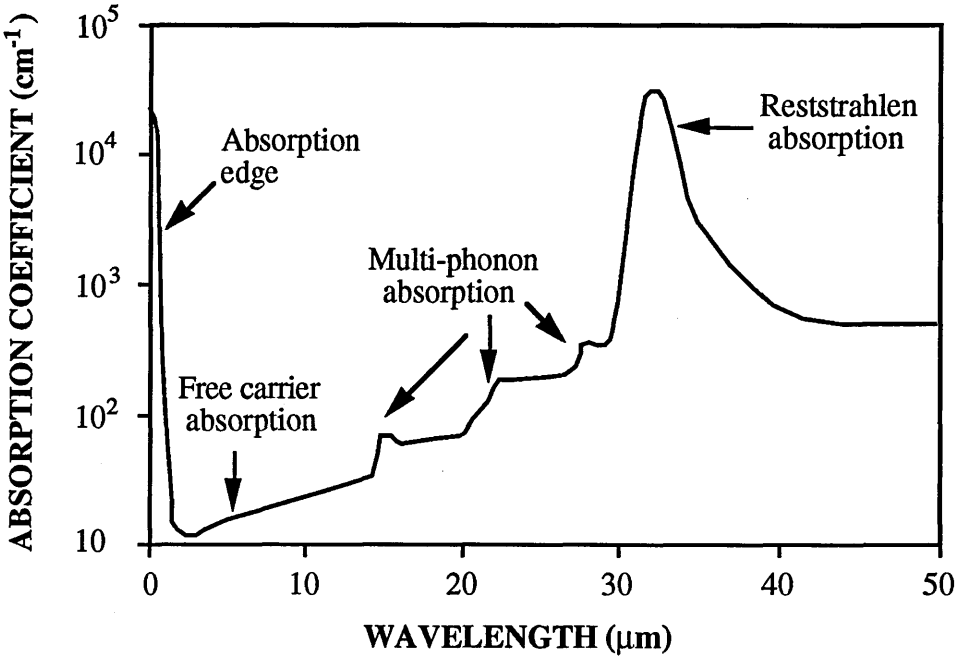

Fig. 2.1(b) Typical semiconductor infrared absorption spectrum (after *Moss 1973*)

In theory, the absorption edge would be infinitely steep, but in practice it falls off exponentially, as shown in Fig. 2.1(b). This additional absorption can occur for several reasons. The existence of shallow impurity bands in the forbidden gap can lead to a tail in the density of states which extends into the forbidden gap, as can internal electric fields or strain in the crystal. The final important cause of the absorption tail is inelastic phonon scattering, which is described by Urbach's Rule *(Urbach 1953)*:

$$\frac{d(\ln \alpha)}{dh\nu} = \frac{-1}{kT} \tag{2.3}$$

On the long-wavelength side of the absorption edge, an increase in absorption is seen due to free carrier absorption, that is transitions of free electrons within the conduction band, as in metals. At still longer wavelengths, there are features in the absorption spectrum due to lattice vibrations and phonons *(Omar 1975)*.

The region of the spectrum of interest for this thesis is at or just below the absorption edge. Providing that the incident photon energy is comparable to that of the energy gap, electrons can be excited from the valence to the conduction band. Both energy and momentum must be conserved in this process.

In direct semiconductors, such as GaAs, the bottom of the conduction band lies at the same k value as the top of the valence band. This means that the momentum of the electron in the initial energy state is equal to that in the final energy state, and so both energy and momentum are conserved when a photon excites an electron from the valence to the conduction band.

For indirect semiconductors the momentum of the electron in the initial energy state is not equal to that in the final energy state, and so a compensating momentum must be provided in order that momentum is conserved in the transition. This compensating momentum cannot be provided by photons, because the photon momentum is negligible at wavelengths around the absorption edge. It must therefore be provided by another source, for example phonons. Thus, in order for a transition to take place in an indirect semiconductor, a phonon must be either absorbed or emitted when the photon is absorbed. Absorption and emission of photons in indirect semiconductors is therefore a three-particle process, and so the probability of its occurrence is reduced.

2.1.2: EXCITONS IN BULK SEMICONDUCTORS

When photons are absorbed, the photogenerated electrons and holes do not behave as completely free particles. Because of their electrostatic interaction, they form bound states in a similar manner to the hydrogen atom, in which the two particles revolve about their centre of mass. These bound states are known as excitons and, as their formation energy is less than that to excite an electron into the conduction band, exciton states can be thought of as existing within the forbidden energy gap. In bulk material, the ground state excitonic binding energy, R_0, and Bohr radius a_0 are given in SI units by

$$R_0 = \frac{e^4 \mu}{2\varepsilon_0^2 \hbar^2} \tag{2.4}$$

$$a_0 = \frac{\varepsilon_0 \hbar^2}{\mu e^2} \tag{2.5}$$

Here μ is the reduced electron-hole mass, defined as

$$\mu^{-1} = m_e^{-1} + m_h^{-1} \tag{2.6}$$

where m_e and m_h are the electron and hole masses, respectively. There is an infinite series of energy levels for the exciton, just as for the hydrogen atom, and the energy of the n^{th} level is given by

$$E_n^{3D} = E_g - \frac{R_o}{n^2} \tag{2.7}$$

Excitons are seen as a narrow line in the absorption spectrum of a semiconductor, giving an enhancement in the continuous absorption, and situated just below the absorption edge (Fig. 2.2). The increased absorption occurs because of the attraction between the electron and hole, which increases the overlap integral V_{fi} between them. Because the excitonic binding energy, R_0, in Gallium Arsenide is only about 4 meV, its exciton resonances are thermally broadened due to exciton ionisation by LO phonons, and are not seen at room temperature. Excitons also tend to disappear in the presence of a high concentration of free electrons and holes, which screen the excitons. This will occur when the screening length is comparable to the Bohr radius a_0 of the exciton (about 140 Å for Gallium Arsenide at room temperature).

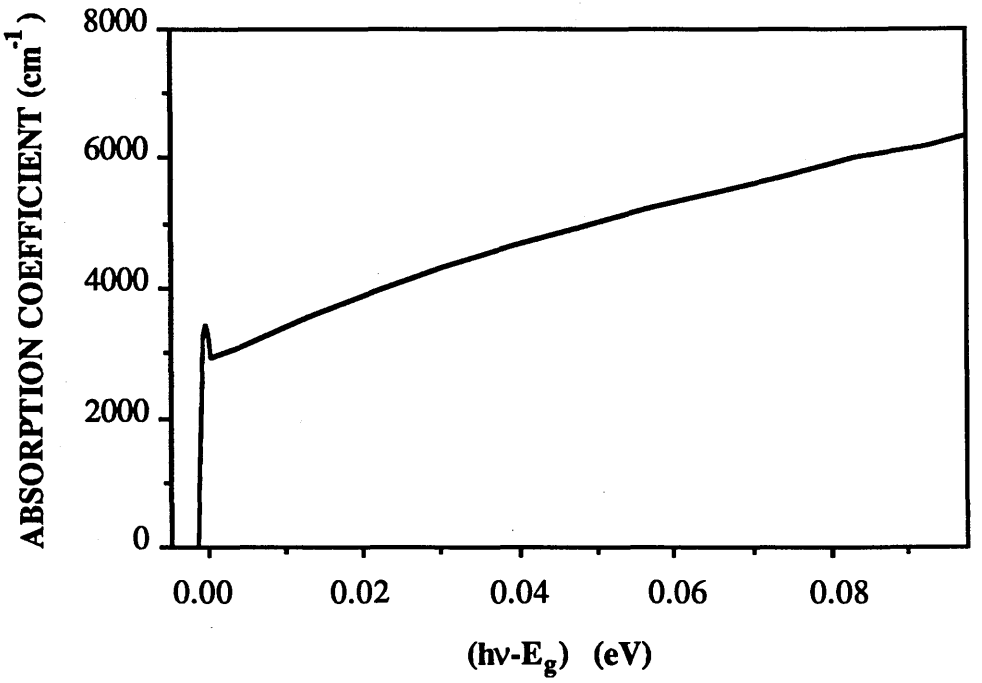

Fig. 2.2 Typical semiconductor absorption spectrum showing the exciton resonance near the absorption edge.

2.2 SEMICONDUCTOR QUANTUM WELLS

2.2.1: LINEAR ABSORPTION IN QUANTUM WELLS

A quantum well (QW) is formed when a thin layer (of the order of 100 Å) of a semiconductor is sandwiched between two thick layers of another semiconductor of larger energy gap, so that there is a step-like discontinuity in the energy bands. If these two intrinsic semiconductors have very similar lattice structures and constants, then the interfaces between them can be considered abrupt enough that the system can be modelled as a square well. The electrons and holes are confined to the well region by the potential barriers at the heterojunctions. Their energy levels in the well are now quantised, and can be calculated by solving Schrödinger's equation subject to the particular boundary conditions.

As the QW structure is the same as that of the classic quantum mechanical text-book problem of a one-dimensional "particle in a box", the effect of the confining potential barriers on the electron energy can be easily found. The eigenvalues of the

energy levels for an infinitely high potential well of width a in the direction perpendicular to the plane of the layers are given by *(Eisberg 1964)*

$$E_n = \frac{\hbar^2 \pi^2 n^2}{2 m a^2} \qquad (n = 1, 2, 3, 4....) \tag{2.8}$$

where m is the effective mass. For a finite well, the situation is more complicated, and can only be solved numerically or graphically. The boundary conditions are no longer that the wave function decays to zero at the barriers, as for an infinite well, since a portion of the wave function now exists in the barrier material, its amplitude falling exponentially away from the junction. There are a finite number of bound states with sinusoidal wave functions in the well, so that any higher energy states are unbound. The condition for the existence of N bound states in a potential well of height V and width a is given by *(Davies 1987)*

$$(N-1)\frac{\pi}{2} < \sqrt{\frac{mVa^2}{2\hbar^2}} < N\frac{\pi}{2} \tag{2.9}$$

and the energy eigenvalues E_n in the direction perpendicular to the plane of the layers are found from the two equations below *(Schiff 1968)*

$$k_1 \tan\left(\frac{k_1 a}{2}\right) = k_2 \tag{2.10}$$

$$k_1 \cot\left(\frac{k_1 a}{2}\right) = -k_2 \tag{2.11}$$

where $k_1 = \frac{\sqrt{2mE_n}}{\hbar}$ and $k_2 = \frac{\sqrt{2m(V - E_n)}}{\hbar}$.

It should be noted that two assumptions inherent in these equations are that the energy bands are parabolic, and that the electron and hole effective masses in the well material are equal to those in the barriers. In reality, the effective masses in the two semiconductor materials used for the well and barrier sections will differ by a small percentage, and the equations can be altered slightly to take this difference into account.

Fig. 2.3 shows a band diagram for a QW of finite depth. The dependence of E_n on the mass of the particles means that the heavy and light hole bands are no longer degenerate, as they were in bulk material. The carriers are unaffected by the presence of the barriers in the direction parallel to the plane of the layers, and are free to move as in bulk material.

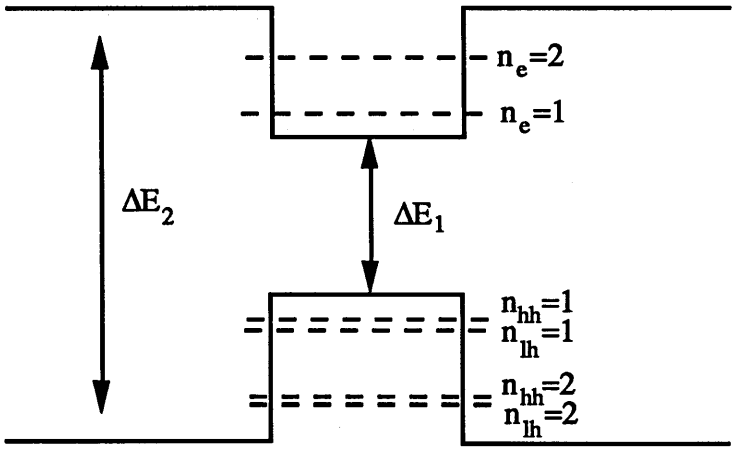

Fig. 2.3 QW structure with two confined states in the valence and conduction bands. ΔE_1 is the well (e.g. GaAs) band gap, and ΔE_2 is for the barrier (e.g. AlGaAs) band gap. The heavy hole energy eigenvalue is denoted by hh, and the light hole by lh.

The most commonly used semiconductor QW system, and that used entirely in this thesis, is GaAs for the well and $Al_xGa_{1-x}As$ for the barrier material. A high value for x results in increased carrier confinement, as the potential barrier is higher and there is less tunnelling of carriers into the barrier material but, in general, x will not be much greater than about 0.3, so that the difference in lattice constants does not lead to strain at the heterojunctions, and also so that the barriers remain a direct-gap material.

The width of the well region is also critical for good confinement. It should be narrower than the electronic mean free path of about 400 Å, so that the electrons can 'see' the confining barriers, but it should be thicker than about 20 Å, so that the material may be considered to have the same properties as macroscopic GaAs *(Jaros 1989)*.

Photons can be absorbed by GaAs QWs, and electrons are excited from the valence to the conduction band, just as for bulk material, except for the condition that transitions can only take place between discrete energy levels with equal quantum numbers n. Because the lowest conduction level E_{e1} lies above the level of the bottom of the bulk GaAs conduction band and the highest valence level E_{hh1} lies below the level of the top of the bulk GaAs valence band, the effective band gap of the QW structure is greater than that of bulk GaAs. The effective band gap can be altered by changing either the aluminium fraction in the barriers or the well width.

Fig. 2.4 shows the density of states spectra for bulk and QW material. As mentioned in Section 2.1, the bulk density of states varies as $\sqrt{E-E_g}$. The QW

density of states in the direction perpendicular to the plane of the wells is a staircase shape, due to the quantisation of the energy levels. It can be seen that as the well width increases, the QW energy levels become closer together, so that the density of states spectrum approaches that of the 3D case. Similarly, as the well width becomes smaller, the QW energy levels become further apart, so that the density of states spectrum approaches that of the 2D case, which is a step-function $n_{2D}(E) = (m / \pi\hbar^2)$ *(Davies 1987)*.

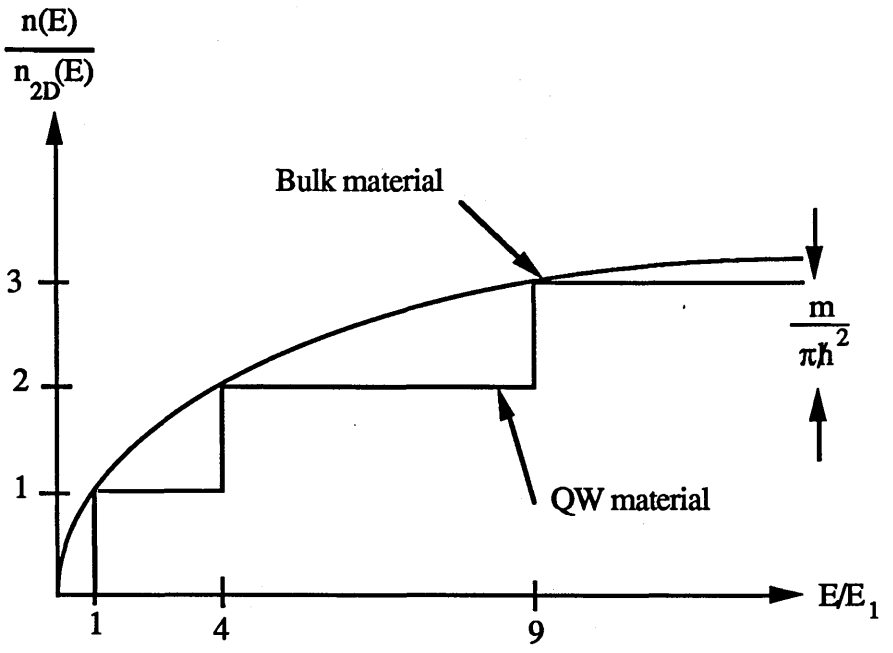

Fig. 2.4 Density of states spectra for bulk and QW material

Periodic structures of a large number of alternating layers of well and barrier material can now be grown. If the barriers are sufficiently narrow that the wavefunctions in adjacent wells overlap, then tunnelling takes place. The carriers are no longer strongly confined, nor are the energy levels discrete, as for a single QW, but broadened into a series of minibands. This type of structure is known as a superlattice. If the barriers are wider, then there is no significant overlap of wavefunctions, and the carriers remain localised in the wells. Each well section may be considered in isolation to have the same properties as the single QW already discussed, and the entire structure can be considered to be a superposition of a large number of single QWs, with energy eigenvalues given by Eqns. 2.6 or 2.7. This type of structure is known as a Multiple Quantum Well (MQW) structure.

2.2.2: EXCITONS IN SEMICONDUCTOR QUANTUM WELLS

In Section 2.1.2, we considered excitons in three-dimensional (3D) bulk semiconductor systems. QWs have properties intermediate between those of 3D and 2D systems, and the properties of excitons in them are very different to those in bulk material.

In pure 2D material, the exciton binding energy is $4R_0$, and the Bohr radius is $a_0/2$. Semiconductor QWs have a finite thickness, however, and so the binding energy is always less than $4R_0$. As the well thickness is made smaller, the exciton binding energy increases at first, but the wells can become so narrow that the wave function penetrates substantially into the barrier material. Hence, beyond a certain limit the exciton radius increases and the binding energy become smaller *(Bastard 1982 and Greene 1983)*. For GaAs/AlGaAs MQW structures, the maximum binding energy lies between $2R_0$ and $3R_0$ *(Chemla 1984)* and, for example, in 100 Å $GaAs/Al_{0.3}Ga_{0.7}As$ QWs at room temperature the binding energy and Bohr radius are 9 meV and 65 Å respectively. Because of the increase in binding energy, the exciton resonances are further away in energy from the continuum. The contrast between the exciton resonances and the continuum is also greater, while the interaction between excitons and phonons remains about the same as in bulk material. These three factors mean that excitonic features are well resolved in MQW structures even at room temperature. (However, because the LO phonon energy of 36 meV is so much greater than the excitonic binding energy of about 10 meV, excitons are still very easily ionised, so that their lifetime at room temperature in GaAs/AlGaAs QWs is about 400 fs).

The other major difference between excitons in bulk and MQW material is that the heavy and light hole excitons can be resolved due to the lifting of the valence band degeneracy at k=0 by the quantum confinement. This effect is visible in absorption spectra using TE polarised light, and can be seen in the transmission spectra taken in the material used for the experiments of this thesis and shown in Fig. 4.7. (For TE polarised light, the optical transition matrix elements from the heavy and light hole bands to the conduction band are in the ratio 3:1 respectively). With TM polarised light, the matrix element from the heavy hole band to the conduction band is zero, so that only the light hole exciton resonance can be seen in the transmission spectrum (see Fig. 4.8).

The exciton resonance in QWs has a typical FWHM of about 2 meV, mainly due to fluctuations in the well width, and roughness at the well/barrier interface *(Weisbuch 1981)*. This inhomogeneous broadening means that the exciton resonance can be accurately modelled by a Gaussian lineshape.

2.3 TWO-LEVEL ATOMIC MODEL

The model of a two-level atom has been extensively used in the theoretical treatment of the interaction of light with matter, and the valence and conduction bands of a semiconductor can be approximated to an example of a two-level system. More accurately, a semiconductor can be considered an inhomogeneously broadened set of two-level atoms, each with a different energy difference between the levels. This is because transitions can take place not only between the states at the top of the valence band and the bottom of the conduction band, but also between any states for which there is no difference in momentum. One of the main assumptions of the model is that there is no energy transference between atoms, and this is generally not the case for semiconductors, which are crystalline solids with various interactions between energy states. A rigourous theory of the nonlinear optical properties of semiconductors must therefore involve many-body theory in order to take account of processes such as scattering and Coulomb interactions, but the two-level atomic model is still extremely useful as an initial basis for understanding *(Miller 1981)*.

2.3.1 INTERACTION BETWEEN A TWO-LEVEL ATOM AND AN OPTICAL FIELD

Let the wave functions of the two atomic eigenstates be the eigenfunctions $\psi_1(\mathbf{r},t)$ and $\psi_2(\mathbf{r},t)$. In the absence of light, the Hamiltonian of the atom is H_0 and the Schrödinger Equation is written as

$$i\hbar \frac{d\Psi_n(r,t)}{dt} = H_0 \Psi_n(r,t) \tag{2.12}$$

If the eigenfunctions are written as

$$\Psi_n(r,t) = \Phi_n(r) \exp(-i\omega_n t) \tag{2.13}$$

then the solution to the unperturbed Schrödinger's Equation is

$$H_0 \Psi_n(r,t) = \hbar\omega_n \Psi_n(r,t) \tag{2.14}$$

and the frequency difference between the two levels is given by $\omega = \omega_1 - \omega_2$. We now introduce the laser field to the two-level system as a perturbation $H'(t)$, so that the Hamiltonian of the perturbed system is given by

$$H = H_0 + H'(t) \tag{2.15}$$

where

$$H'(t) = -\tfrac{1}{2} er\,(Ee^{-ivt} + c.c) \tag{2.16}$$

where c.c. denotes the complex conjugate of the optical electric field. Here, -er is the electric dipole moment operator of the atom, and E(t) is the laser electric field of angular frequency ν. When the laser perturbation is present, the resulting wave function can be written as a linear superposition of the two eigenstates:

$$\Psi(r,t) = a_1(t)\Phi_1(r)\exp(-i\omega_1 t) + a_2(t)\Phi_2(r)\exp(-i\omega_2 t) \tag{2.17}$$

The probability amplitudes of the two states can be found by following the working described in *Boyd 1988* or *Shimoda 1986*. If the atom is assumed to be initially in the upper state, then at time t the probability amplitudes for the states are given by

$$a_1(t) = \frac{ix}{\Omega}\exp[-i(\omega-\nu)t/2]\sin\left(\frac{\Omega t}{2}\right) \tag{2.18}$$

$$a_2(t) = \exp[i(\omega-\nu)t/2]\left[\cos\left(\frac{\Omega t}{2}\right) - \frac{i(\omega-\nu)}{\Omega}\sin\left(\frac{\Omega t}{2}\right)\right] \tag{2.19}$$

where Ω is the Rabi frequency defined as

$$\Omega = \sqrt{(\omega-\nu)^2 + x^2} = \sqrt{(\omega-\nu)^2 + \left(\frac{E\int\Phi_1^*(-er)\Phi_2 dr}{\hbar}\right)^2} \tag{2.20}$$

Eqn. 2.14 shows that the probability of occupation of the lower level varies sinusoidally with time. There is alternating absorption and emission between the two states, with a periodic frequency Ω.

2.3.2 LONGITUDINAL AND TRANSVERSE RELAXATION TIMES

The periodic absorption and emission of photons described in Section 2.3.1 can only last for as long as the coherence lasts between the exciting radiation and the wavefunctions of the two states. In a semiconductor, many processes can destroy this coherence, such as scattering by other carriers or phonons. There are two relaxation times associated with the loss of coherence. The longitudinal relaxation time is the time constant associated with the perturbed system returning to its unperturbed population difference, and the transverse relaxation time is the time constant for the system's atomic dipole moment, i.e. its polarisation, to decay when the field is turned off *(Miller 1981)*.

2.3.3 REAL AND VIRTUAL TRANSITIONS

When an electron is excited from the valence to the conduction band, its quantum mechanical phase is initially highly correlated with that of the optical electric field, as described in Section 2.3.1.

If the photon energy is less than the band gap, then by the Uncertainty Principle, the maximum time that this excited state can exist is about $\hbar / \Delta E$ *(Miller 1981)*. If this time is longer than the times associated with scattering processes (see Section 2.3.2), then absorption takes place, and a real excited state population will be created which will not be coherent with the optical field. This is called a real transition, and its probability is highest when ΔE is minimum, that is when the photon energy is very close to that of the band gap.

As ΔE becomes greater, that is when the photon energy is nonresonant with the band gap, the lifetime of the coherent excited state becomes shorter and, if no scattering event occurs within this lifetime, then the transition is known as virtual. Because there is no scattering, there is no real absorption of energy in the material, and so there is no loss of coherence *(Schmitt-Rink 1989)*.

Optical nonlinearities involving real transitions are usually greater in magnitude, but slower, because of the real carrier populations involved, which have comparatively long lifetimes. Virtual optical nonlinearities are much smaller, but also much faster, as the excited states only exist for a time of about $\hbar / \Delta E$ (about 2 fs for 1.06 μm light and a GaAs/AlGaAs QW structure).

2.4 ALL-OPTICAL NONLINEARITIES INVOLVING REAL TRANSITIONS

Real transitions occur when the photon energy is close to the energy gap. When photons of energy greater than the band gap are absorbed, an electron-hole plasma is created and, when the photon energy is very close to that of the exciton resonance, excitons are created. In this latter case, the excitons will be thermally ionised into an free electron-hole plasma in about 400 fs (for GaAs/AlGaAs QWs at room temperature) *(Chemla and Miller 1984)*. This means that when continuous or picosecond optical excitation is absorbed at the exciton resonance, the changes in the absorption spectrum appear to be the same as for long excitations above the resonance. However, when femtosecond pulses are used, it can be seen that this is not the case. The major all-optical nonlinearities seen when the photon energy is either at or above the exciton resonance are described in more detail below.

2.4.1 PHASE-SPACE FILLING

When photons of energy greater than that of the exciton resonance are absorbed, large carrier densities can be created, and one of the mechanisms whereby these electron-hole pairs (bound or unbound) affect the exciton resonances is known as phase-space filling. This comes about because the Pauli exclusion principle states that transitions to occupied quantum states are forbidden for fermions. This is well known for free electrons and holes, and results in an effective increase in the band gap, known as the Burstein-Moss shift, but less well known for excitons. At low densities, excitons are thought of as bosons *(Madelung 1981)*, but as their concentration increases, the single-particle components of each exciton interact more strongly with those of the neighbouring excitons, so that they behave more as fermions, and are affected by the exclusion principle *(Chemla and Miller 1986)*. The valence and conduction band states near the band edge become filled by photoexcited carriers and by excitons, and this leads to a loss of states available for further exciton formation, and hence to a loss in exciton oscillator strength. (Because the lifetime of excitons at room temperature in QW structures is only about 400 fs, this loss of oscillator strength corresponds to an ultrafast saturable absorption at the exciton resonance, and this is one of the mechanisms employed in the saturable absorber method of modelocking semiconductor lasers *(Silberberg 1984* and *Haus 1985)*).

2.4.2 COULOMB SCREENING

Long-range Coulomb screening comes about when the charged particles in a semiconductor act so as to reduce the extra electric field introduced by the photoexcited electron-hole plasma *(Harrison 1979)*. They do this by moving both spatially and in momentum space by intraband scattering *(Haug 1985)*.

Screening affects the single-particle states of the system much more strongly than the neutral excitonic states, and is seen as a renormalisation of the free electron-hole pairs' energy, i.e. the band gap. This red shift in the band gap leads to a reduction in the exciton binding energy and an increase in the exciton radius, and this change in binding energy affects in turn the strength of the screening, so that the effects of screening and binding must be treated self-consistently *(Haug and Schmitt-Rink 1985)*.

The Debye screening parameter is a measure of the strength of Coulomb screening, and it is proportional to the derivative of the electron density N with respect to the chemical potential of the semiconductor μ. This derivative is given by *(Davies 1987)*

$$\frac{dN}{d\mu} = \frac{1}{k_B T} \exp\left(\frac{\mu}{k_B T}\right) \int_{-\infty}^{\infty} n(E) \exp\left(\frac{-E}{k_B T}\right) dE \qquad (2.21)$$

where k_B is the Boltzmann constant, T is the temperature and n(E) is the density of states at energy E. This equation shows that screening is more efficient at low temperatures than at high, and much stronger in 3D structures than in 2D, as the density of states is higher in 3D.

2.4.3 EXCHANGE INTERACTION

This is a purely quantum-mechanical effect, with no classical analogy, arising from the consequences of electrons being identical, i.e. indistinguishable from one another, and from the symmetry properties of electron wave functions when they overlap with one another *(French and Taylor 1979)*. Exchange effects can be thought of as short-range screening, and so they only become important for dense plasmas. They are particularly important in 2D structures, as carrier confinement leads to the particles seeing more of their near neighbours than in 3D *(Chemla and Miller 1986)*.

Exchange interactions lead to effects such as a blue shift in the exciton resonance due to exciton-exciton interactions leading to a renormalisation of the exciton self-energy. The electron and hole exchange self-energies are changed in the presence of the

photoexcited excitons, due to a gain in energy from fermions of the same spin avoiding each other (another manifestation of the Pauli exclusion principle), and repulsive interactions between excitons.

The bleaching of exciton resonances by phase-space filling and exchange is more efficient at low temperatures. When excitons are created by direct optical excitation, they have no excess energy, and so their effect on exciton bleaching is about twice as strong as that due to the "hot" electron-hole plasma created when the excitons are ionised by LO phonons (each electron-hole pair receives about 25 meV excess energy through ionisation).

2.4.4 FREE CARRIER ABSORPTION

Electrons in the conduction band or holes in the valence band can absorb photons of energy less than the exciton resonance, and make transitions higher into their bands. These transitions must be indirect, because of the change in momentum involved, and interactions with phonons or defects such as impurities are necessary. The free carrier absorption in a semiconductor is a function of the photon energy, the concentration of free carriers and the temperature *(Hodgson 1970)*.

2.4.5 EXPERIMENTAL OBSERVATIONS OF THESE EFFECTS

Complete bleaching of the exciton resonance due to band gap renormalisation has been demonstrated, leaving only a 2D continuum *(Chemla 1988)*. The QW width was 96 Å and the pump photon energy was 60 meV above the n=1 heavy hole exciton resonance. A free carrier density of about 2×10^{12} cm^{-2} was found to result in a red shift of the absorption edge of about 17 meV. It was also demonstrated that the change in the absorption spectrum does not depend on the pump photon energy, but just on the carrier density created. This was done by selectively generating excitons, and then probing the absorption spectrum 2 ps later, by which time the excitons had ionised to free electron-hole pairs. It was found that the changes in absorption were identical for the two cases.

Experiments have been carried out using ultrashort optical pulses to generate excitons directly by resonant excitation. It is seen that there is an initial very strong bleaching caused by the "cold" excitons, which have not yet interacted with the thermal reservoir of the lattice. After the exciton ionisation time of about 400 fs, the exciton

resonance bleaching is reduced, so that it is about 2.5 times smaller than its initial value after about 800 fs, and then remains constant for tens of picoseconds.

Pump-probe spectroscopy using pulses of 120 fs FWHM has been performed on a sample of 300 periods of 53 Å GaAs wells and 56 Å $Al_{0.3}Ga_{0.7}As$ barriers *(Peyghambarian 1984)*. At 15 K, and with the pump photon energy greater than the band gap, exciton bleaching was observed due to Coulomb screening in less than 150 fs. The exciton oscillator strength recovered in about 100 ps, the lifetime of the free carriers, but it was then seen that there was a blue shift in the exciton resonance. This shift has been interpreted as being due to Coulomb screening being so much weakened in the narrow wells that it can no longer compensate for the blue shift expected from exchange effects due to exciton-exciton interactions *(Chemla 1986)*. This interpretation was supported by changing the pump photon energy, so that excitons were generated directly. In this case, the blue shift was observed, as before, but without an accompanying bleaching. These experiments and their interpretations were further corroborated by repeating them at 224 K. In this case, with band-to-band excitation there was exciton bleaching without any energy shift, because the reduced exciton lifetime at higher temperatures means that most of the photogenerated electron-hole pairs remain as free carriers. With resonant excitation of excitons, it was found that there was a blue shift and bleaching during the exciton lifetime, followed by bleaching alone due to free carriers.

2.5 ALL-OPTICAL NONLINEARITIES INVOLVING VIRTUAL TRANSITIONS

Virtual transitions occur when the photon energy is less than that of the exciton resonance. In this case, very few real excitons or carriers can be created by the photons. Because very little real absorption of photons takes place, all-optical nonlinearities involving virtual transitions are faster than those for real transitions.

2.5.1 TWO-PHOTON ABSORPTION

Two-photon absorption (TPA) is a process by which a real carrier population can be created by a method involving virtual transitions. It is used not only as a means of absorption modulation in semiconductors, but also as a spectroscopic tool to investigate the electronic states of a solid, as the selection rules for two-photon absorption are different to those for one photon. Because the TPA coefficient is proportional to the intensity, it was not observed until the invention of the laser *(Kaiser 1961)*, despite having been first predicted thirty years earlier *(Goppert-Mayer 1931)*.

TPA occurs when an electron is excited from the valence to the conduction band via an intermediate state, and is allowed only if twice the photon energy is greater than the semiconductor energy gap. This intermediate state can be any state in the valence band, the conduction band, or some other band, provided that momentum is conserved in the transition. When TPA is analysed using second-order perturbation theory, it is found that the transition probability is highest when the energy difference between the states is smallest, that is when the intermediate state lies closest to the upper valence band or lowest conduction band *(Spector 1987)*. An electron can only remain in the intermediate state for a time governed by the Uncertainty Principle, as energy has not been conserved *(Miller 1981)*. When the second photon is absorbed, the electron reaches the final energy state such that $E_f - E_i = 2h\nu$.

The two photons involved in the absorption process can have different frequencies or polarisations, and it can be found theoretically that some two-photon transitions are forbidden for photons of the same polarisation, and some for photons of opposite polarisations *(Madelung 1981)*. There is also a polarisation dependence of the two-photon absorption spectra in GaAs/AlGaAs QW structures which has been demonstrated experimentally *(Catalano et al. 1989)*. Examples of quantities which can be measured using TPA spectroscopy are the conduction and valence band offsets in a

QW. In order to determine these, the energy difference between successive quantised conduction and valence band energy levels must be known. This is very difficult using one-photon spectroscopy, as transitions are only allowed between conduction and valence band levels with the same quantum number. However, the selection rules for two-photon transitions for light polarised parallel to the confinement direction of the QWs are such that transitions are allowed between conduction and valence subbands whose quantum numbers differ by ±1,±3,etc. *(Tai et al. 1989)*, and so the conduction and valence band offsets can be determined.

The TPA coefficient, β, can be defined by the equation for the rate of change of intensity I with distance z in a material with linear absorption coefficient α:

$$\frac{dI}{dz} = -\alpha I - \beta I^2 \tag{2.22}$$

from which it is found that the intensity at distance z is given by

$$I(z) = \frac{I(0)\ \alpha\ e^{-\alpha z}}{\alpha + \beta I(0)\ (1 - e^{-\alpha z})} \tag{2.23}$$

One of the main ways of measuring β is therefore by measuring the transmission of a sample for a beam of varying input intensity whose photon energy is less than the band gap E_g but greater than $E_g/2$. When β was measured for a wide variety of semiconductors, it was found to be given by *(Van Stryland 1985)*

$$\beta = \frac{K\sqrt{E_p}\ f\left(\frac{2h\nu}{E_g}\right)}{n^2 E_g^3} \tag{2.24}$$

where K is a material-independent constant, n is the linear refractive index, E_p is nearly material-independent and the function f depends on the assumed band structure. To a good approximation, β can be said to be proportional to E_g^{-3}.

2.5.2 AC QUANTUM CONFINED STARK EFFECT

When the excitation is in the transparency region of the semiconductor, there is little or no generation of real carriers or excitons, and so its effect is very different to that of excitation at or above the exciton resonance. In this case, only virtual excitons are created, which interact in exactly the same way as real ones, but do not participate in relaxation processes. The excitation induces a coherent polarisation in the semiconductor, which can be probed with a low intensity test beam, and it is found that there is a blue shift in the exciton resonance which persists only for the duration of the excitation, because no real excited state population is generated. This energy shift is known as the ac Quantum Confined Stark Effect (ac QCSE).

When the effect of Coulomb interactions is neglected, we can find an approximation for the change in interband transition energy by considering ac Stark shifts which have been calculated for a two-level atomic system in an alternating electric field *(Bonch-Bruevich 1968)*. From second order perturbation theory, an expression may be obtained for the change in band gap

$$\partial E_g = \frac{2|er_{cv} E_p|^2}{E_g - h\nu_p} \tag{2.25}$$

where E_g is the band gap, er_{cv} is the atomic dipole matrix element, E_p is the pump field and ν_p is the pump frequency.

This expression must be modified to include the Coulomb interaction. The atomic shift must be renormalised due to excitonic effects, because the electron-hole pair states inside an exciton experience not only the external electric field, but also a "molecular field" *(Schmitt-Rink 1986)* due to other virtual excitons. When the virtual 1s exciton state contribution is taken into account, an expression is found for the shift in the exciton energy due to the ac QCSE:

$$\partial E_g = \frac{2|er_{cv} E_p|^2}{E_{1s} - h\nu_p} \frac{|U_{1s}(r=0)|^2}{N_{PSF}} \tag{2.26}$$

where E_{1s} is the 1s exciton energy and N_{PSF} is the saturation density due to excitonic phase space filling.

2.6 SUMMARY OF CHAPTER TWO

This chapter began by discussing linear absorption, firstly in bulk semiconductors. Bulk semiconductor absorption spectra over a very large range of photon energies were discussed and the causes of their salient features identified. The concept of excitons was explained with reference to bulk material, and formulae quoted for the excitonic binding energy and Bohr radius.

Semiconductor QW material was then introduced, the quantisation of the energy levels was discussed and expressions were given for the eigenvalues of the energy levels for both an infinite and a finite QW. Linear absorption in semiconductor QW material was discussed and the differences between the density of states spectra for bulk and QW material noted. In bulk material, it had been stated that the density of states for photon energies just greater than the band gap varies as $\sqrt{E-E_g}$, whereas for QW material the density of states is a staircase shape. The selection rules for QW material are that transitions can only take place between valence and conduction band energy levels of equal quantum number.

Excitons in QW material were discussed, and the dependence of their Bohr radius and binding energy on well width described. The persistence of excitonic features at room temperature was explained, and the selection rules stated for transitions from the light and heavy hole bands to the conduction band for both TE and TM polarised light.

The model of a two-level atom was then used in order to introduce the theory of nonlinear optical effects in semiconductors. Equations were derived for the probability of occupancy of the two levels when an optical field was applied, and the longitudinal and transverse relaxation times associated with the loss of coherence between the two-level atom and the optical field were defined. Real transitions were defined as transitions for which the lifetime of the coherent excited state ($\hbar / \Delta E$) is longer than the relaxation times associated with scattering processes, and vice versa for virtual transitions. Hence, it was seen that real transitions occur when the photon energy is close to that of the band gap, and virtual transitions occur when it is much smaller than the band gap.

Various examples were then given of all-optical nonlinear processes involving both real and virtual transitions. Those involving real transitions were phase-space filling, Coulomb screening, exchange effects and free carrier absorption, and the theory for each of these was described separately. Experimental observations of these effects were then discussed, with reference to theory. Lastly, both the theory and experimental observations of two-photon absorption and the ac Quantum Confined Stark Effect were discussed as examples of all-optical nonlinear processes involving virtual transitions.

CHAPTER THREE
WAVEGUIDE DESIGN AND FABRICATION

This chapter outlines the methods used to design and fabricate the waveguides used in the nonlinear optical experiments. The waveguide theory and numerical techniques used to design the material structure and rib dimensions are described, as are the photolithography and etching processes.

3.1 GENERAL SLAB WAVEGUIDE THEORY

In order to maximise any nonlinear effects taking place in a waveguide, it is necessary to design the material structure in such a way that the mode area in the waveguides made in it is as small as possible. This section outlines the theory of the guiding of light in dielectrics (for more detail, see *Kogelnik 1979* and *Lee 1986*).

We first consider the conditions necessary for slab guiding to occur. The planar slab guide in Fig. 3.1 consists of a substrate of refractive index n_s, a film of refractive index n_f and a cover of refractive index n_c such that $n_f > n_s \geq n_c$. We assume that the light is monochromatic and coherent, and that the dielectrics are lossless and isotropic.

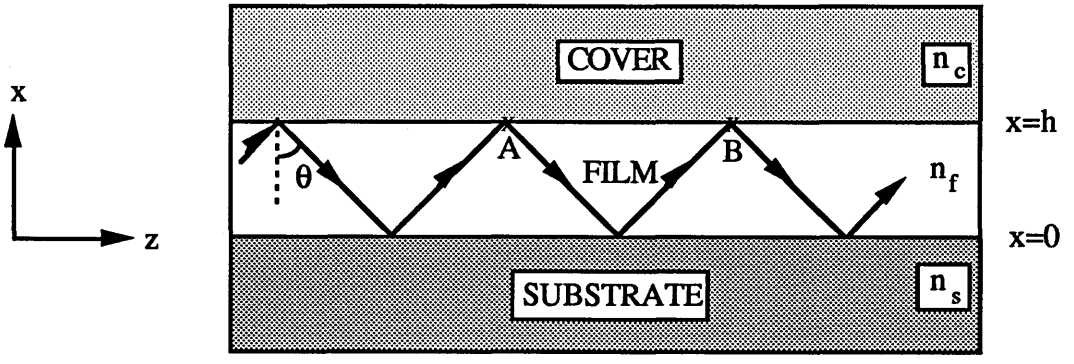

Fig. 3.1 Cross-section of a planar slab waveguide (after *Kogelnik 1979*).

In order for the light to be guided, it must experience total internal reflection at the film-substrate and film-cover layer. Consider a light beam in the film material impinging on the interface with the substrate material. By Snell's Law, total internal reflection of the light will occur if the angle of incidence of the light is greater than the critical angle defined as

$$\sin \theta_c = \frac{n_s}{n_f} \tag{3.1}$$

The propagation constant β of a guided mode in the film in the z-direction is defined as

$$\beta = k n_f \sin\theta = k n_e \tag{3.2}$$

where n_e is the effective refractive index in the film region, and so it can be seen to be bounded by the conditions

$$k n_s < \beta < k n_f \tag{3.3}$$

The transverse propagation constants can be defined for the three sections of the slab waveguide as

$$\kappa_c = \sqrt{\beta^2 - n_c^2 k^2} \tag{3.4}$$

$$\kappa_f = \sqrt{n_f^2 k^2 - \beta^2} \tag{3.5}$$

$$\kappa_s = \sqrt{\beta^2 - n_s^2 k^2} \tag{3.6}$$

The fields in the three regions are assumed to be of the forms

$$E_{y_c}(x, z) = E_c \exp\left[-\kappa_c(x-h)\right] \exp\left[-j\beta z\right] \qquad (x > h) \tag{3.7}$$

$$E_{y_f}(x, z) = E_f \cos\left[\kappa_f x - \psi\right] \exp\left[-j\beta z\right] \qquad (0 < x < h) \tag{3.8}$$

$$E_{y_s}(x, z) = E_s \exp\left[\kappa_s x\right] \exp\left[-j\beta z\right] \qquad (x < 0) \tag{3.9}$$

where ψ is a constant. Since both E_y and $\partial E_y/\partial x$ must be continuous across the boundaries at x=0 and x=h, we find that

$$\tan\psi = \frac{\kappa_s}{\kappa_f} \tag{3.10}$$

$$\tan(\kappa_f h - \psi) = \frac{\kappa_c}{\kappa_f} \tag{3.11}$$

and so, since $\tan(x)=\tan(x\pm m\pi)$, the dispersion relation may be found to be

$$\kappa_f h = \tan^{-1}\left(\frac{\kappa_c}{\kappa_f}\right) + \tan^{-1}\left(\frac{\kappa_s}{\kappa_f}\right) \pm m\pi \tag{3.12}$$

where m is an integer labelling the mode.

The bounds on β have already been shown to be $kn_s<\beta<kn_f$, and as β tends to kn_s, that is as κ_s tends to zero, guiding cuts off. We can therefore find the cutoff wavelength for a given mode by setting κ_s to zero in Eqn. 3.12, and by setting m to the number of the appropriate mode. This leads to the relation that at cutoff of the mth order mode

$$\kappa_f h = \tan^{-1}\left(\frac{\kappa_c}{\kappa_f}\right) \pm m\pi \tag{3.13}$$

The analogous equation to Eqn 3.12 can be found for TM polarised light by using the condition that H_y and $n^{-2}\partial H_y/\partial x$ must be continuous across the boundaries at x=0 and x=h. The dispersion relation for TM polarised light is thus found to be

$$\kappa_f h = \tan^{-1}\left(\frac{n_f^2 \kappa_c}{n_c^2 \kappa_f}\right) + \tan^{-1}\left(\frac{n_f^2 \kappa_s}{n_s^2 \kappa_f}\right) \pm m\pi \tag{3.14}$$

3.2 NUMERICAL METHODS

The theory in the previous section is exact for the case of slab guiding for either TE or TM polarised light. There is no equivalent exact form for the solution for guiding in rib or stripe guides. Examples of these types of guides, in which the light is confined laterally as well as vertically are shown below in Fig. 3.2.

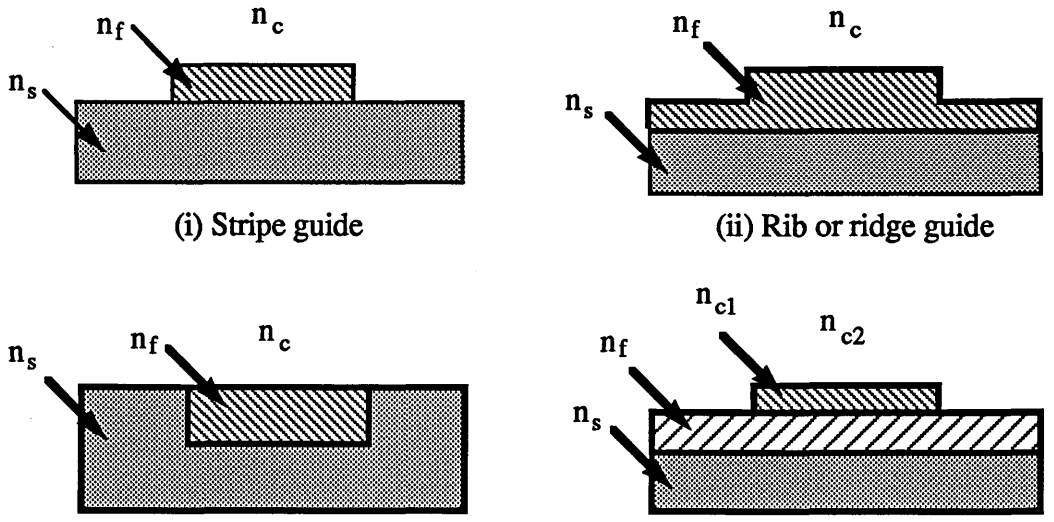

Fig. 3.2 Examples of different geometries used to confine light both vertically and laterally.

Numerical calculations can be performed by a number of methods to analyse the strip waveguide structure. The two numerical methods used to design the waveguides used in this thesis are described below:

3.2.1 EFFECTIVE INDEX METHOD

The effective index method is a relatively straightforward means of analysing a strip waveguide structure, although it is less accurate than most other numerical methods. In designing the material structure various parameters, such as the fraction of Aluminium in the cladding and the thickness of the layers, should be adjusted in order to determine which combination leads to optimum confinement of the light. The simplicity, and hence the speed, of the effective index method is a great advantage in doing this, and so this method was used for the preliminary material design, which was then checked and adjusted using the more accurate, but slower, numerical method described in Section 3.2.2.

The first stage of the effective index method is to find the effective index of the slab waveguide, as defined in Eqn. 3.2. Consider a rib waveguide made in this structure, as shown in Fig. 3.3.

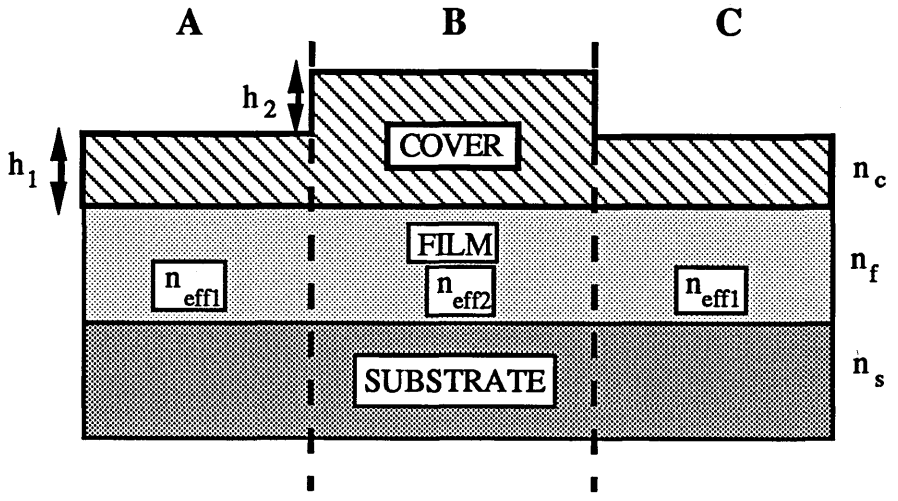

Fig. 3.3 Cross section of a three-layer rib waveguide

It can be seen from Eqn 3.12 that the effective index $n_e=\beta/k$ of the slab structure depends on the thickness of the guiding region. When a rib guide is used, the guiding layer is thicker under the rib, and so the effective index is different in regions A and C (n_{eff1}) from that in region B (n_{eff2}). When the effective indices of the different regions have been found, the structure can be imagined to be rotated by 90° to form a new slab waveguide, whose film refractive index is n_{eff2} and whose substrate and cover indices

are both n_{eff1}. This structure is then treated in the same way as the original slab waveguide, but using the orthogonal polarisation of the light, due to the imagined rotation of the waveguide.

The material for the waveguides used in this thesis is a four-layer structure, rather than the three-layer structure considered in Section 3.1, but the method used to solve this is almost identical to that described. The computer program used for this method was Fourlay, which was written by Bindi Bhumbra, formerly of this Department *(Bhumbra 1990).*

3.2.2 VECTOR FINITE DIFFERENCE METHOD

The finite difference method of solving the vector electromagnetic wave equation for a waveguiding structure is more accurate, but uses more computer time. The program FWave, written by Michael Taylor of this Department, was used to analyse the waveguide material structure after Fourlay had been used to design the structure roughly. The program splits the structure, which can consist of up to 100 layers of different refractive index, into a fine mesh. In order to speed up the program, the effective index method is used at first to gain an estimate of the initial field distribution. The second differentials in the Wave Equation are then approximated to a Taylor series expansion for each section of the mesh, and the resulting equations solved iteratively.

3.3 WAVEGUIDE DESIGN

In order to design the material structure for optimum confinement of the light, it is necessary to obtain accurate values for the refractive indices of the different layers involved. There are many reports in the literature of refractive index calculations and measurements for GaAs/AlGaAs bulk material *(Adachi 1985, Casey et al.1974, Afromowitz 1974 and Aspnes 1986)* and MQW material *(Chen 1987 and Sonek et al. 1986)*. There is some disagreement between the values quoted in these various publications, and it is not always easy to choose which values to use. As Stein Hansen of this Department had found, while carrying out refractive index measurements of MQW material, that the refractive index values found by using Adachi's model correlated most closely with his measurements, it was decided to use Adachi's model. When designing rib waveguides, the absolute values of refractive index are fortunately not as critical as the difference in refractive index between the layers, and so the choice of publication to use is not as critical as when designing structures such as gratings.

In order to find the refractive index of the MQW region, a weighted rms model was used *(Ohke et al. 1985)*. The refractive indices of the MQW section for TE and TM polarised light were found from the approximate equations

$$n_{TE} = \sqrt{\frac{n_w^2 L_w + n_b^2 L_b}{L_w + L_b}} \qquad n_{TM} = \sqrt{\frac{(L_w + L_b) n_w^2 n_b^2}{n_w^2 L_w + n_b^2 L_b}} \tag{3.15}$$

where L_w and n_w are the thickness and refractive index of the well regions, respectively, and L_b and n_b are the equivalents for the barrier regions. This expression is a good approximation when the number of periods in the MQW region is greater than about 50, and the MQW layer thicknesses are less than about 200 Å.

The material was designed to be single-moded vertically at both 1.06 μm and about 880 nm. This was because it had been hoped to carry out experiments using a Ti:Sapphire laser at about 880-900 nm, as well as the YAG laser at 1.06 μm. The material also should be single-moded laterally for rib widths of up to about 4 or 5 μm, in order that several different rib widths could be investigated experimentally, and also to allow for any errors in the design. The mode thickness was noted, as the design aimed for maximum confinement of the guided mode.

The optimum slab structure found when Fourlay (see Section 3.2.1) was used initially is shown in Fig. 3.4. Fourlay gives an exact solution for the vertical confinement of the light, and predicted this structure to be single-moded vertically to below 880 nm, with the vertical mode thickness about 1.7 μm at 1.06 μm. The 4 μm layer of AlGaAs is present in order to minimise the leakage of light from the guided mode into the GaAs substrate.

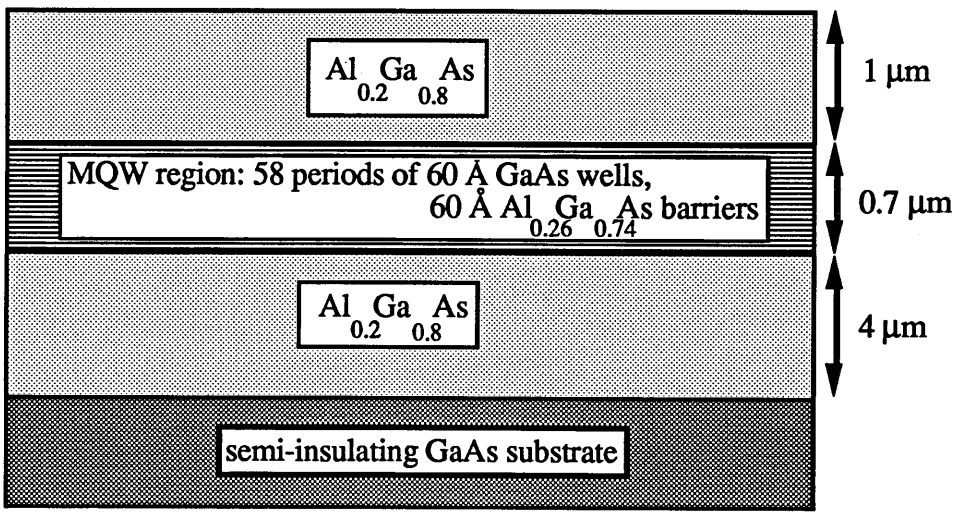

Fig. 3.4 Design for waveguide material

The solution for lateral confinement is only approximate, but predicted that, for an etch depth of 0.8 μm, the TE mode would be single-moded for a rib width less than about 4 μm, and the TM for less than about 3 μm. Similarly, for an etch depth of 0.6 μm, it predicted that both the TE and TM modes would be single-moded for a rib width less than about 5 μm, but for this case the lateral mode thicknesses were larger.

Once Fourlay had been used to design the slab structure shown in Fig. 3.4, FWave (see Section 3.2.2) was used to calculate the etch depth to give the best combination of the maximum rib width for which the guide is single-moded and the minimum mode thicknesses. This was found to be about 0.8 μm and Figs. 3.5 and 3.6 show examples of output plots from FWave for a structure with this etch depth.

The contours in Figs. 3.5 and 3.6 are of electric field. If the mode area is defined as the area in which the intensity is greater than half its maximum value, then this is the area contained by the three innermost contour rings, that is where the electric field is greater than 70% of its maximum value. The mode area was measured for various rib widths for both TE and TM polarised light, and was found to be about 4×10^{-12} m^2.

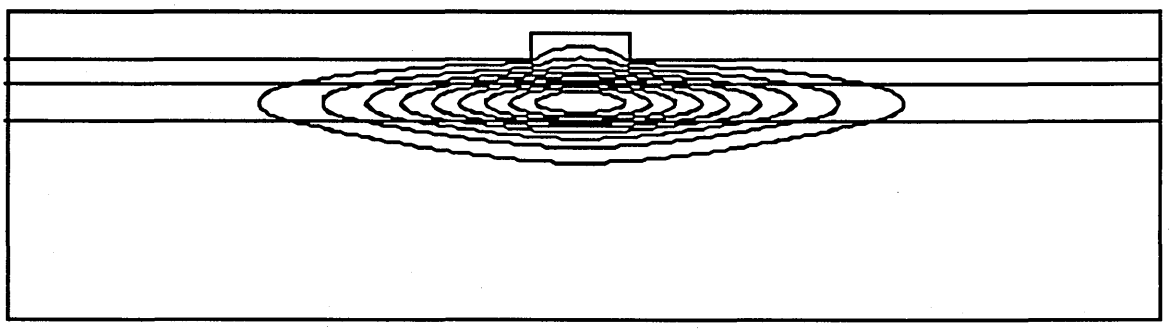

Fig. 3.5 Electric field contour plot of the lowest order even TE mode for a 2 μm wide rib and an etch depth of 0.8 μm

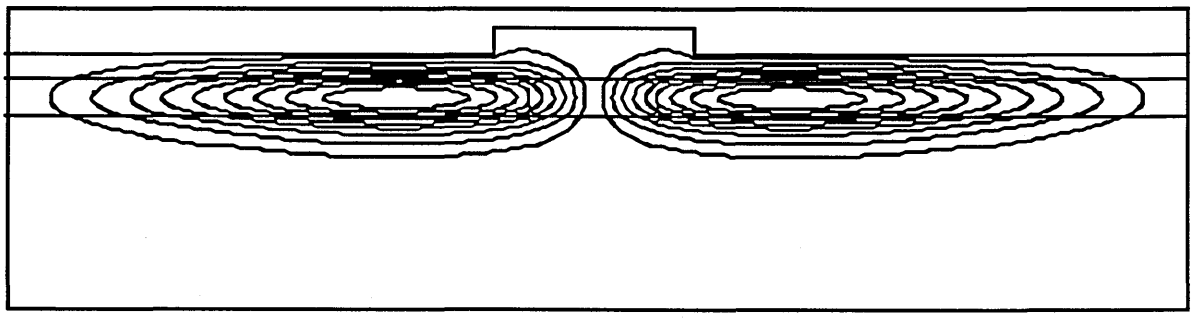

Fig. 3.6 Electric field contour plot of the lowest order odd TE mode for a 4 μm wide rib and an etch depth of 0.8 μm

3.4 PHOTOLITHOGRAPHY AND ETCHING

The waveguide structure of Fig. 3.4 was grown by MOVPE at the SERC Central Facility for III-V Semiconductors at Sheffield University. This growth technique involves exposing the sample to two or more chemically reactive gaseous compounds, such as trimethylgallium and arsine *(Herrenden-Harker and Williams 1986 and Jaros 1989)*.

The ribs were defined by photolithography, and the material around them etched away. Samples of about 11 mm x 2 mm were used, so that they would be about 10 mm long after cleaving. The processing steps are as follows:

(i) The samples were first cleaned thoroughly by soaking in an ultrasonic bath in turn in soapy deionised water, acetone, trichloroethylene, acetone, methanol and deionised water, each for five minutes. This stage is very important in order to remove dirt and dust, which might otherwise degrade the transfer of the pattern on the mask onto the resist.

(ii) Positive photoresist (Shipley S1400-17) was spun onto the material for 40 s at a speed of 4000 rev/min. This was found to give a uniform layer of resist about 0.5 μm thick.

(iii) The sample was baked in an oven at about 90°C for 30 mins in order for the solvents in the resist to evaporate, and to harden the photoresist.

(iv) A mask with micrometer stripes was placed touching the sample using a mask aligner, and the sample was exposed to ultraviolet light from a mercury lamp (365 nm) through the mask. The mask consisted of 19 lines whose widths varied in 0.5 μm steps between 1 μm and 10 μm. The distance between the centres of adjacent lines was 50 μm. The exposure time is critical, especially for narrow ribs, as if it is too short the uncovered resist may not be fully exposed, but if it is too long the resist under the mask may start to become exposed. An exposure time of about 2.5 s was found to give best definition. It is important that the mask is in very close contact with the sample if narrow lines of about 1 μm are to be exposed. This is because diffraction effects will lead to poor line definition if there is any air gap. It is also very important when fabricating waveguides to ensure that the mask is aligned so that the waveguides are perpendicular to the crystal cleavage planes.

(v) The sample was placed in a beaker of 1:1 microdeveloper: deionised water for about 75 s to remove the exposed photoresist.

(vi) The ribs were then produced by etching. Wet etching can be used, but the etch rate is extremely sensitive to temperature, stirring or the age of the etch. Dry etching was used for reproducibility, and also because the side walls of the ribs are more vertical for dry etching. Reactive Ion Etching (RIE) with $SiCl_4$ was used, and the etch rate found to be about 0.2 μm/min. This rate was found to vary from day to day, so that test samples were always etched first, in order to establish the etch rate before etching any waveguides.

(vii) The waveguides could then be cleaved. This was done by making a small nick in the sample in the desired cleavage direction using a diamond stylus, and then carefully applying pressure to the sample so that it cleaved along the crystal planes, to achieve a mirror-like facet.

Fig. 3.7 shows Scanning Electron Micrographs of the waveguides used for the experiments in this thesis, taken by Dave Gourlay of this Department. Fig. 3.7(a) shows the resist layer after exposure and development, but before etching. The ripples on the sidewalls of the resist are due to interference effects from the u.v. light used to expose the pattern. A completed rib waveguide is shown in Fig. 3.7(b), and it can be seen that the sidewalls are fairly vertical, but that they have inherited the same ripple pattern from the photoresist layer.

Figs 3.7(c) and (d) show the results of two different fabrication procedures. Both waveguides have been etched, but the resist layer has not yet been removed in acetone. The sample shown in Fig. 3.7(c) was postbaked for 30 minutes at 90°C after development and before etching, but the sample in Fig. 3.7(d) was not. There is a great difference in the quality of the two resist layers after etching, as may be seen in the photographs. Fig. 3.7(c) shows a smooth layer of resist which has been unaltered by the etching process, whereas the resist layer in Fig. 3.7(d) has been substantially damaged by the etch. However, it may also be seen from the two photographs that there is no apparent difference in the profile of the waveguides themselves. As far as can be seen, the sidewalls are equally vertical, with the same degree of ripple. Postbaking the resist causes it to crosslink, which makes it more difficult to remove, and so it was decided not to do this. Another advantage of not postbaking the samples was that one of the stages at which the waveguides might become contaminated was removed.

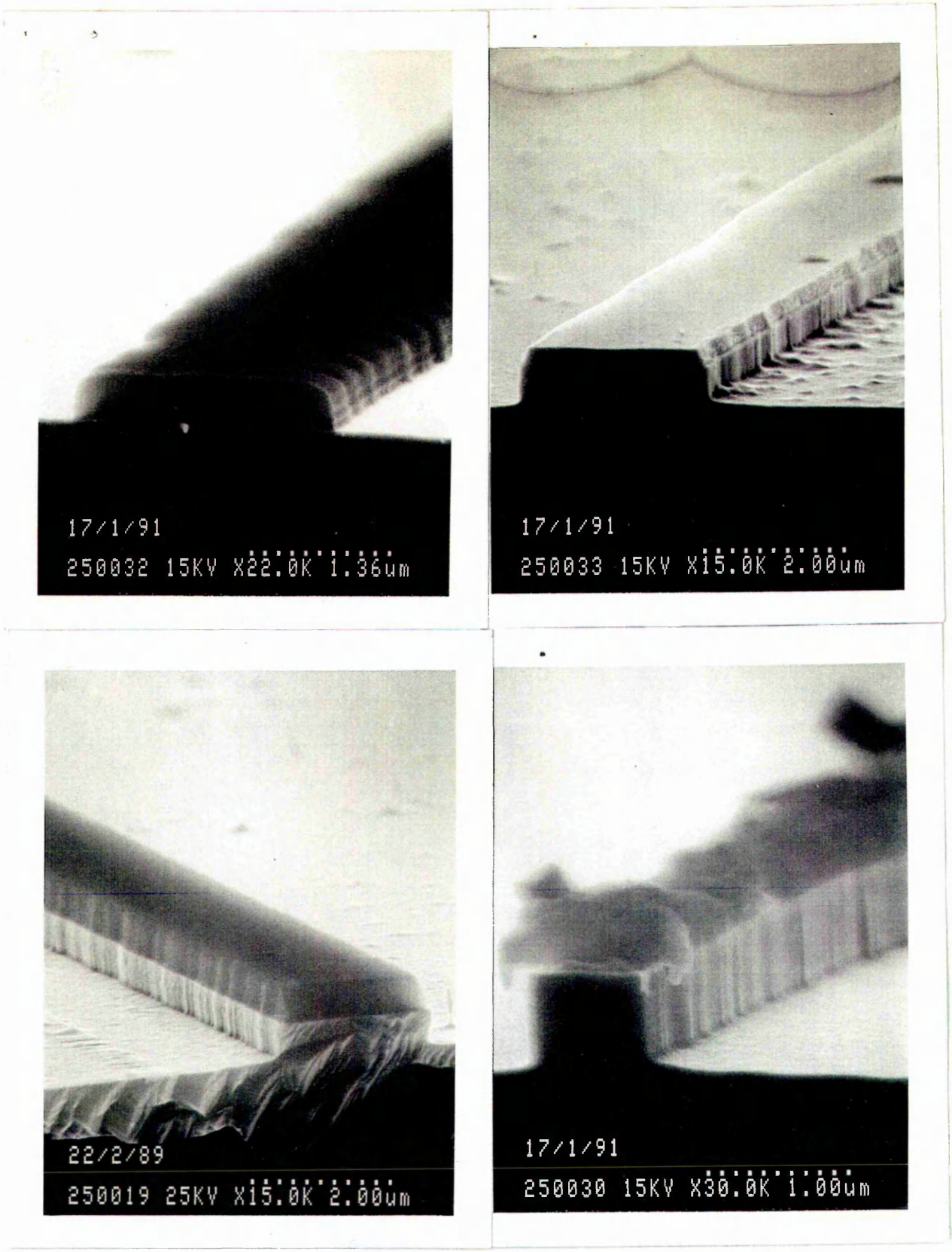

Fig. 3.7 Scanning Electron Micrographs of waveguides in various stages of the fabrication process. Fig. 3.7(a) shows a resist layer before etching, and (b) shows a waveguide which has been etched, and the resist layer removed. Photographs (c) and (d) show etched waveguides before the resist has been removed. The waveguide in (c) was postbaked before etching, while that shown in (d) was not.

CHAPTER FOUR
EXPERIMENTAL SET-UP

This chapter describes the preliminary experiments carried out on the waveguides in order to assess them. The laser system used is described, as are the methods used to characterise the waveguide material quality, namely loss, photoluminescence and transmission measurements.

4.1 LASER SYSTEM

4.1.1 YAG LASER

The laser used for the experiments in this thesis was a Quantronix 416 Nd^{3+}:YAG laser, lasing at 1.064 μm, with a maximum cw output power of about 5 W. When the laser was modelocked at a frequency of 76 MHz, the pulsewidth was about 100 ps, and the peak power was about 700 W. When it was used modelocked and Q-switched, the modelocked pulses were contained by an envelope of about 250 ns, and the peak power was about 500 kW.

4.1.2 KTP CRYSTAL

The laser was used cw modelocked for all the nonlinear optical experiments, and the quality of the modelocking was monitored very carefully, as it was necessary for the peak laser intensity to be as high as possible in order for nonlinear effects to be maximised. At first, an InGaAs photodiode with a typical FWHM of 65 ps was used to monitor the pulsewidth, but this was found to be insufficient to ensure optimum modelocking. This was because the active area of the photodiode had a diameter of only 100 μm, so that when the mirrors were adjusted to peak up the modelocking, the laser spot would be deflected away from this small area. This meant that the signal from the photodiode would fall, even if the mirrors had been moved in such a way as to enhance the modelocking.

It was found to be much more effective to use a KTP crystal to frequency-double the YAG beam, and to gauge the quality of modelocking from the intensity of this green light. A beamsplitter was put in the laser beam to reflect 10% of the YAG light. This was then focussed onto a KTP crystal, and the orientation and position of the crystal

carefully adjusted to optimise the efficiency of the frequency-doubling process. The light emerging from the crystal passed through a filter to remove any light at 1.06 μm, the green light was detected by a photomultiplier tube, and the signal displayed on an oscilloscope. It was found to be relatively easy with this arrangement to achieve modelocked pulses which were as narrow and stable as possible.

4.1.3 AUTOCORRELATION

It was only possible to gain an approximate measure of the modelocked pulsewidth using the InGaAs detector and a sampling oscilloscope. The minimum measurable FHWM of the pulses was limited to about 120 ps by the rise times of the photodiode (about 45 ps) and the sampling head (about 30 ps) and by timing jitter in the oscilloscope and the mode-locked pulses. An autocorrelator was therefore used *(Sala et al. 1980)*, as shown in Fig 4.1.

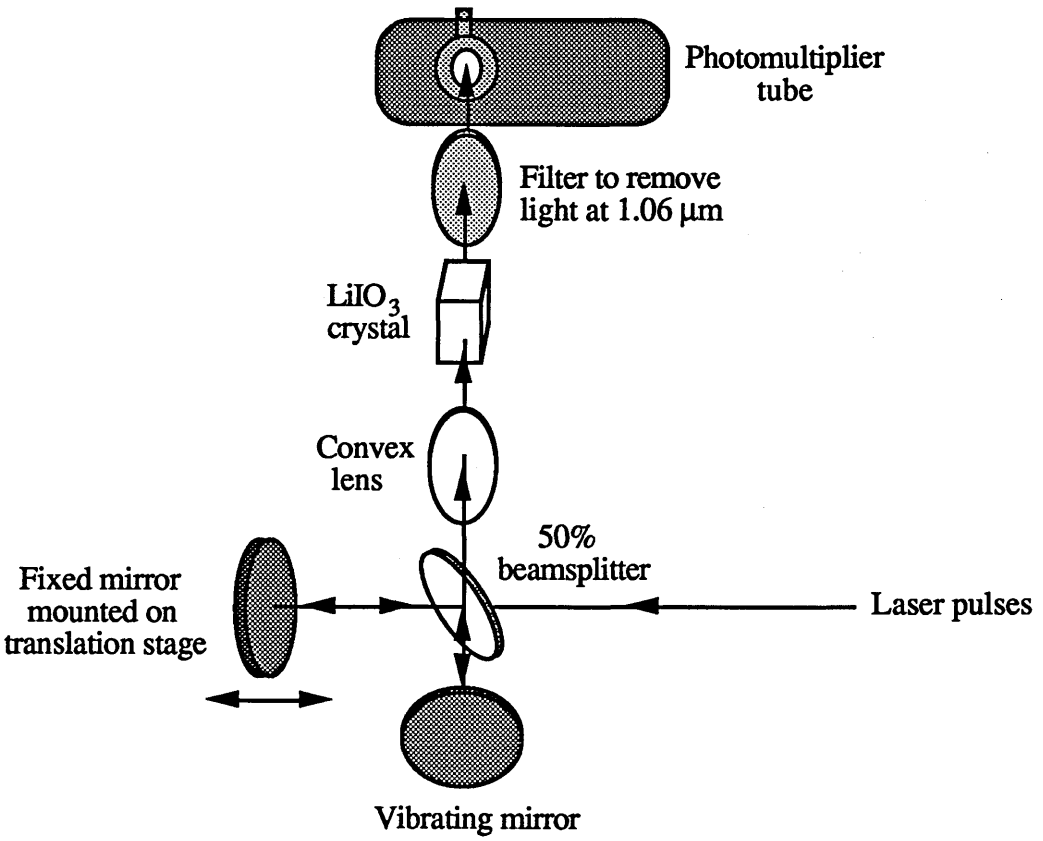

Fig 4.1 Schematic of an autocorrelator

When each modelocked laser pulse enters the autocorrelator, it is divided at the beamsplitter, and the beams travel different distances before recombining and being focussed into the nonlinear crystal ($LiIO_3$ cut at 34° for use with a YAG laser). The

intensity of the frequency-doubled light generated by the crystal is proportional to the square of the peak input intensity, and hence dependent on the degree of overlap of the two beams. If one of the mirrors is made to vibrate, the path length for one beam will change periodically, which will change the overlap between the beams, and the intensity of the second harmonic radiation, so that an autocorrelation function is generated. This can be displayed on an oscilloscope and, from a knowledge of the input pulse shape, the pulse width can be easily obtained.

Because the laser pulsewidth was about 100 ps (the time for light to travel 3 cm) and the travel on the vibrator was only ±2.5 mm, it was found necessary to adapt slightly the method described above. The two beams should be separated enough that the FWHM of the modelocked pulses can be measured, and so the mirror which would normally vibrate was kept stationary, and the mirror which would normally be kept stationary was moved manually using the 25 mm translation stage. The total travel in this arm of the autocorrelator was therefore 50 mm, corresponding to a time of 167 ps. An autocorrelation plot obtained in this way for the YAG laser is shown in Fig. 4.2.

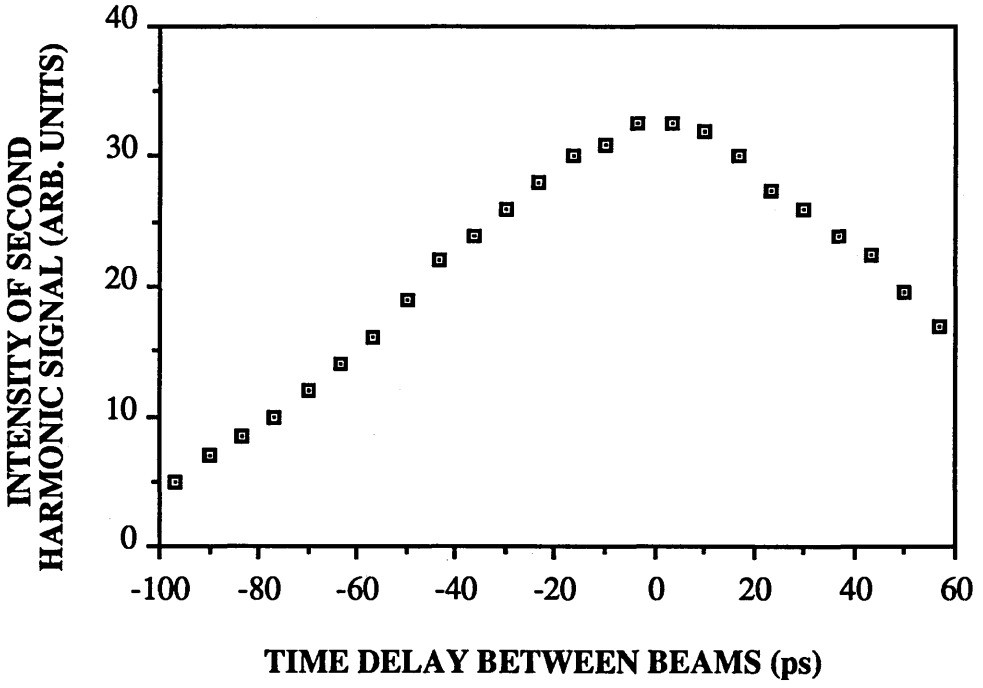

Fig. 4.2 Autocorrelation trace of modelocked YAG pulses.

The FWHM of this plot is about 126 ps, and this can be converted to the FWHM of the actual modelocked pulses by dividing by $\sqrt{2}$ for Gaussian pulses, giving a FWHM of 89 ps. This is in line with the specifications of the laser.

4.2 MATERIAL CHARACTERISATION

4.2.1 PHOTOLUMINESCENCE

Photoluminescence spectra of the material were taken in order to find out the energy of the excitonic resonances and the band edge, and to assess the material quality. Photoluminescence occurs when the absorption of photons leads to the formation of hot carriers. These relax by phonon emission and recombine by the emission of photons at lower energy than the pumping photon energy *(Wilson and Hawkes 1983)*. The spectra were taken by John Cochrane of this Department. The excitation photons were from a He-Ne laser at 633 nm, and the resulting photoluminescence was focussed into a 1 metre monochromator, which was scanned through the wavelength range requested. The signal from the monochromator fell onto a Ge photodetector, and then via a lock-in amplifier to a chart recorder.

Figs. 4.3 to 4.5 show photoluminescence spectra of the waveguide material used for the experiments of this thesis at 20 K and room temperature respectively. In Fig. 4.3, the heavy hole exciton resonance can be seen at about 789 nm at 20 K, with a FWHM of about 27 Å (4.7 meV), and in Fig. 4.5, it is seen to be at about 840 nm at 300 K. This value for the FWHM is in very good agreement with that of 4 meV found from the empirical equation for the temperature dependence of the half width at half maximum Γ of the heavy hole exciton *(Chemla et al. 1984)*:

$$\Gamma = \Gamma_0 + \frac{\Gamma_{ph}}{\left[\exp\left(\frac{\hbar\Omega_{LO}}{kT}\right) - 1\right]} \qquad (4.1)$$

where $\hbar\Omega_{LO}$ =36 meV is the energy of the LO-phonon in GaAs, Γ_0=2 meV is a constant inhomogeneous term and Γ_{ph}=5.5 meV is a proportionality constant. The inflection at about 832 nm in the 298 K spectrum is attributed to the light hole exciton, although it should be noted that this value is very approximate. At 20 K, there is a bulk GaAs peak at 818 nm and a peak due to carbon impurities in the GaAs at 828 nm.

The two peaks at 695 nm and 686 nm at 20 K seen in Fig. 4.4 are attributed to the bulk $Al_{0.2}Ga_{0.8}As$ material of the cladding region and the $Al_{0.26}Ga_{0.74}As$ barriers of the MQW region, respectively. When these values were inserted into a computer program Xton *(Bhumbra 1990)*, written by Bindi Bhumbra, formerly of this Department, it was found that a peak at 695 nm at 20 K corresponds to the bulk material having a composition of $Al_{0.18}Ga_{0.82}As$, while a peak at 686 nm corresponds to the barrier material being $Al_{0.2}Ga_{0.8}As$.

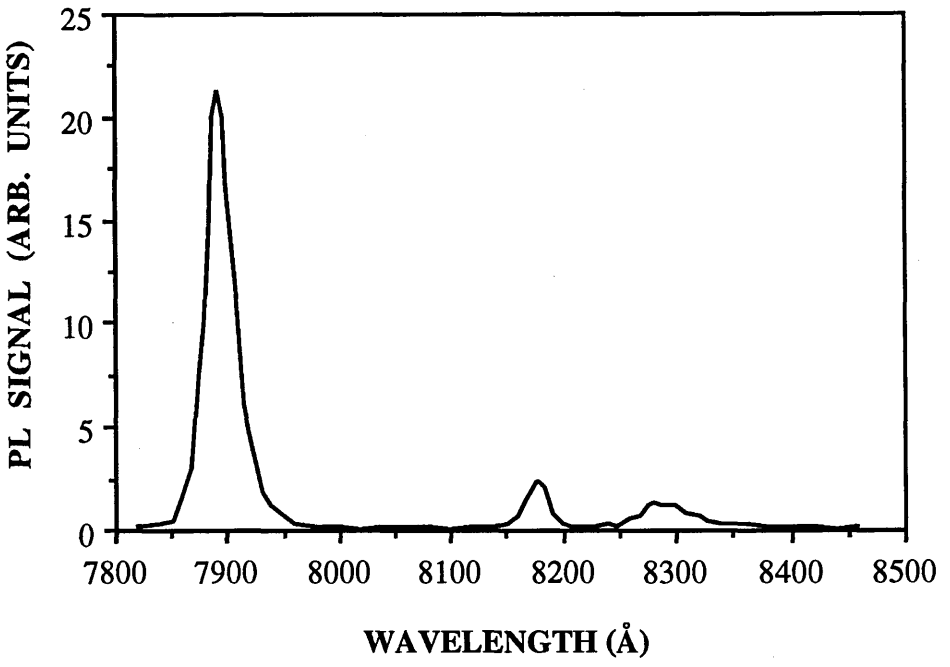

Fig. 4.3 PL plot at 20K, showing peaks for the quantum well GaAs exciton resonances, bulk GaAs and Carbon impurities

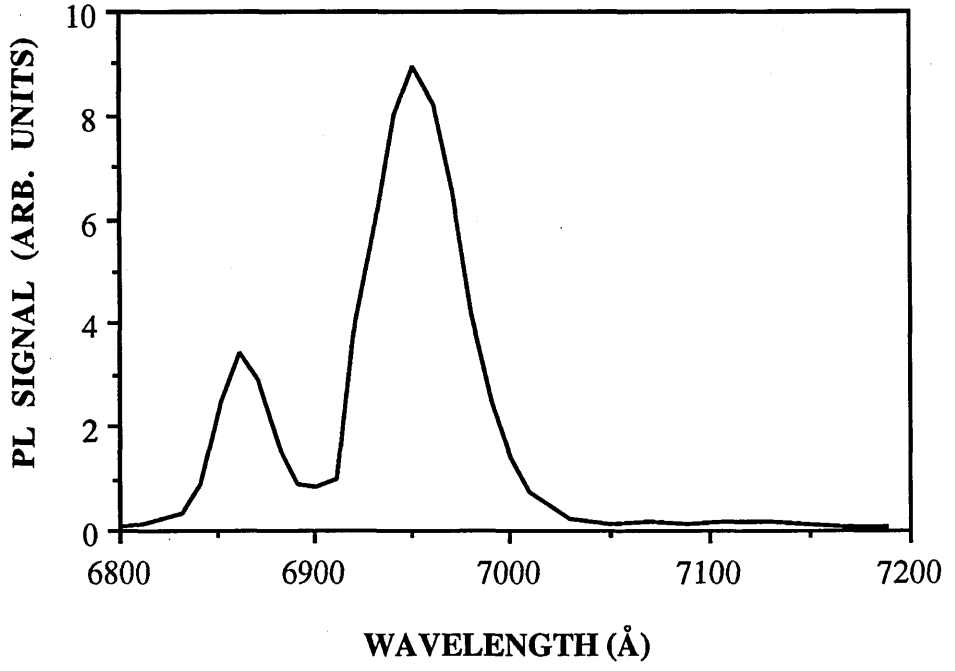

Fig. 4.4 PL plot at 20K, showing peaks for the AlGaAs exciton resonances

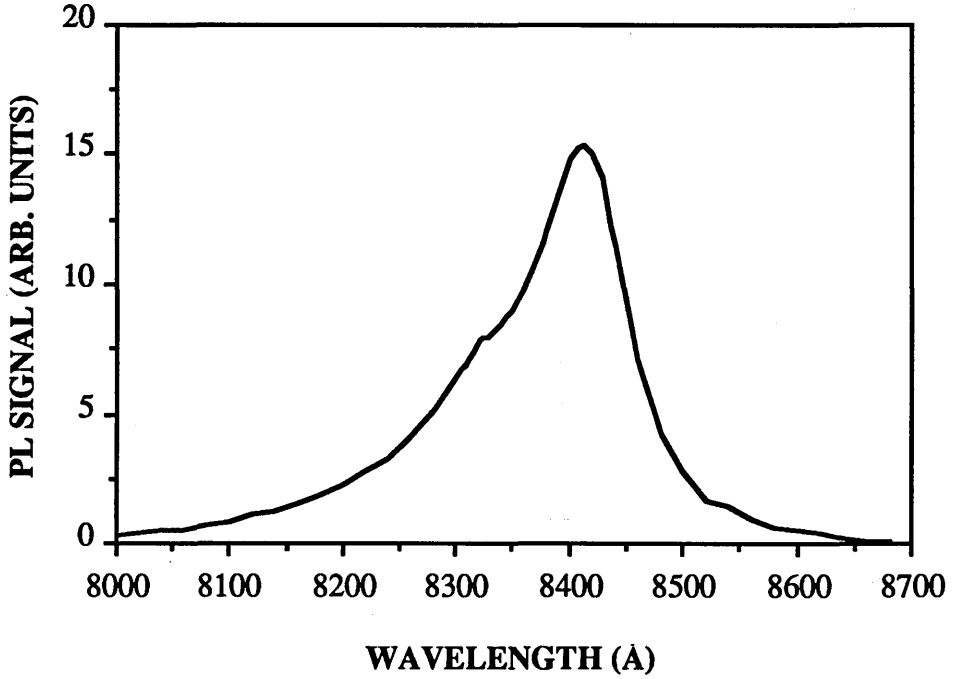

Fig. 4.5 PL plot at room temperature, showing the heavy and light hole excitonic resonances

The barrier material in the MQW section was therefore believed to be $Al_{0.2}Ga_{0.8}As$, and the well material GaAs. The program Xton was run with these values for various well widths, and the wavelengths at which the program predicted the heavy and light hole exciton resonances were noted. The well width for which the program predicted exciton transitions closest to those observed experimentally in the photoluminescence plots was 70 Å. For this case, the program predicted the heavy hole exciton transition to be at 840 nm and the light hole exciton transition to be at 836 nm.

This well width was confirmed by John Roberts, of the Department of Electronic and Electrical Engineering of the University of Sheffield, where the material had been grown, who indicated that photovoltage spectra of the material had also shown that the well width was 70 Å.

4.2.2 TRANSMISSION MEASUREMENTS NEAR THE EXCITON RESONANCE

In order to further assess the material quality, and to check the position of the exciton resonances, transmission measurements were taken near the band edge. The experimental arrangement (as shown in Fig. 4.6) was set up by Stein Hansen and Jacques Beauvais of this Department, and the transmission experiments were carried out with them.

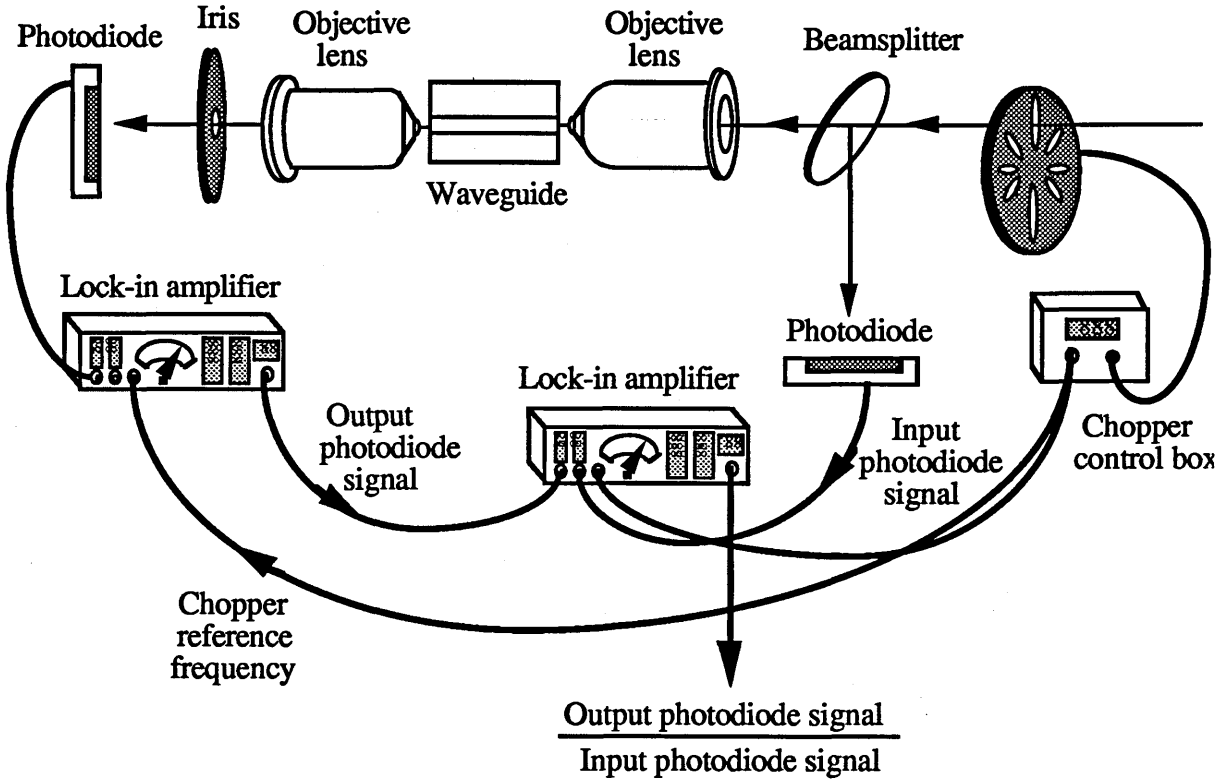

Fig. 4.6 Experimental arrangement for linear transmission measurements

The input and output intensities from the waveguide were measured by the two photodiodes. The signal from the photodiode which measured the output intensity was passed into a lock-in amplifier, whose reference frequency was that of the chopper. The output from this was then connected to one of the input ports of another lock-in amplifier, and the signal from the photodiode which measured the input intensity was fed into the other port. This second lock-in amplifier acted as a ratiometer, so that it divided the signal from the output photodiode by the signal from the input photodiode. In this way, the measurement was automatically normalised for the laser's spectral response. It was also set to give a logarithmic response, in order to show more detail in the transmission plot by magnifying any small variations in transmission.

The resulting logarithmic transmission plots for both TE and TM polarisations are shown in Figs. 4.7 and 4.8.

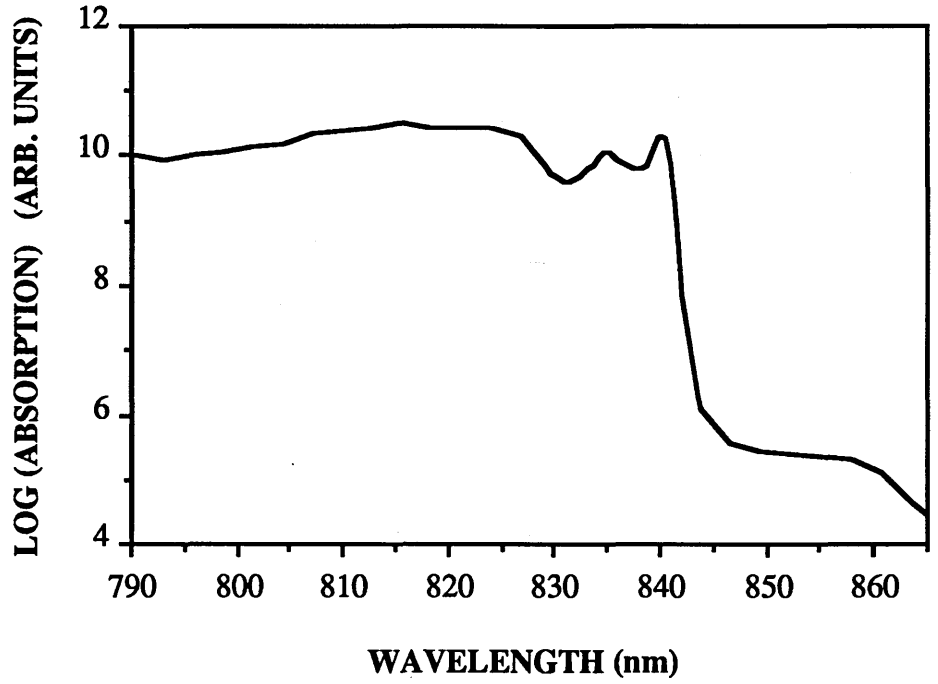

Fig. 4.7 Logarithmic transmission plot for TE polarised light

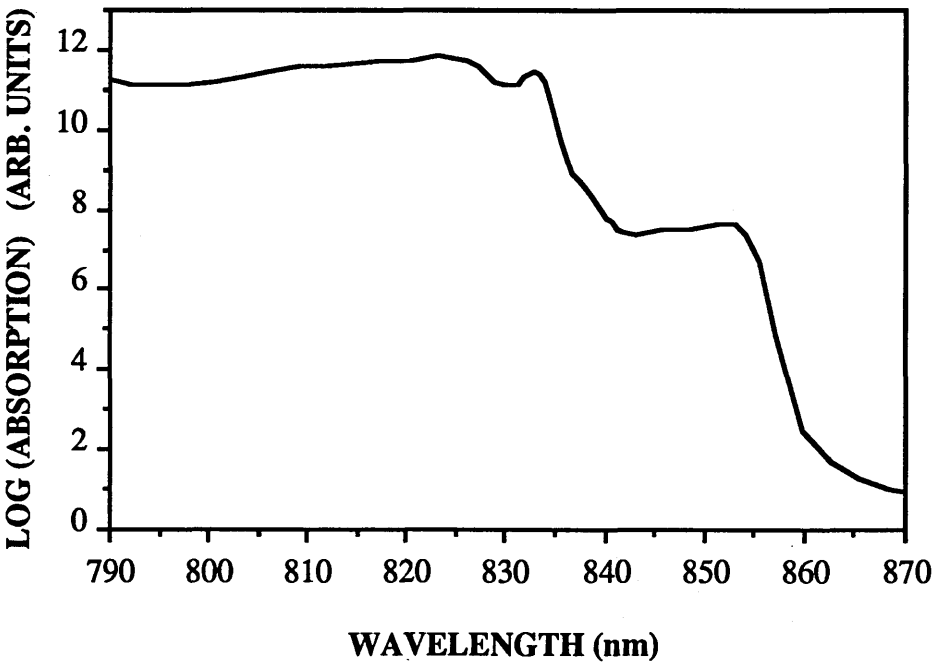

Fig. 4.8 Logarithmic transmission plot for TM polarised light

In the TE plot of Fig. 4.7, both the heavy hole and light hole exciton resonances are clearly visible, whereas only the light hole exciton resonance exists in the TM plot of Fig. 4.8. This is consistent with accepted theory *(Chemla 1985)*, as is the observation that in Fig. 4.7, the heavy hole exciton resonance is more distinct than that of the light hole (for TE polarised light, the optical transition matrix elements from the heavy and light hole bands to the conduction band are in the ratio 3:1 respectively).

The TE plot shows the heavy and light hole exciton resonances to be at about 841 and 835 nm respectively, and the TM plot shows the light hole resonance to be at about 834 nm. These values are very close to those obtained from the photoluminescence measurements of 840 nm for the heavy hole exciton resonance and 832 nm for that of the light hole, given the large uncertainty in the latter value from the photoluminescence plot. From the photoluminesence and transmission measurements, the actual structure of the waveguide material can therefore be deduced, and is shown in Fig. 4.9.

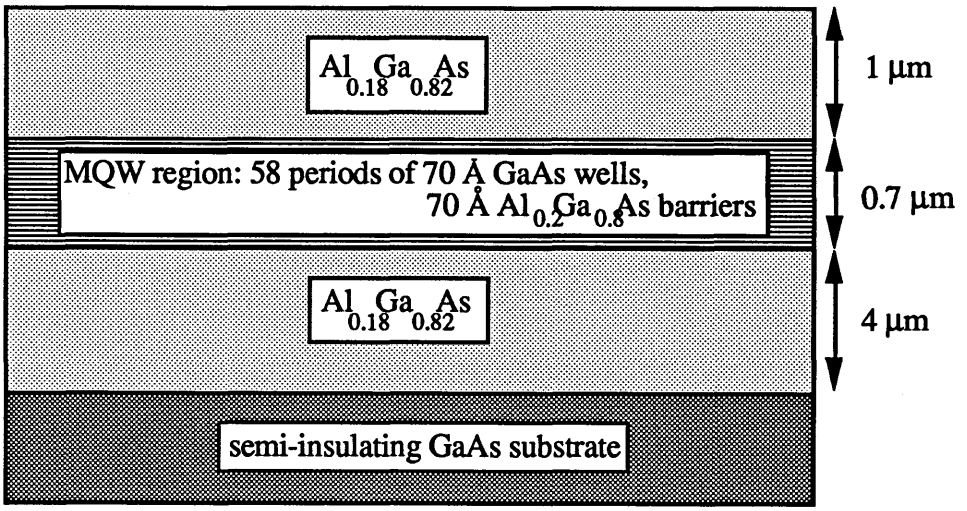

Fig. 4.9 Actual structure of material used to fabricate waveguides

4.3 WAVEGUIDE CHARACTERISATION

4.3.1 END-FIRE COUPLING

Laser light was launched into the waveguides by means of end-fire coupling. In order to optimise the coupling efficiency into the waveguide mode, the overlap integral between the mode profile of the laser beam and that of the waveguide must be maximised. Objective lenses of x10, x20 and x40 magnifications were tested and it was found that x20 and x40 lenses led to approximately equal coupling efficiencies, which were greater than that of x10 lenses. It was decided to use x20 objectives because the area of the focussed spot was larger than that of x40 lenses, so that the intensity incident on the waveguide would be smaller and the waveguides would be less likely to be burnt.

The coupling efficiency is extremely sensitive to the position of the lenses, and so the lenses were mounted on translation stages with differential drives whose resolution was about 0.1 μm. Both the input and output lenses could be independently adjusted to optimise focussing and alignment, and the sample could also be translated and rotated independently of the lenses. When aligning a waveguide, the output light was sent to an infra-red camera and V.D.U. The camera's line scan facility was used to monitor the intensity in the waveguide and hence to optimise the coupling efficiency, and the mode profile was also observed.

4.3.2 COMPUTER CONTROL OF THE EXPERIMENTS

The experiments were all controlled by an IBM XT-286 computer in order to simplify and speed up the acquisition of data. Software was written to enable the analogue to digital conversion board to be used to read data from power meters both before and after the waveguide and also from the lock-in amplifier, which was used to measure the signal from a photodiode. An RS232 interface was also accessed by the same software to control a stepper motor which varied the pump-probe delay time.

4.3.3 PELTIER TEMPERATURE CONTROLLER

When nonlinear optical experiments were first carried out, one of the most serious problems was that the waveguides were easily destroyed by the high intensities launched into them. Fig. 4.10 shows some examples of ribs burnt by the laser.

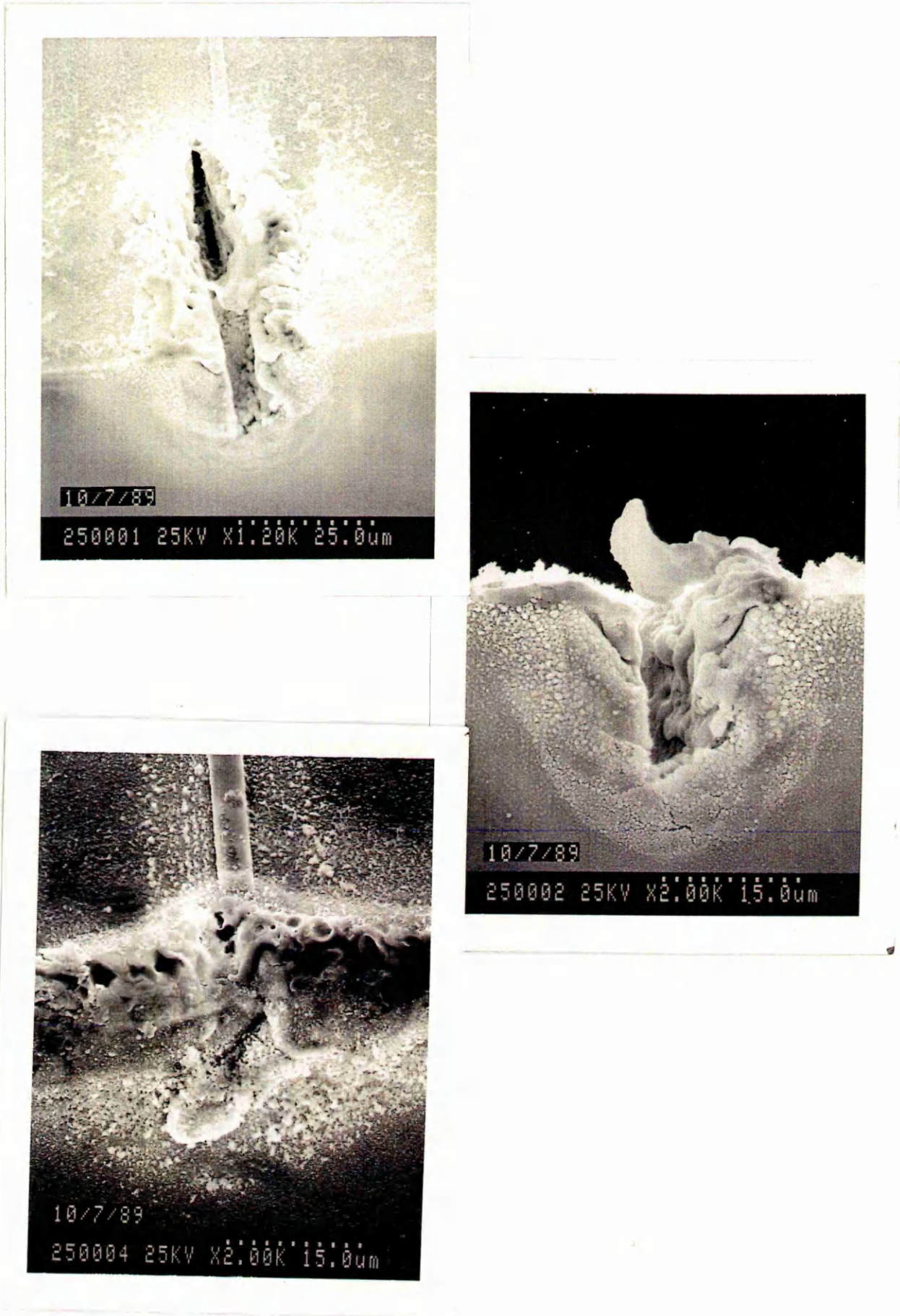

Fig. 4.10 Photographs of rib waveguides burnt by the YAG laser beam

As it was believed that the problem of the waveguides burning was due to the laser beam's heat not being dissipated quickly enough, the waveguides were then mounted on a Peltier device, which consists of sections of n- and p-type semiconductor separated by ohmic contacts. (The semiconductor usually used is Bismuth Telluride, as the Peltier Effect is particularly strong in this material *(RS data sheet 1987)*) Consider an n-type semiconductor with ohmic contacts on either side, as shown in Fig. 4.11.

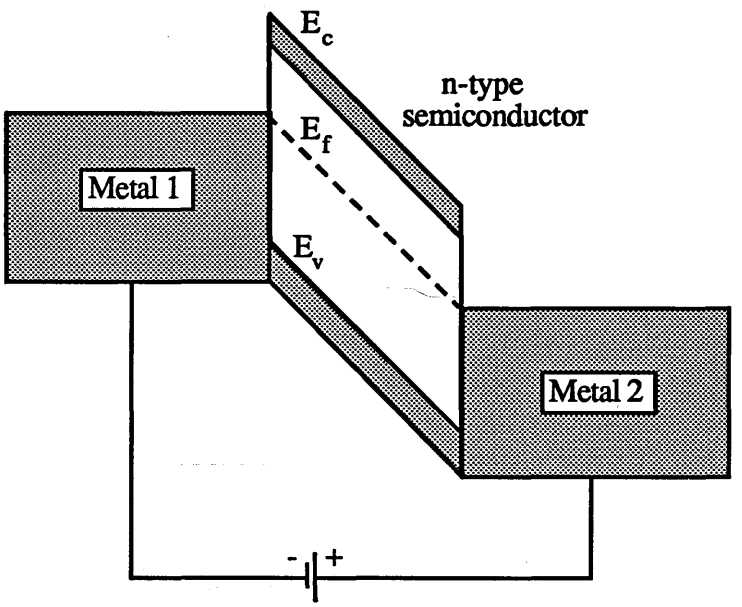

Fig. 4.11 Band structure of an n-type semiconductor with ohmic contacts *(after Azaroff and Brophy 1963)*

It may be seen from the band structure in Fig. 4.11 that only the higher energy electrons of Metal 1, i.e. the "hotter" electrons, can overcome the potential barrier, and so pass to Metal 2. In this way, Metal 1 becomes cooler, and Metal 2 hotter. This is known as the Peltier Effect, discovered in 1834 by Jean Peltier *(Azaroff and Brophy 1963)*.

Fig. 4.12 shows the waveguide mounted on the Peltier device. Because the currents in the n-type and p-type elements flow in opposite directions (with respect to the cold junction), it can be seen that heat will pass to the bottom of the controller, and the top will become cooler. Similarly, if the polarity of the applied voltage is reversed, the direction of heat flow will also be reversed. The copper block is present to raise the waveguide to the height of the objective lenses, and the heatsink removes the heat pumped away from the waveguide by the Peltier device. The various components of Fig. 4.12 are joined by high thermal conductivity heat sink compound, in order to assist the heat flow. The waveguide temperature is measured by means of a thermistor inserted in a small hole near the top of the copper block, and a feedback loop in the temperature

controller acts so as to stabilise the temperature by applying a voltage of the appropriate magnitude and polarity to the Peltier device. In this way, the waveguide temperature can be set to any temperature desired, between about -20 and 50 °C. The temperature was set to about 30°C, and this setting remained fixed throughout the experiments.

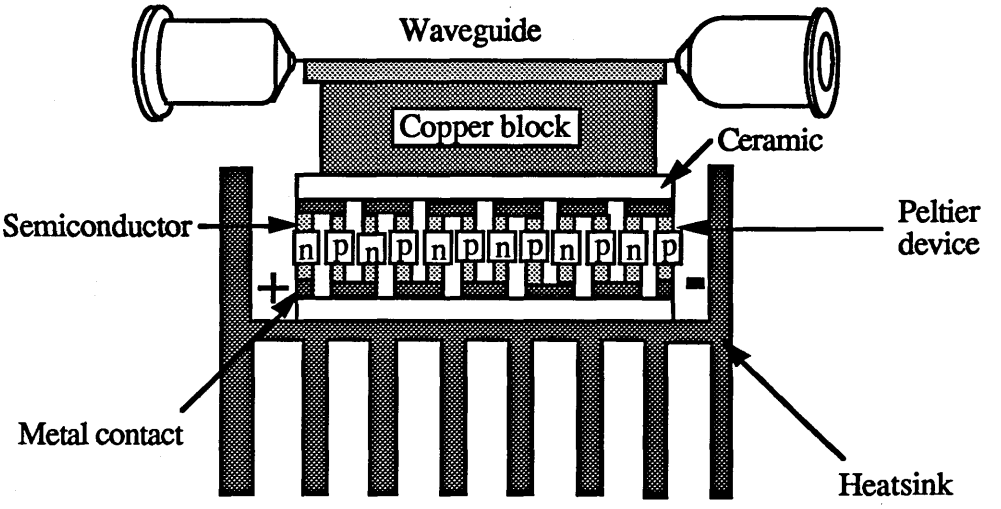

Fig. 4.12 Peltier device as used to control the waveguide temperature

The gain and the time constant of the controller's feedback loop could be adjusted independently, and were found to be critical in ensuring that the waveguides did not burn. If the gain was too high, or the time constant too short, the controller would be oversensitive to any change in temperature recorded by the thermistor, and would overshoot the set temperature. If the gain was too low, or the time constant too long, the controller would be too sluggish in its response to the thermistor resistance. In either case, the waveguides would still be destroyed by the laser beam. When the optimum settings were found, the waveguides were extremely resistant to damage, and experiments could be carried out using higher peak intensities than previously.

4.3.4 WAVEGUIDE MODE PROFILES

The waveguides had been designed to be single moded, in order to maximise the peak intensity under the rib. Their actual mode profile could be checked by viewing the output beam with an infrared camera and monitor. The order of the transverse mode depended on the rib width, and Fig. 4.13 shows examples of a single-moded and a double-moded waveguide. The material used for the waveguides shown in Fig. 4.13 was nominally identical to that shown in Fig. 3.4, except that the cladding layer was not present. This meant that there was no slab guiding between the ribs, so that the laterally-confined modes under the ribs were much clearer.

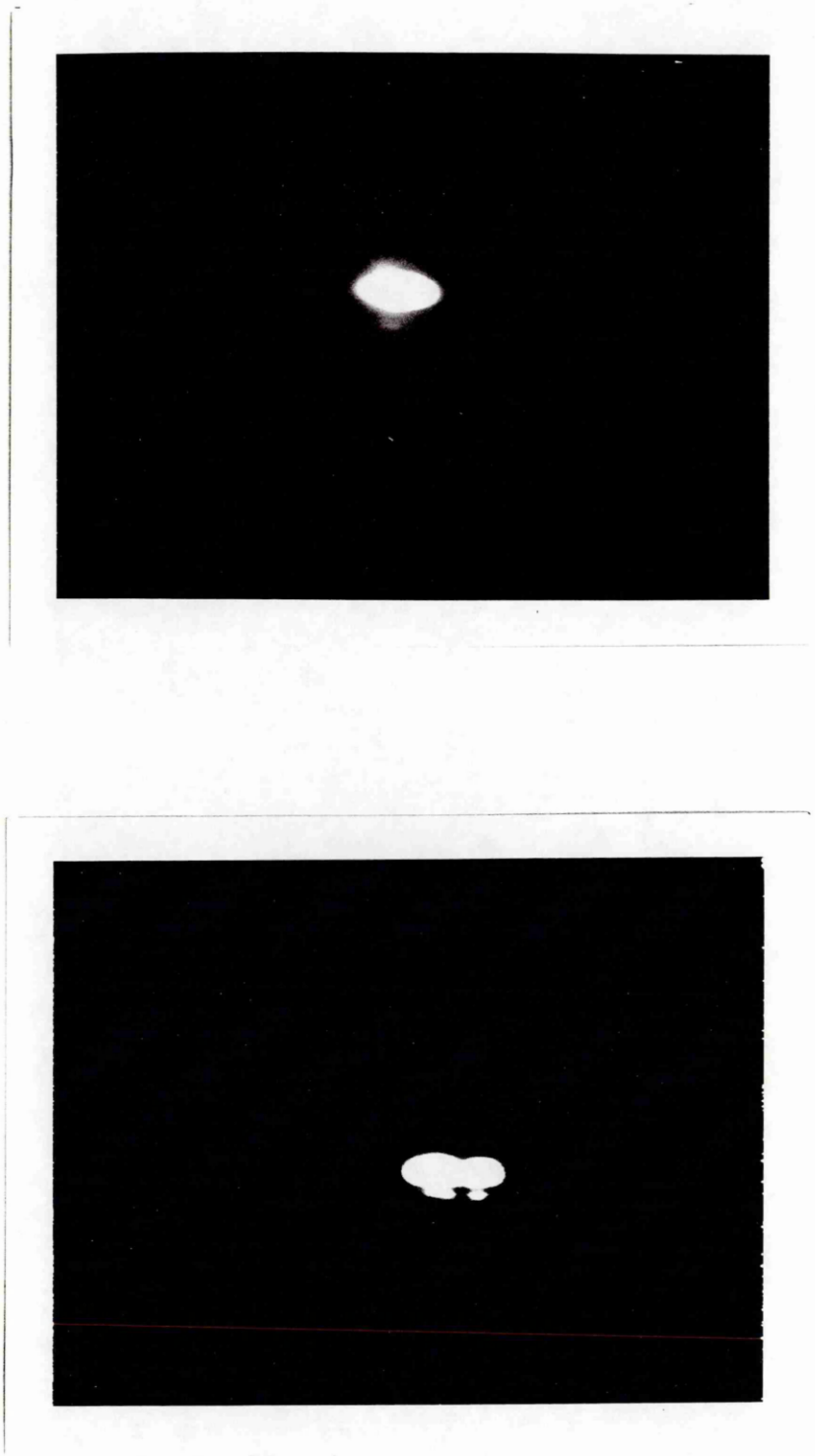

Fig. 4.13 Photographs of the output beam from a single-moded and a double-moded waveguide

4.3.5 WAVEGUIDE LOSS MEASUREMENTS

(i) SEQUENTIAL CLEAVING

The loss of a waveguide can be measured by making transmission measurements of a number of different lengths of the same waveguide structure. The YAG laser was used cw when making these measurements, in order that any nonlinearities can be neglected. The output power from the waveguide can then be written as

$$P_{out} = P_{in} e^{-\alpha L} \tag{4.2}$$

where P_{in} and P_{out} are the input and output powers respectively within the waveguide, α is the linear absorption coefficient and L is the length of the waveguide. The way in which the measurements were made is shown in Fig. 4.14.

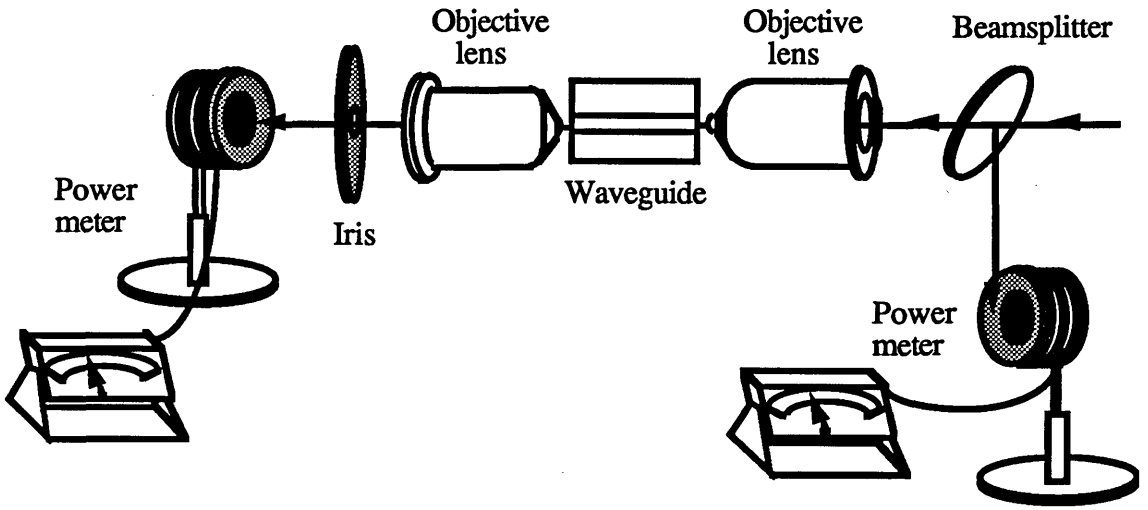

Fig. 4.14 Experimental setup for sequential cleaving waveguide loss measurement

It can be seen that the input and output powers measured by the two power meters are not equal to P_{in} and P_{out} in Eqn. 4.2, but are proportional to them. We can therefore rearrange Eqn. 4.2 to give

$$\ln\left(\frac{P'_{in}}{P'_{out}}\right) = \ln K + \alpha L \tag{4.3}$$

where P_{in}' and P_{out}' are the input and output powers as measured by the power meters positioned as in Fig. 4.14, and K is the proportionality factor linking these powers with P_{in} and P_{out} in Eqn. 4.1. If a graph is plotted of $\ln(P_{in}'/P_{out}')$ against L, then the absorption coefficient α can be found from the gradient. Figs. 4.15 and 4.16

show two such graphs used to find the loss of the waveguides used in this thesis for TE and TM polarised YAG laser light respectively.

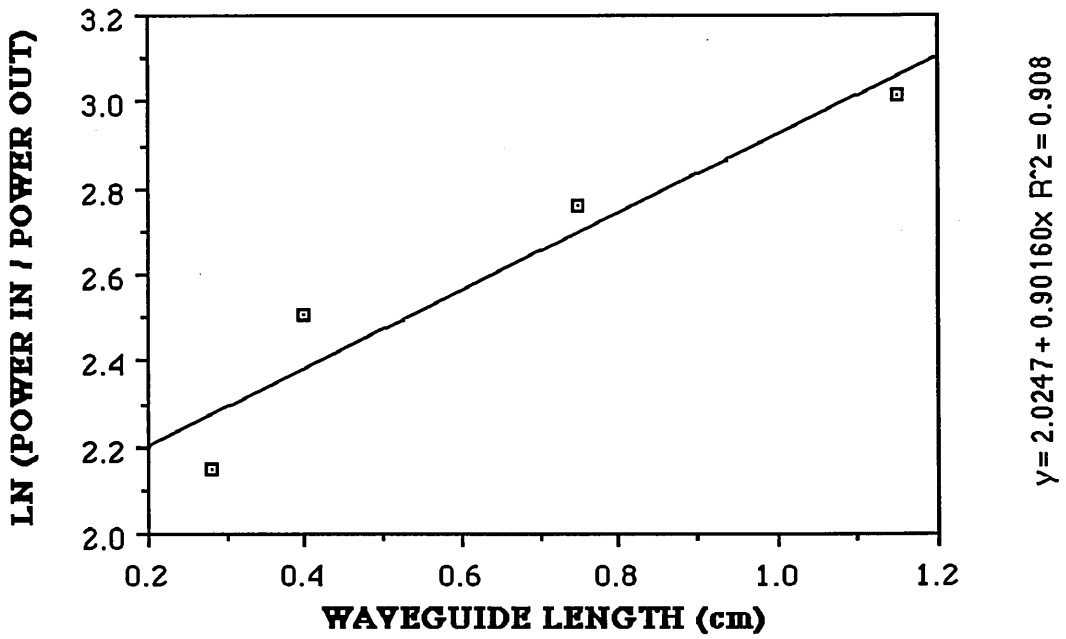

Fig. 4.15 Sequential cleaving plot for TE polarised YAG laser light

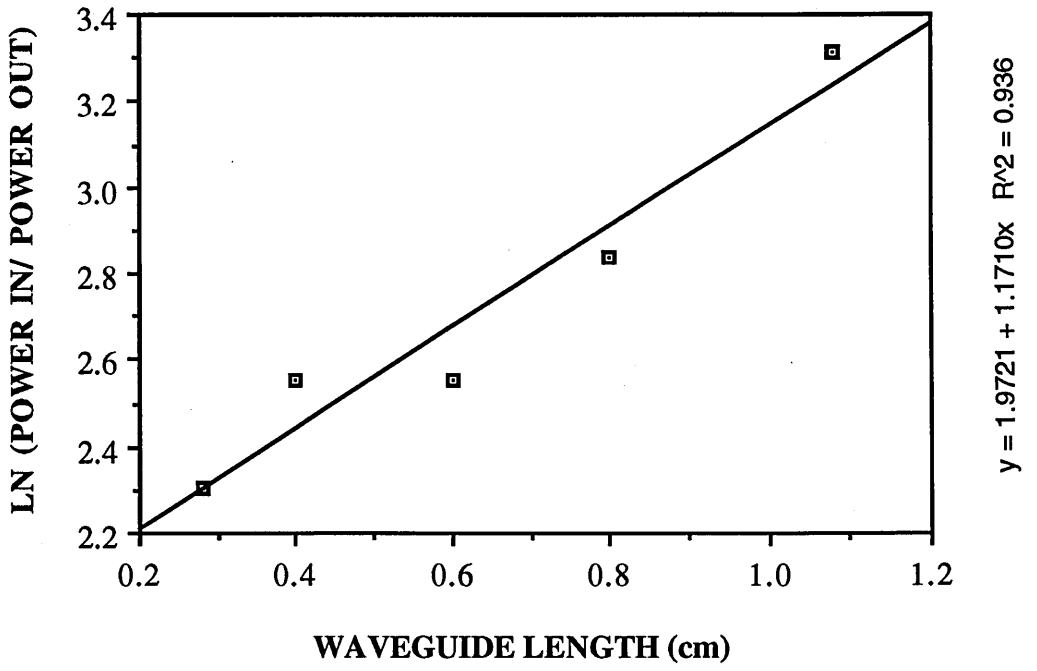

Fig. 4.16 Sequential cleaving plot for TM polarised YAG laser light

It can be seen from the graphs that the absorption coefficient α is about 0.9 cm^{-1} for TE polarised light at 1.06 μm, and 1.2 cm^{-1} for the TM polarisation.

(ii) LOSS MEASUREMENTS- FABRY-PÉROT

The other method used to measure the loss of the waveguides was by Fabry-Pérot transmission measurements. If the waveguide is short enough, it can be considered a Fabry-Pérot interferometer, as pictured in Fig. 4.17.

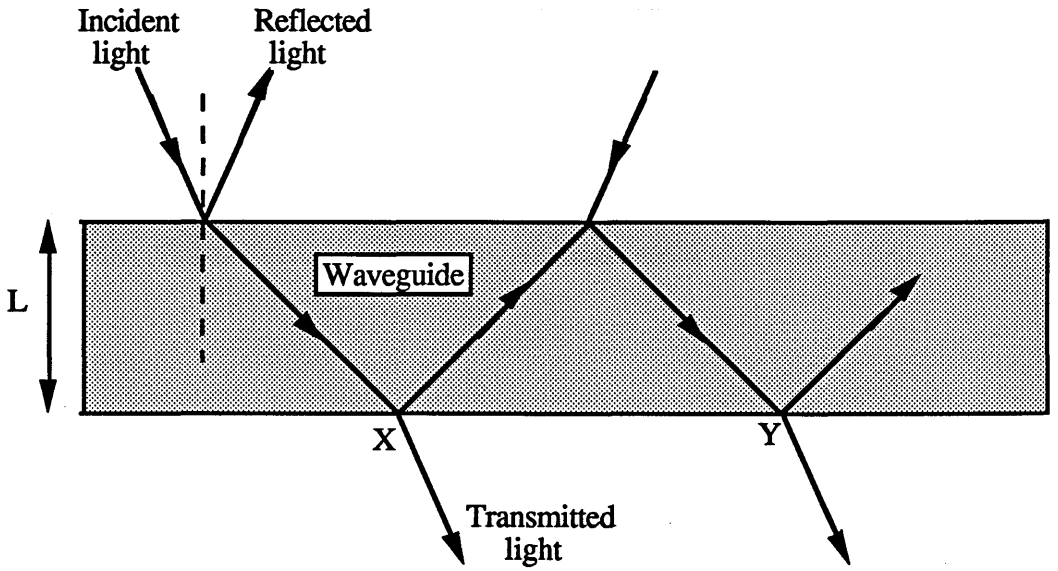

Fig. 4.17 Fabry-Pérot étalon

The fraction of the light which is transmitted is summed for all the multiple reflections and found to be

$$T = \frac{A(1-R)^2}{(1-AR)^2 + 4AR\,\sin^2(\delta/2)} \tag{4.4}$$

where A is the fractional intensity loss per pass of the étalon, i.e. between points X and Y, R is the reflectivity at the interfaces and δ is the phase difference between X and Y *(Yariv 1985)*. From this expression, the resonant and antiresonant transmissions can be found to be

$$T_r = \frac{A(1-R)^2}{(1-AR)^2} \qquad T_{ar} = \frac{A(1-R)^2}{(1+AR)^2} \tag{4.5}$$

The absorption in the waveguide can be found by measuring the ratio of the resonant and antiresonant transmissions. It is given by *(Walker 1985)*

$$\alpha\,(cm^{-1}) = -\frac{1}{L}\ln\left(\frac{1}{R}\left[\frac{\sqrt{k}-1}{\sqrt{k}+1}\right]\right) \tag{4.6}$$

where L is the waveguide length in cm and $k = \frac{T_r}{T_{ar}}$. (4.7)

Any real laser has a finite linewidth, and so, because the phase difference term δ in Eqn. 4.4 is wavelength-dependent, there will be a decrease in the fringe visibility due to the spectral range of the laser. The free spectral range is defined as the separation between the frequencies of the étalon which lead to maximum transmission can be shown to be *(Yariv 1985)*

$$\Delta\nu = \frac{c}{2nL} \tag{4.8}$$

where c is the velocity of light and n is the linear refractive index. In order to make an accurate measurement of the loss, it is therefore necessary to use a laser whose linewidth is narrower than this free spectral range. The waveguides to be measured were 5 mm long, so that the free spectral range was $2x10^{10}$ Hz. As the linewidth of the Nd^{3+}:YAG laser was about 120 GHz, this was not suitable to carry out the measurements, and so a He-Ne laser at 1.15 μm was used, whose linewidth was about 1,500 MHz *(Siegman 1986)*. The absorption coefficient measured at 1.15 μm can be approximated to the absorption coefficient at 1.06 μm. This is because the loss in this wavelength range for the waveguide structure of Fig. 3.4 is mainly due to scattering or leaky modes through to the GaAs substrate, with only a small proportion due to interband absorption.

In order to measure the waveguide loss, a heated soldering iron was placed close to the waveguide. This altered the refractive index, and hence the optical length, of the waveguide. As the waveguide was warmed, the fraction of the light transmitted therefore varied. The output power from the waveguide was measured as it was heated, as shown in Figs. 4.18 and 4.19 for the waveguides used for the experiments of this thesis. A reflection coefficient of 0.32 was assumed. For TE polarised light, k=2.3, so that α=0.9 cm^{-1}, and for TM polarised light, k=2.0, so that α=1.3 cm^{-1}. The uncertainty in these measurements is about 10%. These values are in good agreement with the loss measurements made by sequential cleaving (Section 3.5(i)), from which it was found that for TE polarised light α=0.9 cm^{-1} and for TM polarised light α=1.2 cm^{-1}.

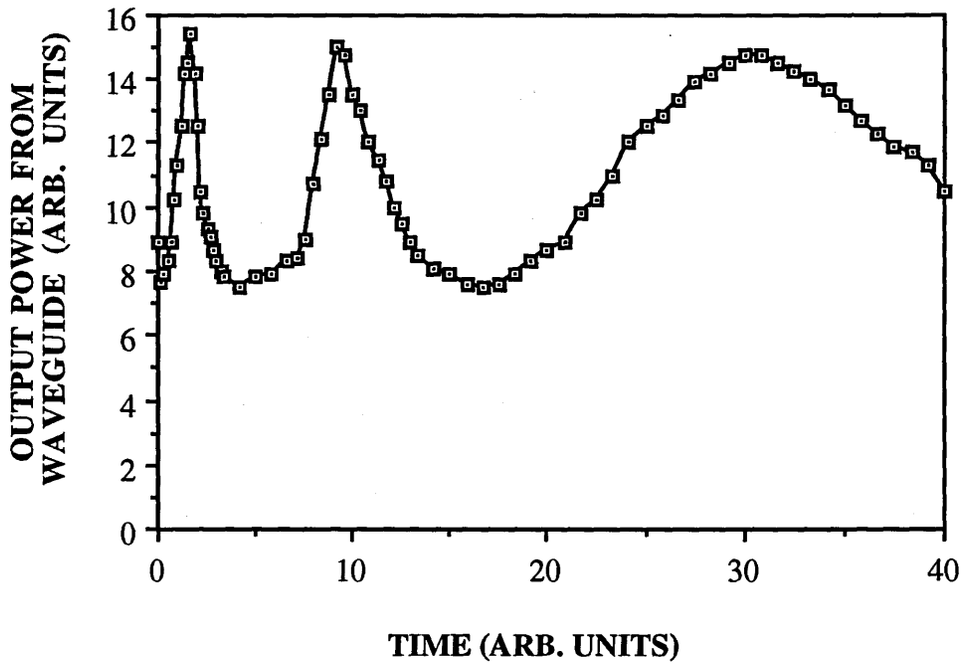

Fig. 4.18 Fabry-Pérot resonances in the GaAs/AlGaAs MQW waveguide with TM polarised light

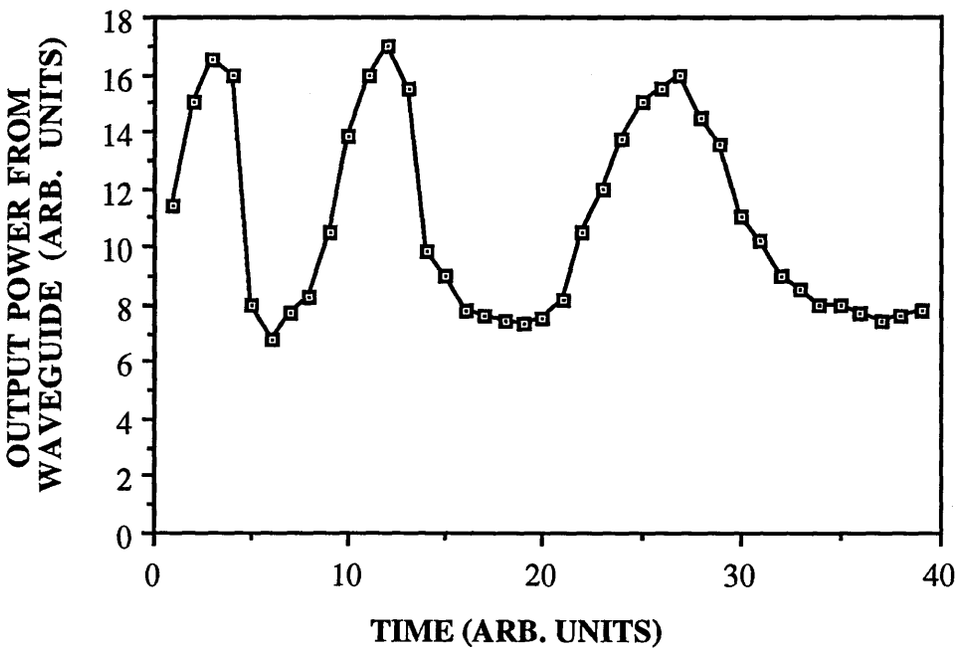

Fig. 4.19 Fabry-Pérot resonances in the GaAs/AlGaAs MQW waveguide with TE polarised light

CHAPTER FIVE
NONLINEAR ABSORPTION THEORETICAL MODEL

In this chapter a theoretical model is derived for nonlinear absorption in waveguides. This includes in an intuitive manner the effects of two-photon absorption and free carrier absorption together with those of linear absorption. The chapter begins by describing the nonlinear absorption of a single modelocked laser beam propagating through a waveguide, and proceeds to the case of pump and probe beams. The equations are then extended so that pump-probe experiments can be modelled for which either the pump intensity or pump-probe delay time varies.

Note that throughout this chapter, the term "intensity" is always taken to mean the peak intensity of a laser pulse, rather than the average intensity. The terms "input intensity" and "output intensity" mean the intensity at either the input or output end of the waveguide, but **inside** the waveguide. This means that the effects of Fresnel reflections and coupling losses into the waveguide mode can be considered separately, and so the form of the equations is simplified.

5.1 EQUATIONS FOR NONLINEAR ABSORPTION FOR A SINGLE MODELOCKED LASER BEAM

5.1.1 LINEAR ABSORPTION:

For a low intensity beam, the rate of change of intensity with distance as it propagates through a sample is assumed to be proportional to the instantaneous intensity, that is

$$\frac{dI}{dz} = -\alpha I \tag{5.1}$$

which has a solution of the form

$$I(z) = I(0)\, e^{-\alpha z} \tag{5.2}$$

where I(0) is the input intensity and I(z) is the intensity at a distance z.

5.1.2 INCLUDING TWO-PHOTON ABSORPTION:

When a high intensity beam, whose photon energy is smaller than the energy gap E_g but greater than $E_g/2$, propagates through a waveguide, two-photon absorption (TPA) can become a significant fraction of the total absorption (see Section 2.5.1 for the theory of TPA). The rate of change of intensity with distance is now given by

$$\frac{dI}{dz} = -\alpha I - \beta I^2 \tag{5.3}$$

with a solution

$$I(z) = \frac{I(0)\ \alpha\ e^{-\alpha z}}{\alpha + \beta I(0)\ (1 - e^{-\alpha z})} \tag{5.4}$$

This can be usefully rearranged to give

$$\frac{1}{I(z)} = \frac{1}{e^{-\alpha z} I(0)} + \frac{\beta(1 - e^{-\alpha z})}{\alpha e^{-\alpha z}} \tag{5.5}$$

which is the equation for a straight line. This equation shows that if the reciprocal of the input intensity is plotted against the reciprocal of the output intensity, the TPA coefficient β can be found from the intercept of this line. The linear absorption coefficient α can also be found from the line's gradient.

5.1.3 INCLUDING FREE CARRIER ABSORPTION:

If the effect of free carrier absorption (FCA) is now included in the equations for linear absorption and TPA, then the rate of change of intensity with distance is given by *(Van Stryland 1985)*

$$\frac{dI}{dz} = -\alpha I - \beta I^2 - \sigma_{ex} N I \tag{5.6}$$

where N is the density of free carriers (both electrons and holes), and σ_{ex} is the total carrier cross section.

If we assume that the photon energy is much smaller than the energy gap E_g but greater than $E_g/2$ (as will be the case for a high intensity Nd^{3+}:YAG laser beam at 1.06 μm in a GaAs/AlGaAs MQW waveguide), then any free carriers will be generated predominantly by TPA. Their rate of generation is given by *(Van Stryland 1985)*

$$\frac{dN}{dt} = \frac{\beta I^2}{2h\nu} \tag{5.7}$$

This equation assumes that the laser pulsewidth is much shorter than the carrier recombination time. This assumption is valid for the semiconductor material used for the experiments presented in this thesis, as the carrier lifetime in the wafer used in the experiments of this thesis was measured by G.S. Buller of the Department of Physics, Heriot-Watt University by time-resolved photoluminescence to be about 35 ns. This is much longer than the laser pulsewidth of about 100 ps. It is also assumed that carrier diffusion times are much longer than the pulsewidth, and electron-hole pair generation by means of photoionization of an electron from the valence band to the conduction band via intermediate energy levels inside the forbidden energy gap, such as the $EL2^+$ level *(Valley et al. 1989)* is neglected.

If the laser pulse is Gaussian in time, then it can be written as

$$I(t) = I_0 \exp\left(\frac{-2t^2}{T^2}\right) \tag{5.8}$$

so that the density of carriers created by a single pulse is given by

$$N_p = \frac{\beta}{2h\nu}\int_{-\infty}^{\infty} I_0^2 \exp\left(\frac{-4t^2}{T^2}\right) dt \tag{5.9}$$

This can be solved by comparing to the standard integral

$$\int_0^{\infty} \exp\left(-a^2x^2\right) dx = \frac{\sqrt{\pi}}{2a} \tag{5.10}$$

and so the density of carriers created per pulse is found to be

$$N_p = \frac{\beta\sqrt{\pi}\, T I_0^2}{4\, h\nu} \tag{5.11}$$

If the carrier lifetime is comparable to or longer than the laser pulse separation, then at any instant in time there will be some carriers present in the waveguide which were created by previous laser pulses. This means that the free carrier absorption experienced by any pulse propagating through the waveguide will be due not only to the carrier density which it creates itself, but also to the remnants of the carriers created by previous pulses. If the time between the modelocked pulses of the laser beam is t_p and

the carrier lifetime in the waveguide is τ, then the total carrier density seen by a pulse is given by

$$N = N_p\left[1 + \exp\left(\frac{-t_p}{\tau}\right) + \exp\left(\frac{-2t_p}{\tau}\right) + \exp\left(\frac{-3t_p}{\tau}\right) + ...\right] \tag{5.12}$$

which can be simplified, as the sum of a geometric series, to

$$N = N_p\left(\frac{1}{\left[1-\exp\left(\frac{-t_p}{\tau}\right)\right]}\right) = F N_p \tag{5.13}$$

Eqn. 5.11 can now be substituted into Eqn. 5.13 to give an expression for the carrier density seen by each of the modelocked pulses:

$$N = \frac{F\beta\sqrt{\pi}\, T I_0^2}{4h\nu} \tag{5.14}$$

An intensity-independent FCA coefficient can then be defined as

$$\gamma = \frac{\sigma_{ex} N}{I^2} = \frac{\sigma_{ex} F\beta\sqrt{\pi}\, T}{4h\nu} \tag{5.15}$$

and this can now be substituted into Eqn. 5.6 to give

$$\frac{dI}{dz} = -\alpha I - \beta I^2 - \gamma I^3 \tag{5.16}$$

This can be integrated analytically by using standard integrals (*CRC Handbook*)

$$\int \frac{dI}{\alpha I + \beta I^2 + \gamma I^3} = \frac{1}{2\alpha}\log\left(\frac{I^2}{\alpha + \beta I + \gamma I^2}\right) - \frac{\beta}{2\alpha}\int \frac{dI}{\alpha + \beta I + \gamma I^2} \tag{5.17}$$

Define $q=4\alpha\gamma-\beta^2$.

If $q<0$, then

$$\int \frac{dI}{\alpha + \beta I + \gamma I^2} = \frac{1}{\sqrt{-q}}\log\left(\frac{2\gamma I + \beta - \sqrt{-q}}{2\gamma I + \beta + \sqrt{-q}}\right) \tag{5.18}$$

If $q>0$, then

$$\int \frac{dI}{\alpha + \beta I + \gamma I^2} = \frac{2}{\sqrt{q}}\tan^{-1}\left(\frac{2\gamma I + \beta}{\sqrt{q}}\right) \tag{5.19}$$

So the equation relating the output intensity from a waveguide to the input intensity can now be solved for linear absorption, TPA and FCA simultaneously:

$$\int_{I(0)}^{I(L)} \frac{dI}{\alpha I + \beta I^2 + \gamma I^3} = -L \qquad (5.20)$$

If $q<0$, that is if $\beta^2 > 4\alpha\gamma$, then

$$\left[\log\left(\frac{I^2}{\alpha + \beta I + \gamma I^2}\right)\right]_{I(0)}^{I(L)} = \left[\frac{\beta}{\sqrt{-q}} \log\left(\frac{2\gamma I + \beta - \sqrt{-q}}{2\gamma I + \beta + \sqrt{-q}}\right)\right]_{I(0)}^{I(L)} - 2\alpha L \qquad (5.21)$$

If $q>0$, that is if $\beta^2 < 4\alpha\gamma$, then

$$\left[\log\left(\frac{I^2}{\alpha + \beta I + \gamma I^2}\right)\right]_{I(0)}^{I(L)} = \left[\frac{2\beta}{\sqrt{q}} \tan^{-1}\left(\frac{2\gamma I + \beta}{\sqrt{q}}\right)\right]_{I(0)}^{I(L)} - 2\alpha L \qquad (5.22)$$

It is not possible to solve Eqns. 5.21 or 5.22 analytically, but they can easily be solved numerically. For each value of the peak input intensity I(0), an initial value for the peak output intensity I(L) was guessed. The two sides of the relevant equation were then evaluated, and the value for I(L) adjusted until the difference between them was minimised.

5.1.4. GRAPHICAL REPRESENTATION

Sections 5.1.1-5.1.3 have described the methods for solving the equations for the nonlinear absorption of a single beam, and Fig. 5.1 shows the results of such calculations. Fig. 5.1(a) shows three plots overlaid. The first plot is for linear absorption only (Eqn. 5.2), the second is for linear absorption and TPA combined (Eqn. 5.4), and the third is for linear absorption, TPA and FCA all combined (Eqns. 5.21 or 5.22, depending on the sign of q). Fig. 5.1(b) shows the second and third curves on an expanded scale.

The values inserted into the equations to obtain these plots were $\alpha=100\ m^{-1}$, $\beta=2\times10^{-10}\ m\ W^{-1}$, $\sigma_{ex}=5\times10^{-22}\ m^2$ (*Van Stryland 1985*), L=0.01 m, T=75 ps, τ=30 ns and $h\nu$=1.167 eV. By substituting these into Eqn. 5.11 it was found that $N_p=(0.036I_0^2)\ m^{-3}$. It was then found from Eqn. 5.13 that the carrier density seen by

each of the modelocked pulses was $N=2.84N_p=(0.102I_0^2)$ m^{-3}, and hence, from Eqn. 5.15, that $\gamma=5.12x10^{-23}$ m^3W^{-2}. These values led to a negative value for q, so that Eqn. 5.21 was used to obtain the plot for linear absorption, TPA and FCA all combined.

It can be seen from Fig. 5.1 that the inclusion of the effect of TPA decreases the output intensity significantly for anything more than moderate peak input intensities. The effect of free carriers is less pronounced, and only becomes noticeable at high peak input intensities.

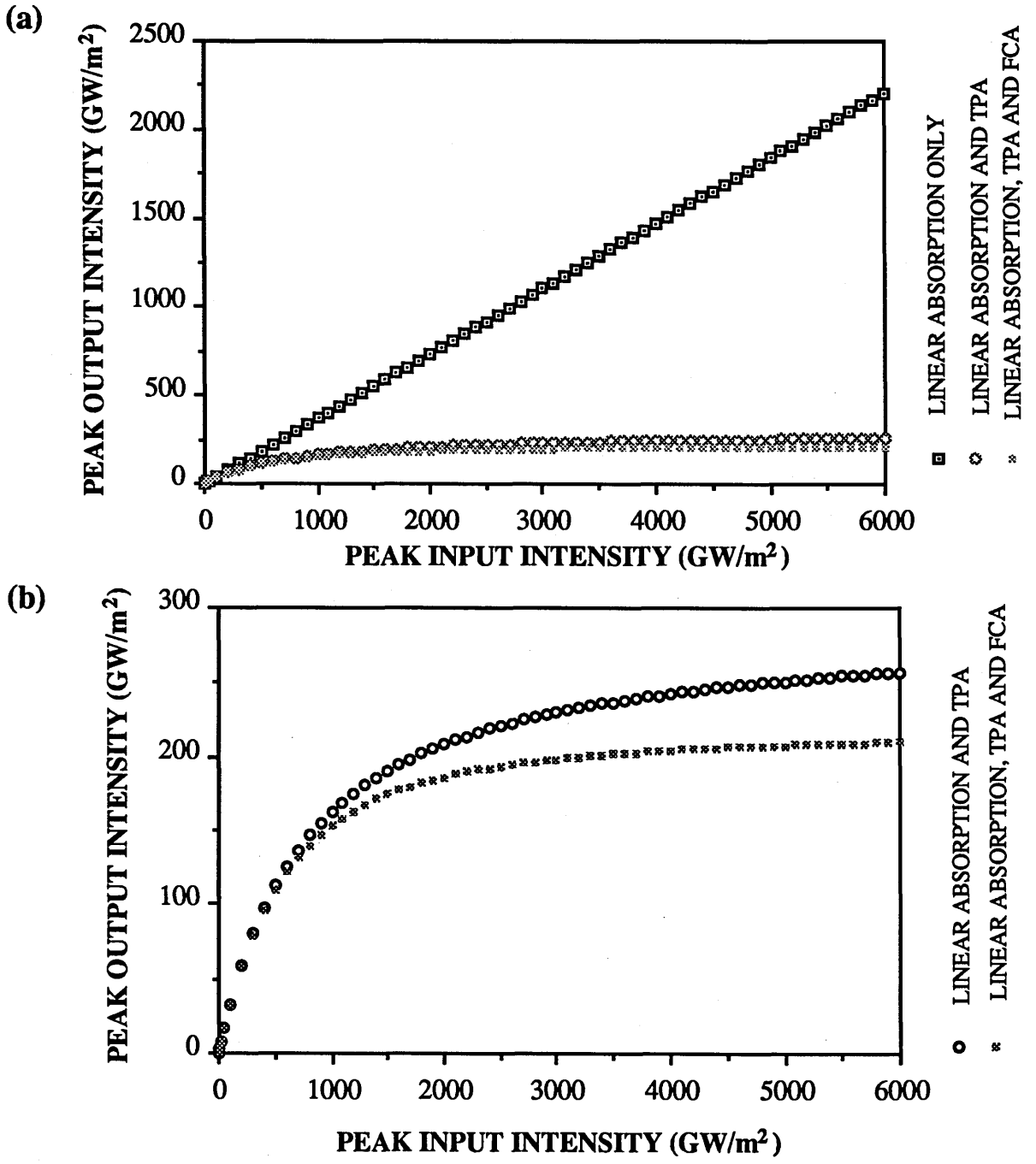

Figure 5.1 Output against input intensity for linear absorption, TPA and FCA

5.2 EQUATIONS FOR NONLINEAR ABSORPTION FOR A PUMP AND A PROBE BEAM IN THE WAVEGUIDE

5.2.1. TWO-PHOTON ABSORPTION FOR TWO LASER PULSES

Referring back to Eqn. 5.3, we have seen that the rate of change of intensity with distance of a single beam under the influence of linear and two-photon absorption is given by

$$\frac{dI}{dz} = -\alpha I - \beta I^2 \tag{5.23}$$

In this case, both of the photons which contributed to the TPA process came from the same beam. However, as already discussed in Section 2.5.1, TPA can also take place such that the two photons involved in the absorption come from two different beams, which can be of different frequencies or polarisations. Consider now the case of two Gaussian beams present in the waveguide, where one is a pump pulse of high peak intensity and the other is a probe pulse of much lower intensity. Then the rate of change of intensity of the probe beam is given by

$$\frac{dI_{probe}}{dz} = -\alpha I_{probe} - \beta I_{probe}^2 - \beta I_{probe} I_{pump} \tag{5.24}$$

In this equation, the second term on the right hand side represents the TPA of two photons from the probe beam, and the third term represents the TPA of one photon from each of the probe and pump beams.

Let the probe intensity be represented by the following equations

$$I_{probe} = I'_{probe} \exp\left(\frac{-2t^2}{T^2}\right) \tag{5.25}$$

and the pump intensity by

$$I_{pump} = I'_{pump} \exp\left(\frac{-2(t-t_d)^2}{T^2}\right) \tag{5.26}$$

where I'_{pump} and I'_{probe} are the peak intensities of the pump and probe beams respectively, and the full pulsewidth at 1/e of the maximum intensity is given by $\sqrt{2}\,T$.

We can assume that the term I_{probe} in Eqn. 5.24 represents the peak intensity of the probe beam, that is I'_{probe}, just as we did for the case of a single beam. If the time delay between the pump and probe pulses, t_d, is zero, then the term I_{pump} in Eqn. 5.24 represents the peak intensity of the pump beam, that is I'_{pump}. As t_d becomes greater, the absorption of the probe pulse becomes less strongly dependent on the pump intensity, and so the term I_{pump} should be represented by a function which decays in an appropriate manner with respect to t_d. Appendix 1 describes the working used to show that the term I_{pump} in Eqn. 5.24 should be written as

$$I_{pump} = I'_{pump} \exp\left(\frac{-t_d^2}{T^2}\right) \tag{5.27}$$

So Eqn. 5.24 can now be rewritten as

$$\frac{dI'_{probe}}{dz} = -\alpha I'_{probe} - \beta I'^{2}_{probe} - \beta I'_{probe} I'_{pump} \exp\left(\frac{-t_d^2}{T^2}\right) \tag{5.28}$$

This equation shows that if the peak pump intensity is increased, the effect of TPA on the probe beam also increases, and so the higher the pump intensity, the higher the absorption of the probe beam. Similarly, it can be seen that the smaller the time delay between the two beams, the higher the absorption of the probe.

Eqn. 5.28 could now be integrated in order to find the output probe intensity as a function of either pump intensity or time delay t_d between the two beams, but first we will include the effect of FCA in the working.

5.2.2. FREE CARRIER ABSORPTION FOR TWO LASER PULSES

The FCA coefficient, γ, is proportional to the number of carriers present in the waveguide at any instant (Eqn. 5.15). We now assume that the probe is sufficiently less intense than the pump that the number of carriers it generates itself are negligible, and that it is only affected by the carriers created by the pump pulse. When the probe beam passes through the waveguide, it will be absorbed more strongly if there are more free carriers present.

If the pulses are exactly coincident, the probe pulse will see all of the carriers created by the pump pulse and it will also see any carriers still remaining from previous pump pulses, just as for the case of a single beam. Equations 5.13 and 5.14 can

therefore be used for this case in order to find the carrier density seen by the probe beam, with I_0 in Eqn. 5.14 being made equal to the peak pump intensity.

If the probe is incident on the sample a time t_d after the pump, then the probe pulse will see all the carriers created by the pump pulse except for those which have recombined in the time interval t_d. For a probe pulse incident on the sample a time t_d before the pump, the probe will see only that fraction of the carriers created by the pump during the overlap of pump and probe. This fraction is of a Gaussian form, and depends on τ, the carrier lifetime, and T, which is proportional to the pulsewidth. In both these cases, the probe pulse will additionally see any carriers created by previous pump pulses which have not yet recombined.

So, if the probe is incident on the sample a time t_d after the pump, the pump pulses are separated by a time t_p and the carrier lifetime is τ, then the number of carriers created by the pump that the probe will experience will be given by

$$N = N_p\left[\exp\left(\frac{-t_d}{\tau}\right) + \exp\left(\frac{-[t_p + t_d]}{\tau}\right) + \exp\left(\frac{-[2t_p + t_d]}{\tau}\right) + ..\right] \tag{5.29}$$

which can be simplified, as the sum of a geometric progression, to

$$N = N_p\left(\frac{\exp\left(\frac{-t_d}{\tau}\right)}{\left[1 - \exp\left(\frac{-t_p}{\tau}\right)\right]}\right) = F N_p \tag{5.30}$$

If the probe is incident on the sample a time t_d before the pump, then the number of carriers that the probe will experience in this case will be

$$N = N_p\left[\exp\left(\frac{-t_d^2}{T^2}\right) + \exp\left(\frac{-[t_p + t_d]}{\tau}\right) + \exp\left(\frac{-[2t_p + t_d]}{\tau}\right) + ...\right] \tag{5.31}$$

and this can be similarly simplified to

$$N = N_p\left(\exp\left[\frac{-t_d^2}{T^2}\right] + \frac{\exp\left[\frac{-(t_p - t_d)}{\tau}\right]}{\left(1 - \exp\left[\frac{-t_p}{\tau}\right]\right)}\right) = F N_p \tag{5.32}$$

Define $N = FN_p$, and Fig 5.2 is then a plot of F against t_d for t_p=13 ns, T=75 ps and τ=10, 20,30 and 40 ns.

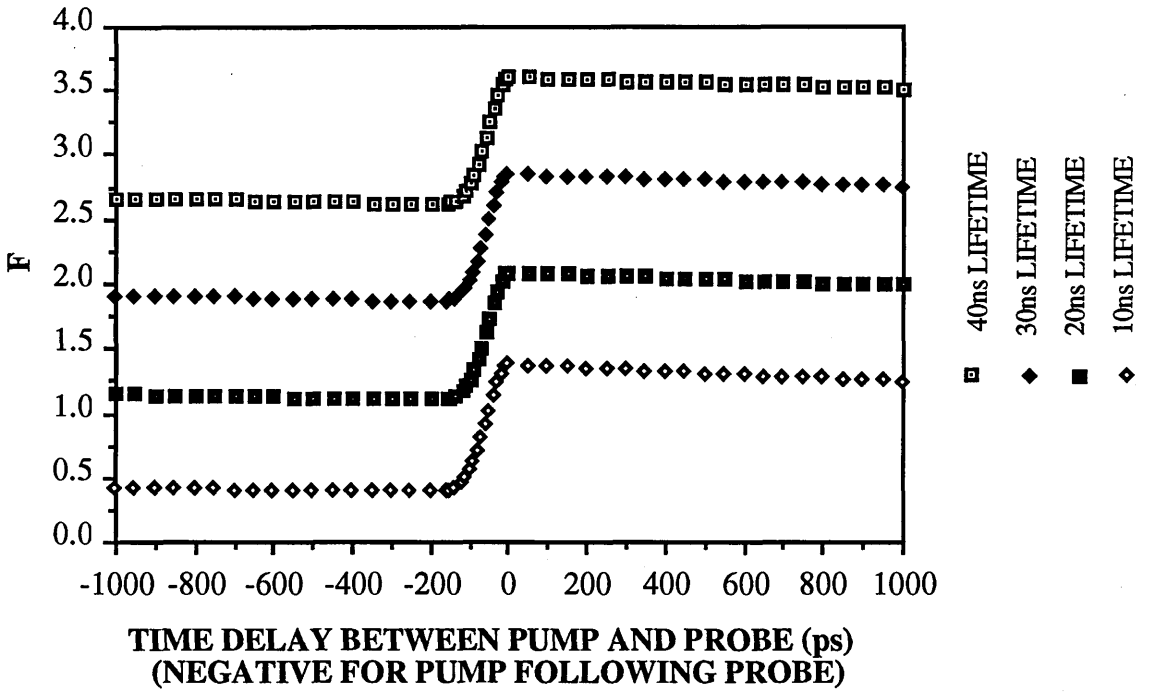

Figure 5.2 Plot of the carrier density seen by the probe pulse due to a pump pulse separated in time from the probe.

Eqn 5.28 has shown the rate of change of intensity with distance of a probe beam in the presence of a pump beam under the influence of linear and two-photon absorption to be

$$\frac{dI'_{probe}}{dz} = -\alpha I'_{probe} - \beta I'^{2}_{probe} - \beta I'_{probe} I'_{pump} \exp\left(\frac{-t_d^2}{T^2}\right) \tag{5.33}$$

We can now add the term relating to FCA to this equation to give

$$\frac{dI'_{probe}}{dz} = -\alpha I'_{probe} - \beta I'^{2}_{probe} - \beta I'_{probe} I'_{pump} \exp\left(\frac{-t_d^2}{T^2}\right) - \sigma_{ex} N I'_{probe} \tag{5.34}$$

where N is the carrier density seen by the probe beam. Let us assume that the pump is much more intense than the probe, so that any free carriers present in the waveguide are created by two-photon absorption of the pump beam alone. Then the carrier density seen by the probe beam is given by

$$N = F_1 N_p = \frac{F_1 \beta \sqrt{\pi}\, T I'^{2}_{pump}}{4h\nu} \tag{5.35}$$

Here F_1 is the proportionality factor relating the carrier density created per single pump pulse to that created by the series of pump pulses, as seen by the probe pulses separated by a time t_d from the pump pulses. This can be calculated using Eqns. 5.30 or 5.32, depending on whether the pump pulses precede or follow the probe pulses.

Eqn. 5.34 can therefore be rewritten as

$$\frac{dI'_{probe}}{dz} = -\alpha I'_{probe} - \beta I'^{2}_{probe} - \beta I'_{probe} I'_{pump} \exp\left(\frac{-t_d^2}{T^2}\right) - \gamma_1 I'^{2}_{pump} I'_{probe} \qquad (5.36)$$

$$\text{where } \gamma_1 = \frac{\sigma_{ex} F_1 \beta \sqrt{\pi}\, T}{4 h\nu} \qquad (5.37)$$

Eqn. 5.36 can now be integrated in order to find the output probe intensity from a waveguide under the influence of linear, two-photon and free carrier absorption as a function of pump intensity or pump-probe delay time.

5.3 INTEGRATION OF THE PUMP-PROBE NONLINEAR ABSORPTION EQUATIONS OVER THE WAVEGUIDE

In order to determine the nonlinear absorption in a waveguide, taking into account simultaneously the effects of TPA and FCA, it is necessary to integrate the equations of the previous sections over the length of the waveguide. In this section, equations will be derived to describe the nonlinear absorption of a weak probe pulse due to the presence of a strong pump pulse. Eqn. 5.36 can be rearranged to give

$$\frac{dI'_{probe}(z)}{dz} + \left[\alpha + \beta I'_{pump}(z) \exp\left(\frac{-t_d^2}{T^2}\right) + \gamma_1 I'^{2}_{pump}(z)\right] I'_{probe}(z) = -\beta I'^{2}_{probe}(z) \qquad (5.38)$$

$$\text{Let } I'_{probe}(z) = v \exp\left[-\int \left[\alpha + \beta I'_{pump}(z) \exp\left(\frac{-t_d^2}{T^2}\right) + \gamma_1 I'^{2}_{pump}(z)\right] dz\right] \qquad (5.39)$$

and now substitute this into Eqn. 5.38 to give

$$\int_{z=0}^{z=L} \frac{dv}{v^2} = -\beta \int_{z=0}^{z=L} \exp\left[- \int \left(\alpha + \beta\, I'_{pump}(z) \exp\left(\frac{-t_d^2}{T^2}\right) + \gamma_1\, I'^{2}_{pump}(z) \right) dz \right] dz \tag{5.40}$$

where L is the length of the waveguide. The next stage is to solve the integral

$$Int = \int \left(\alpha + \beta\, I'_{pump}(z) \exp\left(\frac{-t_d^2}{T^2}\right) + \gamma_1\, I'^{2}_{pump}(z) \right) dz \tag{5.41}$$

In order to solve this integral, some assumptions are made about the rate of change of intensity of the pump beam as it propagates through the waveguide. Because the pump beam is much more intense than the probe beam, it is assumed that its rate of decay as it passes through the waveguide is unaffected by the presence of the probe beam. So the rate of change of intensity of the pump beam may be found from Eqn. 5.16, by considering it to be a single beam in the waveguide:

$$\frac{dI'_{pump}(z)}{dz} = -\alpha I'_{pump}(z) - \beta I'^{2}_{pump}(z) - \gamma_2 I'^{3}_{pump}(z) \tag{5.42}$$

$$\text{where } \gamma_2 = \frac{\sigma_{ex} F_2 \beta \sqrt{\pi}\, T}{4 h\nu} \tag{5.43}$$

Here, F_2 is the proportionality factor relating the carrier density created per single pump laser pulse to the carrier density created by the series of pump pulses, as seen by the pump pulses themselves. F_2 can therefore be found from Eqn. 5.13. (If $t_d \neq 0$, then the number of carriers created by TPA of the pump beam that are seen by the pump beam will be different to the number seen by the probe beam. This means that $F_1 \neq F_2$, and so $\gamma_1 \neq \gamma_2$).

Eqn 5.42 is soluble by means of Eqns. 5.21 or 5.22, as shown in Section 5.1.3, so that $I'_{pump}(z)$ and $I'^{2}_{pump}(z)$ could then be substituted into Eqn. 5.40, and this could then be solved. However, as it is not possible to solve Eqn. 5.42 analytically, this process can be considerably simplified by assuming that the pump intensity decays through the waveguide as a result of linear absorption and TPA only, and neglecting the effect of FCA. Then Eqn. 5.42 can be simplified to

$$\frac{dI'_{pump}(z)}{dz} = -\alpha I'_{pump}(z) - \beta I'^{2}_{pump}(z) \tag{5.44}$$

which can be solved analytically, as in Eqn. 5.4, to give

$$I'_{pump}(z) = \frac{I'_{pump}(0)\ \alpha\ e^{-\alpha z}}{\alpha + \beta I'_{pump}(0)\ (1 - e^{-\alpha z})} \tag{5.45}$$

With these assumptions, we can therefore obtain an analytical solution to the integral of Eqn. 5.41, the working for which is contained in Appendix 2. From Eqn. A2.10,

$$Int = \alpha z - \frac{\gamma_1 I'_{pump}(z)}{\beta} - \left(\frac{\gamma_1 \alpha}{\beta^2} - \exp\left[\frac{-t_d^2}{T^2}\right] \right) \ln\left[\alpha + \beta I'_{pump}(0) \left(1 - e^{-\alpha z} \right) \right] \tag{5.46}$$

Substitution of Eqn. 5.46 into Eqn. 5.40 gives the equation

$$\int_{z=0}^{z=L} \frac{dv}{v^2} = -\beta \int_0^L \exp\left[\left(\frac{\gamma_1 \alpha}{\beta^2} - \exp\left[\frac{-t_d^2}{T^2}\right] \right) \ln\left[\alpha + \beta I_{pump}(0)(1 - e^{-\alpha z})\right] + \frac{\gamma_1\ \alpha\ I_{pump}(0)\ e^{-\alpha z}}{\beta\left(\alpha + \beta I_{pump}(0)(1 - e^{-\alpha z})\right)} - \alpha z \right] dz \tag{5.47}$$

where v is related to $I_{probe}(z)$ by the equation

$$I'_{probe}(z) = v \exp\left[\left(\frac{\gamma_1 \alpha}{\beta^2} - \exp\left[\frac{-t_d^2}{T^2}\right] \right) \ln\left[\alpha + \beta I'_{pump}(0)\ (1 - e^{-\alpha z})\right] + \frac{\gamma_1 \alpha I'_{pump}(0)\ e^{-\alpha z}}{\beta\left(\alpha + \beta I'_{pump}(0)(1 - e^{-\alpha z})\right)} - \alpha z \right] \tag{5.48}$$

Eqns 5.47 and 5.48 can then be integrated numerically using Simpson's Rule, so that if the input pump intensity $I_{pump}(0)$ and the input probe intensity $I_{probe}(0)$ are known, then the output probe intensity $I_{probe}(L)$ can be calculated.

5.4 SUMMARY OF CHAPTER FIVE

This chapter has derived a theoretical model for nonlinear absorption in waveguides, which includes the effects of two-photon absorption and free carrier absorption together with those of linear absorption. The equations for nonlinear absorption have been solved for both a single beam and for pump and probe beams, and these equations will be used in the following chapter to model pump-probe nonlinear absorption experiments.

CHAPTER SIX
NONLINEAR ABSORPTION EXPERIMENTS AND FITTING TO THE THEORETICAL MODEL

This chapter describes nonlinear absorption experiments carried out in GaAs/AlGaAs MQW waveguides using a Nd^{3+}:YAG laser at 1.06 μm. The first section is concerned with single-beam experiments, in which the output intensity of the modelocked beam was measured as a function of the input intensity. From these experiments, the two-photon absorption coefficient β was initially calculated by the usual method, which is to neglect free carrier absorption (FCA). It was then recalculated using the theoretical model of Chapter 5, which includes the effect of FCA. The pump-probe experiments are then described, and graphs presented for the probe transmission as a function of both the pump intensity and the pump-probe delay time. These are also fitted to the model of the previous chapter.

6.1 SINGLE BEAM NONLINEAR ABSORPTION MEASUREMENTS

There are several experimental methods by which the TPA coefficient β has been calculated, including Fabry-Pérot loss measurements *(Aitchison 1990)* and photocurrent measurements *(White 1990)* for various peak input intensities. The most usual method is to measure the nonlinear transmission of a sample for various input intensities, and to calculate β from Eqn. 5.5 *(Bechtel 1976, Van Stryland 1985, Villeneuve 1990, Mizrahi 1989 and Le 1990)*. The first four of these references used a single beam for their experiments and neglected the effect of FCA, while Le used a picosecond pump-probe nonlinear transmission measurement in order to resolve the instantaneous TPA from the longer-lived FCA.

This section describes single-beam nonlinear transmission experiments carried out to measure β in a rib waveguide while taking into account the effect of FCA, using the theoretical model of Section 6.1. The method used has the advantages of giving a more accurate estimate of β than when FCA is neglected, while being simpler both experimentally and in analysis than that of Le.

6.1.1 EXPERIMENTAL ARRANGEMENT

The experiment was set up as shown in Fig. 6.1 for TM polarised light. For TE polarised light, the waveguide was inserted into the path of the light passing through the polarising beamsplitter cube. The waveguide used was patterned as previously described in Section 3.4, etched so that the rib height was 0.8 μm, and then cleaved to a length of 10 mm. The YAG laser was modelocked, and the quality of modelocking was continually monitored using the KTP crystal (see Section 4.1.2). Several individual ribs of different widths were investigated on the same sample. The output objective lens was focussed carefully so that the plane of focus of the guided beam was coincident with the iris, so as to minimise diffraction effects.

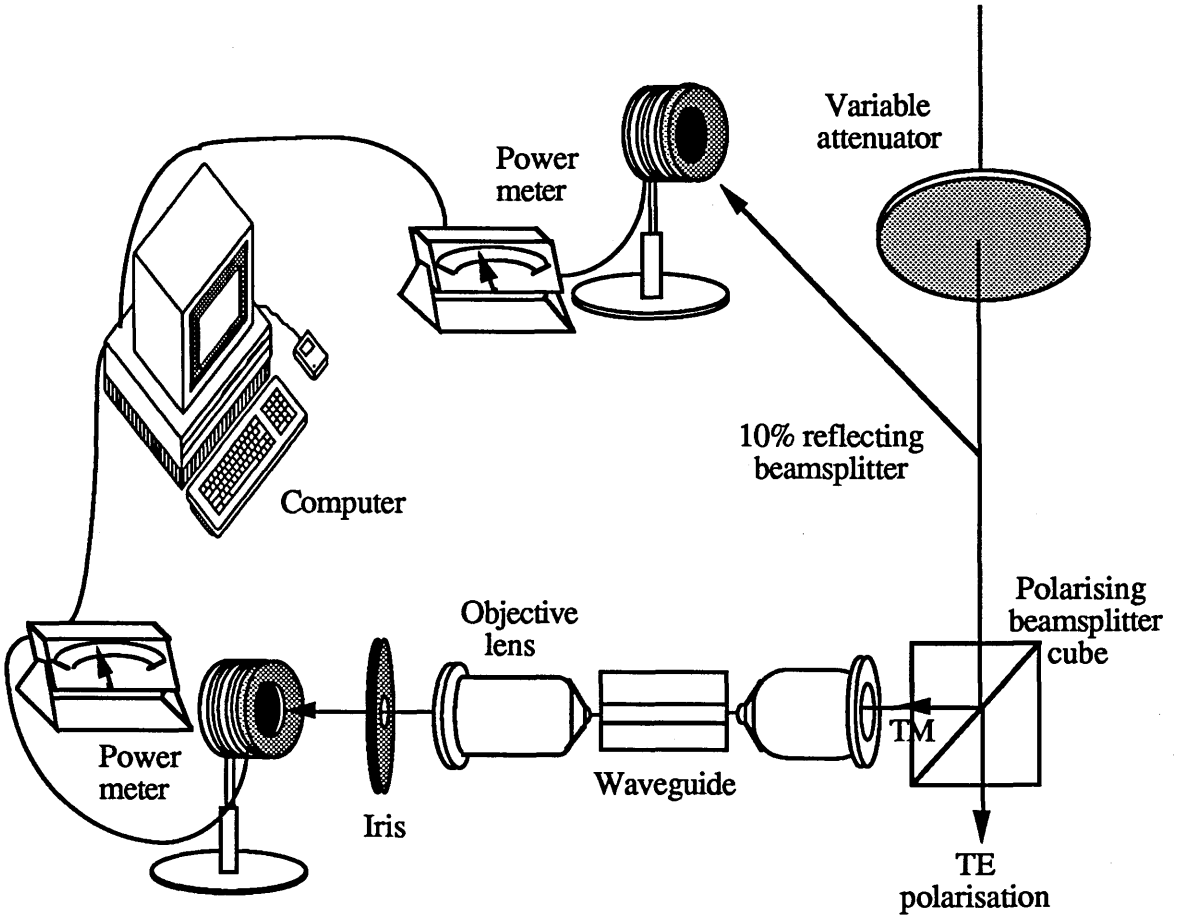

Figure 6.1 Single beam nonlinear absorption experiment with TM polarised light

In order to estimate the input intensity, the average input power was measured by the power meter as shown in Fig. 6.1. If the separation between the pump pulses is t_p and the peak power is P_0, then the average power is given by

$$P_{ave} = \frac{\int_{-\infty}^{\infty} P dt}{\int_0^{t_p} dt} \tag{6.1}$$

$$P_{ave} = \frac{\int_{-\infty}^{\infty} \left(P_0 \exp\left(\frac{-2t^2}{T^2} \right) \right) dt}{\int_0^{t_p} dt} \tag{6.2}$$

The ratio of the peak to the average power can thus be found to be

$$\frac{\text{Peak Power}}{\text{Average Power}} = \frac{\sqrt{2}\, t_p}{\sqrt{\pi}\, T} \tag{6.3}$$

For the YAG laser, T=75 ps and t_p=13 ns, so that the power meter readings of average power were multiplied by 138 in order to convert them to peak power. The mode area was calculated from FWave, a Vector Finite Difference computer program (see Section 3.2.2), and hence the peak intensity immediately before the end-fire rig input objective was obtained. This objective transmitted approximately 95% and there was a Fresnel reflection loss of about 30% from the input face of the waveguide. The coupling coefficient of the light into the waveguide mode cannot be measured directly, but was estimated to be about 45%. The peak input intensity inside the waveguide could therefore be estimated, and the peak output intensity inside the waveguide was found in an analogous way.

It should be noted that the value obtained for β will be independent of the estimated value used for the coupling coefficient. This can be seen if Eqn. 5.5 is considered. This equation is repeated below.

$$\frac{1}{I(z)} = \frac{1}{e^{-\alpha z} I(0)} + \frac{\beta(1 - e^{-\alpha z})}{\alpha e^{-\alpha z}} \tag{6.4}$$

In order to estimate β, a graph is plotted of the reciprocal of the peak input intensity against the reciprocal of the peak output intensity, and β is found from the intercept of the straight line by the following equation

$$\text{Intercept} = \left[\frac{1}{I(L)} \right]_{I(0) \to \infty} = \frac{\beta(1 - e^{-\alpha z})}{\alpha e^{-\alpha z}} \tag{6.5}$$

It can therefore be seen that the value obtained for β does not depend on the estimated value for the coupling coefficient of the input beam into the guided mode.

6.1.2 EXPERIMENTAL RESULTS

Figs. 6.2 and 6.3 show examples of the resulting plots of output against input intensity for TM and TE polarised light respectively.

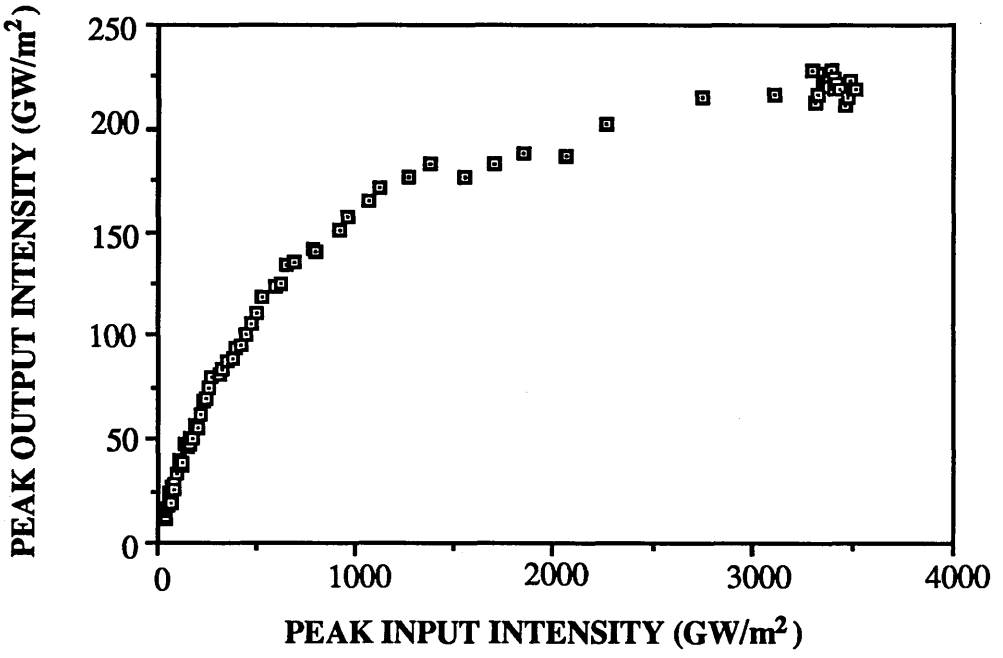

Figure 6.2 Relationship between the input and output peak intensity for a modelocked YAG beam of TM polarisation in a GaAs/AlGaAs MQW waveguide

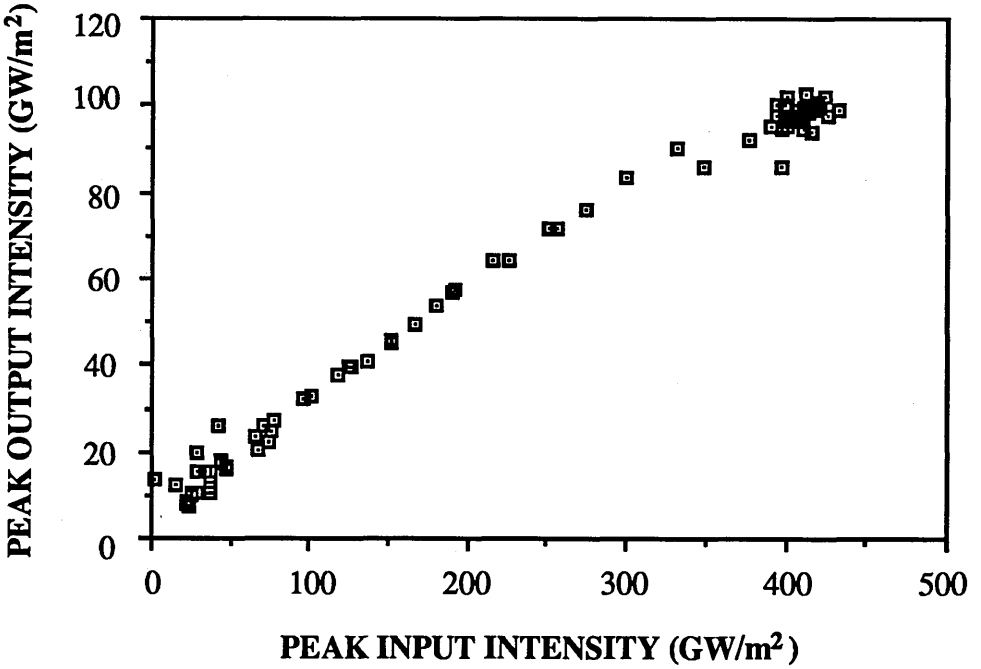

Figure 6.3 Relationship between the input and output peak intensity for a modelocked YAG beam of TE polarisation in a GaAs/AlGaAs MQW waveguide

The relationship between peak input and output intensity in Fig. 6.2 is clearly very nonlinear, and by comparing with Fig. 5.1, it appears that TPA, and possibly some FCA explain the results. Fig. 6.3 also shows a nonlinear plot, although the nonlinearity is not as obviously apparent as in Fig. 6.2, because the values of the peak input intensity are considerably smaller. This difference in intensity between the two plots is because the polarisation obtained from the YAG laser was vertical, which corresponded to TM for the waveguide. A quarter-wave plate and polarising beam-splitter cube were used to rotate the laser's polarisation to TE, and so it was not possible to obtain as high intensities for the TE case.

Fig 6.4 shows the results of the same experiment performed with the laser cw. This plot is much more linear than Figs. 6.2 or 6.3, for which the laser was used modelocked. It should be noted that the average intensities used for Figs. 6.2 and 6.4 are approximately equal, but the peak intensities are two orders of magnitude higher in Fig. 6.2, because the laser was used modelocked. Because the average intensities were similar, any thermal effects would also have been similar for the two cases. The linearity of Fig. 6.4 compared with the graphs for the modelocked case implies that the nonlinearity of Figs. 6.2 and 6.3 was not be caused by effects which are long-lived compared with the modelocked pulse separation of 13 ns, such as thermal effects.

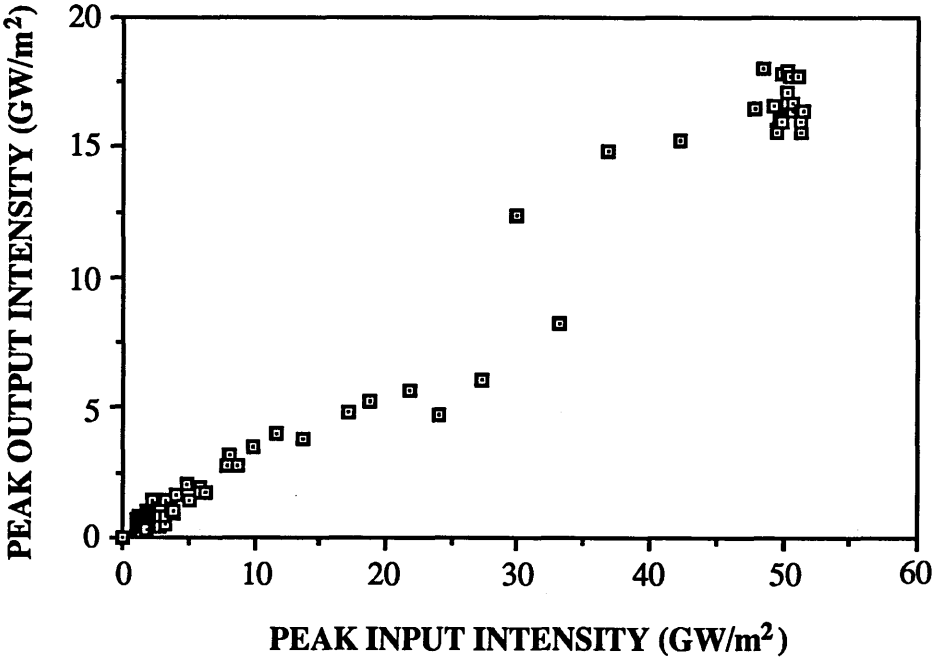

Figure 6.4 Relationship between the input and output intensity for a cw YAG beam of TM polarisation in a GaAs/AlGaAs MQW waveguide

6.2 ANALYSIS OF SINGLE BEAM NONLINEAR ABSORPTION EXPERIMENTS

6.2.1 With TM polarised light

In order to evaluate β from Fig. 6.2, the reciprocal of the input intensity is plotted against the reciprocal of the output intensity, as shown in Fig. 6.5(a).

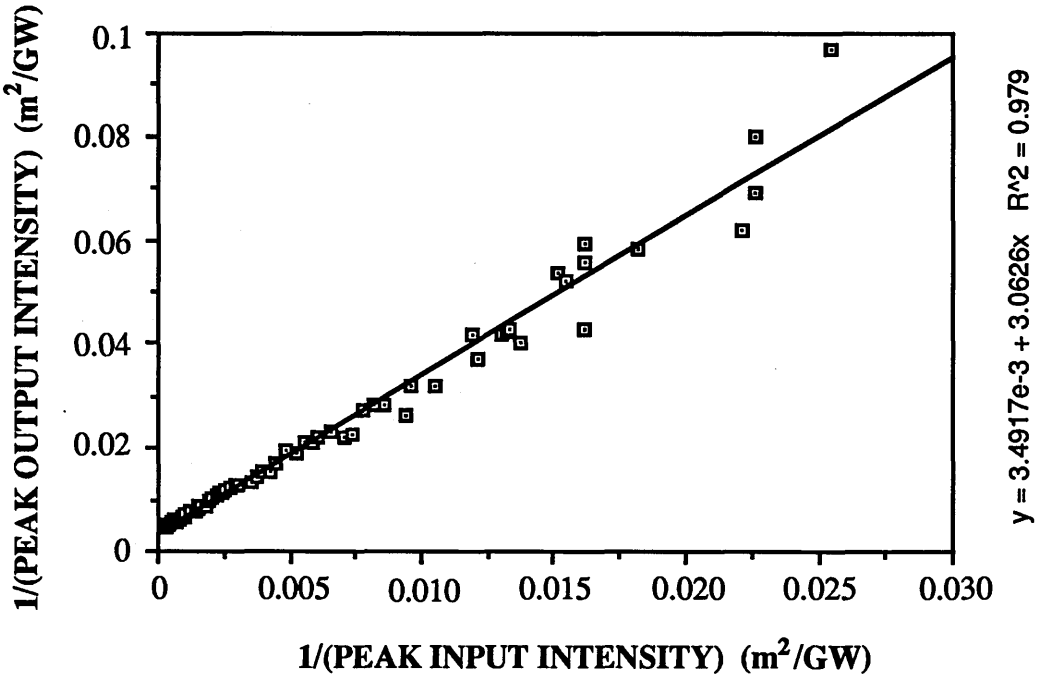

Figure 6.5(a) Relationship between the reciprocals of the input and output peak intensity for a modelocked YAG laser beam of TM polarisation.

It is initially assumed that the nonlinearity is caused by TPA alone, so that the effect of FCA is neglected. For this case, the TPA coefficient β can be found from this graph using Eqn. 6.5, which is repeated below.

$$\text{Intercept} = \left[\frac{1}{I(L)}\right]_{I(0)\to\infty} = \frac{\beta(1-e^{-\alpha z})}{\alpha e^{-\alpha z}} \qquad (6.6)$$

It can be seen from Fig. 6.5(a) that the intercept is 3.49×10^{-3} m^2 GW^{-1}. The linear absorption coefficient α had been previously found by both sequential cleaving and Fabry-Pérot loss measurements to be about 1.25 cm^{-1}, and the waveguide was 10 mm long. When these values are inserted into Eqn. 6.6, it is found that $\beta=2.03\times10^{-10}$ m W^{-1}. Because Fig. 6.5(a) is a graph of reciprocal intensities, there will be a higher degree of uncertainty in those points furthest from the origin. In order to

increase the accuracy of measurement of the intercept, Fig. 6.5(a) is therefore replotted with only those points for which 1/(peak input intensity)>10^{-11} m^2W^{-1}. The resulting graph is shown in Fig. 6.5(b).

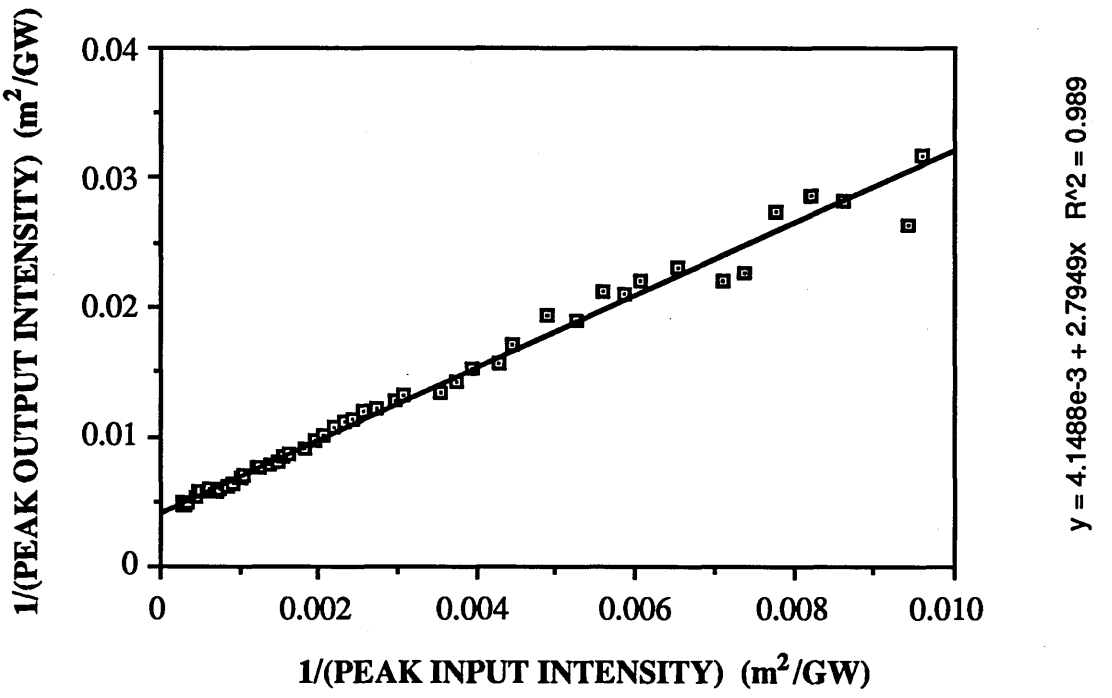

Figure 6.5(b) Replot of Fig. 6.5(a), except for the exclusion of any data points for which 1/(peak input intensity)>10^{-11} m^2W^{-1}.

The intercept in Fig. 6.5(b) is equal to $4.15\times10^{-3}\,m^2\,GW^{-1}$. When this is inserted into Eqn. 6.6, it is found that $\beta=2.41\times10^{-10}$ m W^{-1}.

If we now consider that FCA plays some part in the nonlinearity, then a new estimate of β must be made. This can be achieved using either Eqn. 5.21 or 5.22. In order to decide which of these equations to use, the sign of q must first be decided. Since τ=35 ns and t_p=13 ns, F can be found from Eqn. 5.13 to be 3.22. When this is inserted into Eqn. 5.15, together with the other values of $\alpha=125\ m^{-1}$, $\sigma_{ex}=5\times10^{-22}\,m^2$ (*Van Stryland 1985*), T=75 ps and $h\nu$=1.167 eV, it is found that

$$\gamma = (2.87\times10^{-13}\beta)\ \ m^3W^{-2} \tag{6.7}$$

which leads to

$$q = 4\alpha\gamma - \beta^2 = \left[1.43\times10^{-10}\beta - \beta^2\right]\ m^2W^{-2} \tag{6.8}$$

It can therefore be seen that for $\beta>1.43\times10^{-10}$ m W^{-1}, q<0, and vice versa. As we do not yet know whether β is greater or smaller than 1.43×10^{-10} m W^{-1} when FCA

is taken into account, it will be necessary to use both Eqn. 5.21 and Eqn. 5.22 in turn in order to find out which of them is suitable for the particular experimental parameters. We will first use Eqn. 5.21, which is relevant for $q<0$.

Let us consider this equation as $I(0)\rightarrow \infty$, i.e. at the same intercept used previously to determine β while neglecting FCA. Eqn. 5.21 then becomes

$$\log\left(\frac{I(L)^2}{\alpha+\beta I(L)+\gamma I(L)^2}\right)-\log\left(\frac{1}{\gamma}\right)=\frac{\beta}{\sqrt{-q}}\log\left(\frac{2\gamma I(L)+\beta-\sqrt{-q}}{2\gamma I(L)+\beta+\sqrt{-q}}\right)-2\alpha L \tag{6.9}$$

Here, I(L) is the output intensity for infinite input intensity, found from the reciprocal of the intercept of Fig. 6.5(b) to be $2.41\times10^{11}\ Wm^{-2}$. We also insert into Eqn. 6.9 the parameters $\alpha=125\ m^{-1}$, $\gamma=(2.87\times10^{-13}\beta)\ m^3W^{-2}$ (from Eqn. 6.7), $q=(1.43\times10^{-10}\beta-\beta^2)\ m^2W^{-2}$ (from Eqn. 6.8). A value for β can then be found graphically as shown in Fig. 6.6.

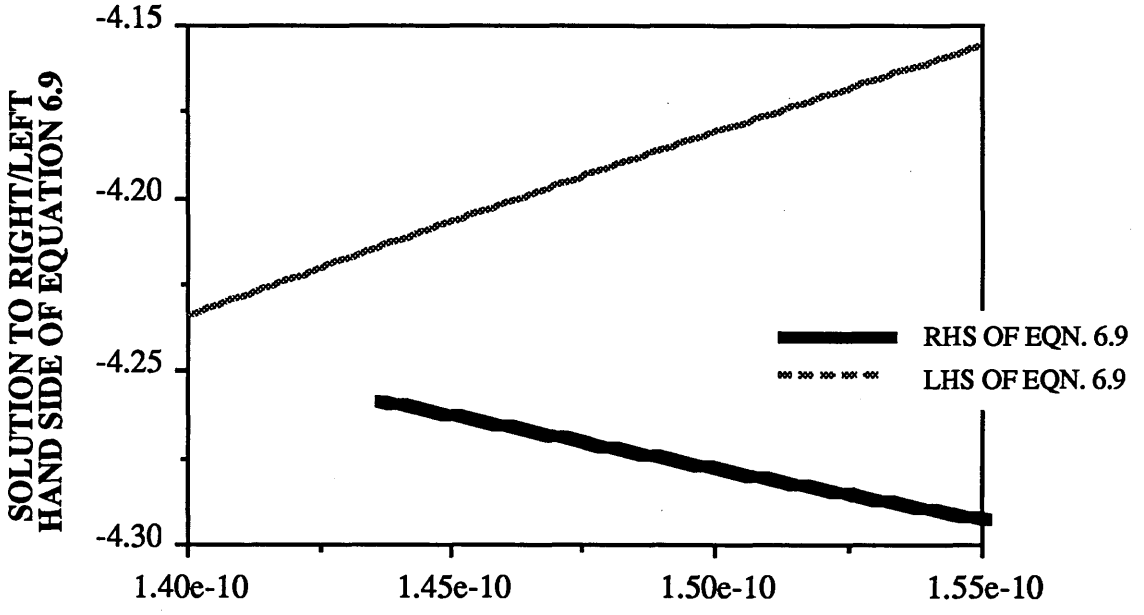

Figure 6.6 Graphical representation of Eqn. 6.9

The dotted line in Fig. 6.6 is a plot of the left-hand side of Eqn. 6.6, and the solid line is a plot of the right-hand side. It can be seen that the left-hand side does not contain q, so that it can always be evaluated, no matter what value is chosen for β. This is not the case for the right-hand side of Eqn. 6.6, which cannot be evaluated for $\beta<1.43\times10^{-10}\ m\ W^{-1}$, as q would then become positive, and $\sqrt{-q}$ would then become complex. This can be seen in Fig. 6.6, as the solid line ends when $\beta=1.43\times10^{-10}\ m\ W^{-1}$. Because the solid line ends before the two lines meet, β must be

smaller than $1.43\text{x}10^{-10}$ m W^{-1}, and so it is not possible to obtain a value for β using Eqn. 6.6.

We therefore must use Eqn. 5.22 in the analogous way to evaluate β. As $I(0)\rightarrow\infty$, this becomes

$$\log\left(\frac{I(L)^2}{\alpha+\beta I(L)+\gamma I(L)^2}\right)-\log\left(\frac{1}{\gamma}\right)=\frac{2\beta}{\sqrt{q}}\tan^{-1}\left(\frac{2\gamma I(L)+\beta}{\sqrt{q}}\right)-\frac{\beta\pi}{\sqrt{q}}-2\alpha L \qquad (6.10)$$

This can be solved graphically in the same way as Eqn. 6.9, and the result is shown in Fig. 6.7.

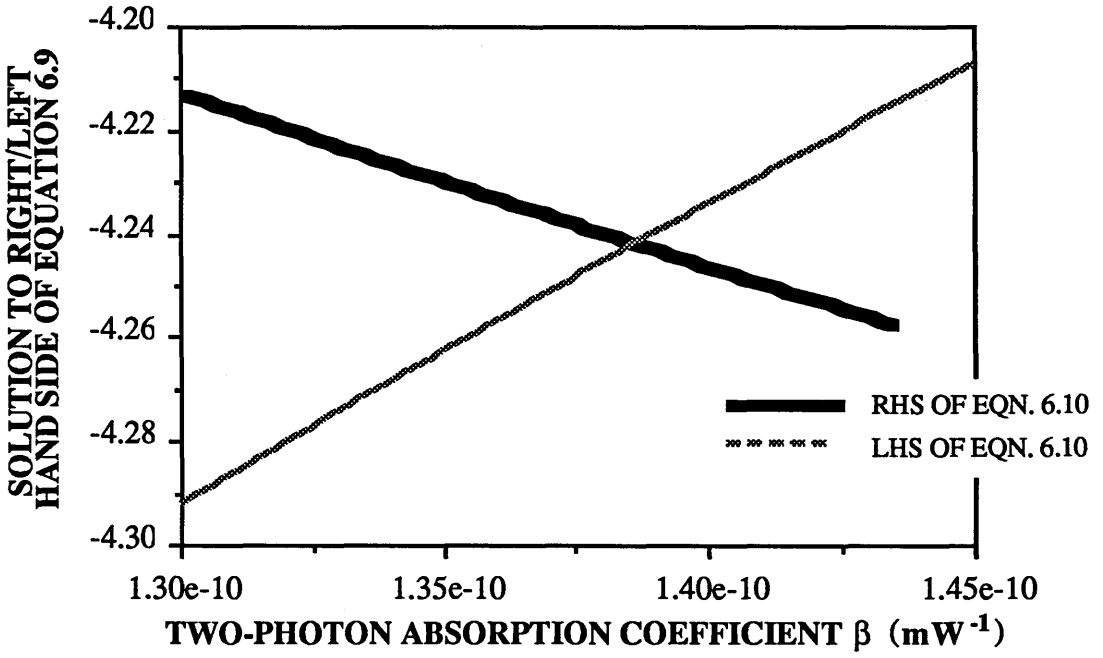

Figure 6.7 Graphical representation of Eqn. 6.10

It can be seen that the two lines in Fig. 6.7 intercept at $\beta=1.39\text{x}10^{-10}$ m W^{-1}, and so this is the value for the two-photon absorption coefficient when free carrier absorption is also taken into account.

All the experimental data used so far in this section was for the case of a 3.5 μm wide rib. This experiment was repeated for several other rib widths, and the working of this section can be repeated for this data also. It was found to be sometimes necessary to use Eqn. 6.9 to calculate β, and sometimes Eqn. 6.10 was used, depending on whether β was greater or smaller than $1.43\text{x}10^{-10}$ m W^{-1}. All the results of this working are shown in Table 6.1, in order to give an indication of their spread.

RIB WIDTH (μm)	MODE AREA ($x10^{-12}$ m^2)	β (NEGLECTING FREE CARRIER ABSORPTION) ($x10^{-10}$ m W^{-1})	β (INCLUDING FREE CARRIER ABSORPTION) ($x10^{-10}$ m W^{-1})
1.5	5.83	2.80	1.67
1.5	5.83	4.23	2.77
1.5	5.83	1.50	0.75
1.5	5.83	2.81	1.68
2.0	4.87	1.44	0.71
2.0	4.87	1.85	0.99
2.0	4.87	3.55	2.24
2.5	4.20	3.56	2.25
3.5	3.76	0.88	0.36
3.5	3.76	1.81	0.96
3.5	3.76	1.01	0.44
3.5	3.76	2.41	1.39
4.0	3.92	1.93	1.05
4.5	4.00	1.53	0.77
4.5	4.00	2.21	1.24
5	4.09	1.54	0.77
5	4.09	2.41	1.39
5.5	4.18	2.76	1.65

TABLE 6.1

It can be seen from Table 6.1 that there is a high degree of uncertainty in the measurement of β. The mean found for β when the effect of FCA was neglected was $2.24x10^{-10}$ m W^{-1}, and the standard deviation was $8.9x10^{-11}$ m W^{-1}, (40% of the mean). The reason for this large fractional standard deviation can be seen when Eqn. 6.6 is considered. This can be rearranged as

$$\beta = \frac{A\,\alpha\, e^{-\alpha z}}{P(z)(1-e^{-\alpha z})} \tag{6.11}$$

where A is the mode area and P(z) is the peak output power for infinite peak input power. If $\alpha \approx 125$ m^{-1}, then a 10% uncertainty in α leads to about a 7% uncertainty in β. So the fractional uncertainty in β can be written as

$$\frac{\Delta\beta}{\beta} \approx \frac{\Delta A}{A} + \frac{\Delta P}{P} + \frac{0.7\Delta\alpha}{\alpha} \tag{6.12}$$

The mode area was calculated using FWave (see Section 3.2.2), and its uncertainty is estimated to be about 20%. The uncertainty in the peak power results mainly because the radius of the iris is critical. If it is too large, light guiding in the slab may be incident on the photodiode, and if it is too small, some light from the rib may be blocked or there may be diffraction effects, so that not all of the light guiding in the rib reaches the photodiode. There are also uncertainties in the calibration of the photodiode, and in the factor used to convert from average to peak power, so that the total uncertainty in the peak intensity is estimated to be about 20%. If the uncertainty in α is taken to be about 10%, then the total uncertainty in β is about 47%, which is comparable to the fractional standard deviation found for β experimentally.

The mean obtained for β when the effect of FCA was included was 1.28×10^{-10} m W^{-1}, and the standard deviation in the experimental values was now about 50% of the mean. The uncertainty can be estimated by considering Eqns. 6.9 and 6.10. There is an uncertainty of approximately 40% in I(L), as estimated in the previous paragraph from a 20% uncertainty in both the mode area and power readings. Consider the example of the 3.5 μm rib already described in detail in this section, for which $I(L)=2.41 \times 10^{11}$ Wm^{-2}, and $\alpha \approx 125$ m^{-1}. In order to find the expected uncertainty in β, the value for I(L) is altered by 40%, and α by 10%. These new values are then substituted into Eqn. 6.10, and a new value for β obtained which differs from the true value by about 100%.

6.2.2 With TE polarised light

The experiments and calculations of the preceding section are now repeated for TE polarised light instead of TM. For this polarisation, the linear absorption coefficient α had been measured by both sequential cleaving and Fabry-Pérot loss measurements to be about 90 m^{-1}. Figure 6.8 is a graph of the reciprocal of the input intensity against the reciprocal of the output intensity for the same experimental data shown in Figure 6.3.

Table 6.2 shows the results of experiments carried out with waveguides of various rib widths. From Table 6.2, the mean obtained for β when the effect of FCA was neglected was 2.70×10^{-10} m W^{-1}, and the standard deviation was 8.3×10^{-11} m W^{-1} (31% of the mean). When the effect of FCA was included, the mean obtained for β was 1.97×10^{-10} m W^{-1}, and the standard deviation was 38% of the mean.

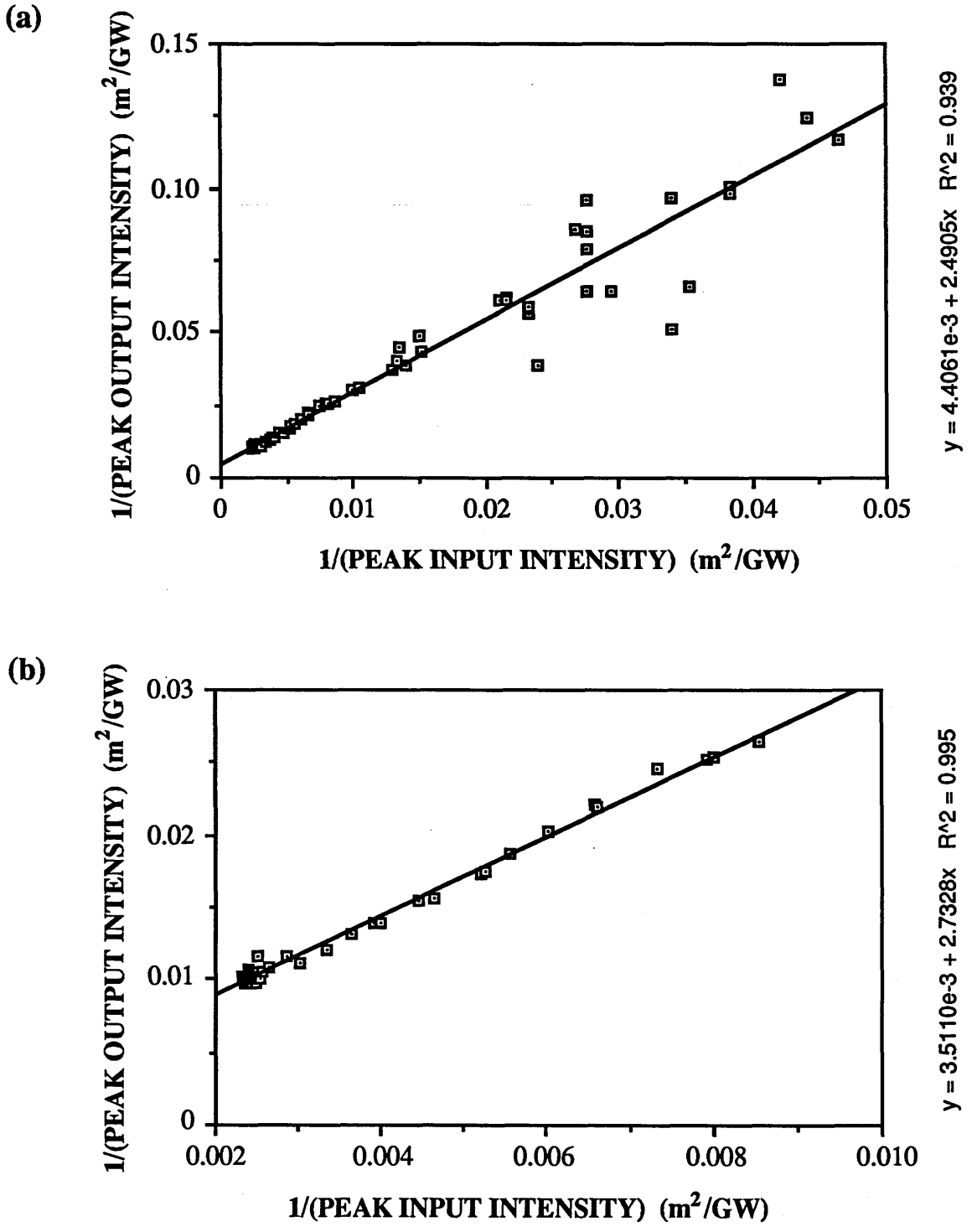

Figure 6.8 Relationship between the reciprocals of the input and output peak intensity for a modelocked YAG laser beam of TE polarisation. Plot (b) differs from plot (a) only in the exclusion of any data points for which 1/(peak input intensity)>$1x10^{-11}$ m^2/W.

RIB WIDTH (μm)	MODE AREA ($x10^{-12}$ m^2)	β (NEGLECTING FREE CARRIER ABSORPTION) ($x10^{-10}$ m W^{-1})	β (INCLUDING FREE CARRIER ABSORPTION) ($x10^{-10}$ m W^{-1})
1.5	2.80	2.34	1.64
1.5	2.80	3.33	2.52
2.0	3.06	1.71	1.11
3.5	2.9	4.70	3.77
3.5	2.9	2.79	2.03
4.0	3.02	2.13	1.45
4.5	3.14	2.13	1.46
5	3.27	2.55	1.82
5.5	3.39	2.62	1.89

TABLE 6.2

6.2.3 With cw light

It is also possible to estimate β in the same way from a cw plot, as shown in Fig. 6.9(a) and (b).

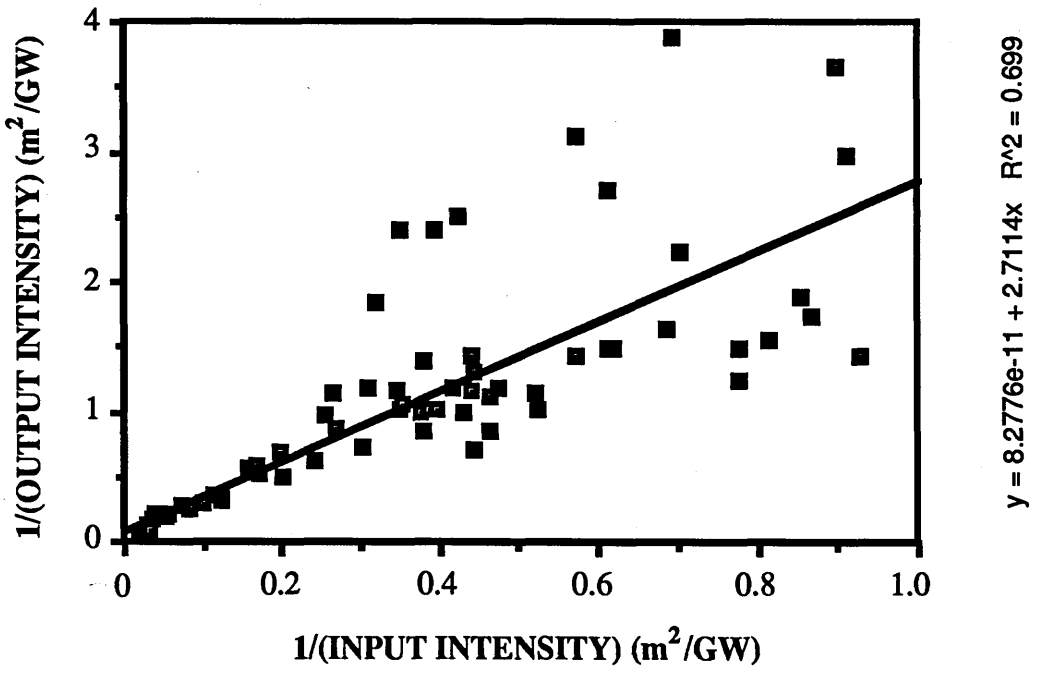

Figure 6.9(a) Relationship between the reciprocals of the input and output intensity for a cw YAG laser beam of TM polarisation.

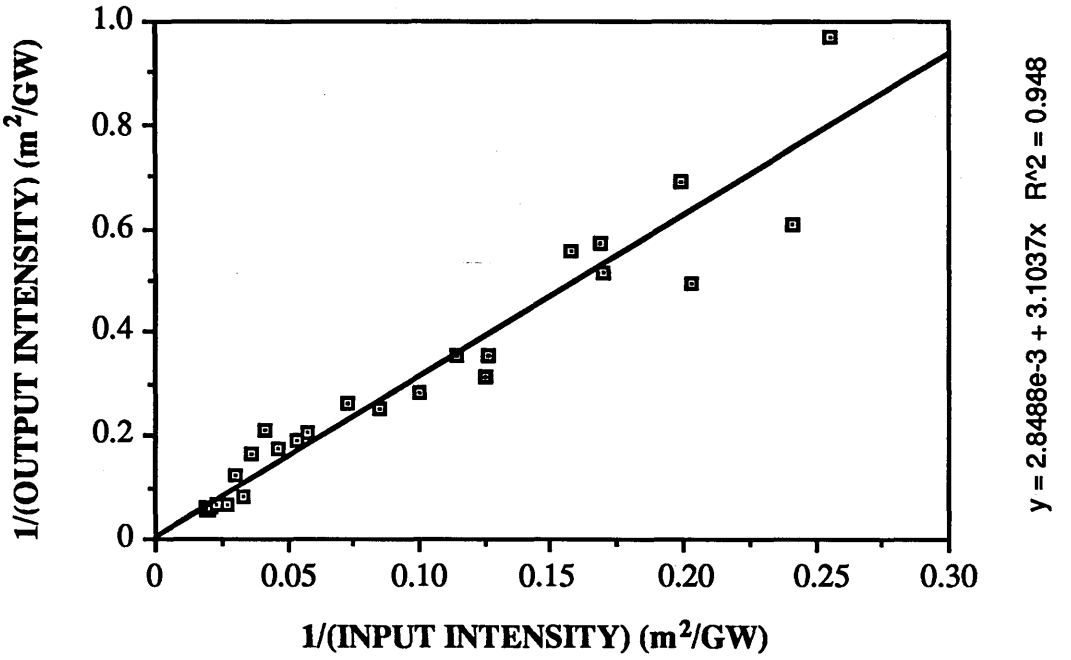

Figure 6.9(b) Replot of Fig. 6.9(a), except for the exclusion of any data points for which 1/(peak input intensity)>2.5×10^{-10} m^2/W.

For this case, β is found to be about 1.7×10^{-10} m W^{-1} from Fig. 6.9(b), although it should be noted that this value varies significantly depending on the number of points which are included in the graph. The laser was TM polarised and the rib width was 4.5 μm. In theory, β can be estimated from cw measurements of transmission as well as from modelocked measurements, although the uncertainty can be prohibitively high, because the accuracy with which the intercept can be obtained is much less.

6.3. PUMP-PROBE NONLINEAR ABSORPTION EXPERIMENTS - CHANGE IN PUMP-PROBE DELAY TIME FOR FIXED PUMP INTENSITY

In order to investigate the cause of the observed nonlinear absorption of the waveguide more fully, further experiments were performed with two beams travelling through the guide simultaneously. One of these was a high-intensity pump beam and the other was a low-intensity probe beam, whose input intensity remained constant, and whose output intensity was continuously measured as a function of the relative delay between the pump and probe pulses. The experimental results are compared to the theoretical model described in Chapter 5.

6.3.1 EXPERIMENTAL ARRANGEMENT

The experiment was set up as in Fig 6.10. The pump-probe delay line was arranged so that at its central point the pump and probe pulses were approximately overlapped in time. This was achieved by removing the waveguide from the end-fire rig, and placing an InGaAs photodiode with a rise time of 30 ps in the path of the two beams. The photodiode was connected to a sampling oscilloscope with a S-6 sampling head whose rise time was about 30 ps, and this was triggered from a synchronous output port on the laser modelocker's acousto-optic control box. The pump beam was first blocked out and the probe pulse was centred on the oscilloscope. The delay line was put to its central position, and the probe beam was then blocked. The position of the delay line on the table was then adjusted until the pump pulse was also centred on the oscilloscope.

The polarisation of the pump was orthogonal to that of the probe, so that the beams could be spatially separated by the polarising beam-splitter cube on emerging from the guide. (Separating the pump and probe beams before the photodiode helped to ensure that any detected nonlinearity occurs in the waveguide, and not in the photodiode). The probe beam was chopped at about 400 Hz, and the pump beam was chopped at 1 Hz. The output probe intensity was read into the computer from the lock-in amplifier, and the output pump intensity was read into the computer from the power meter. Readings of pump and probe intensities were taken for several cases of pump intensity.

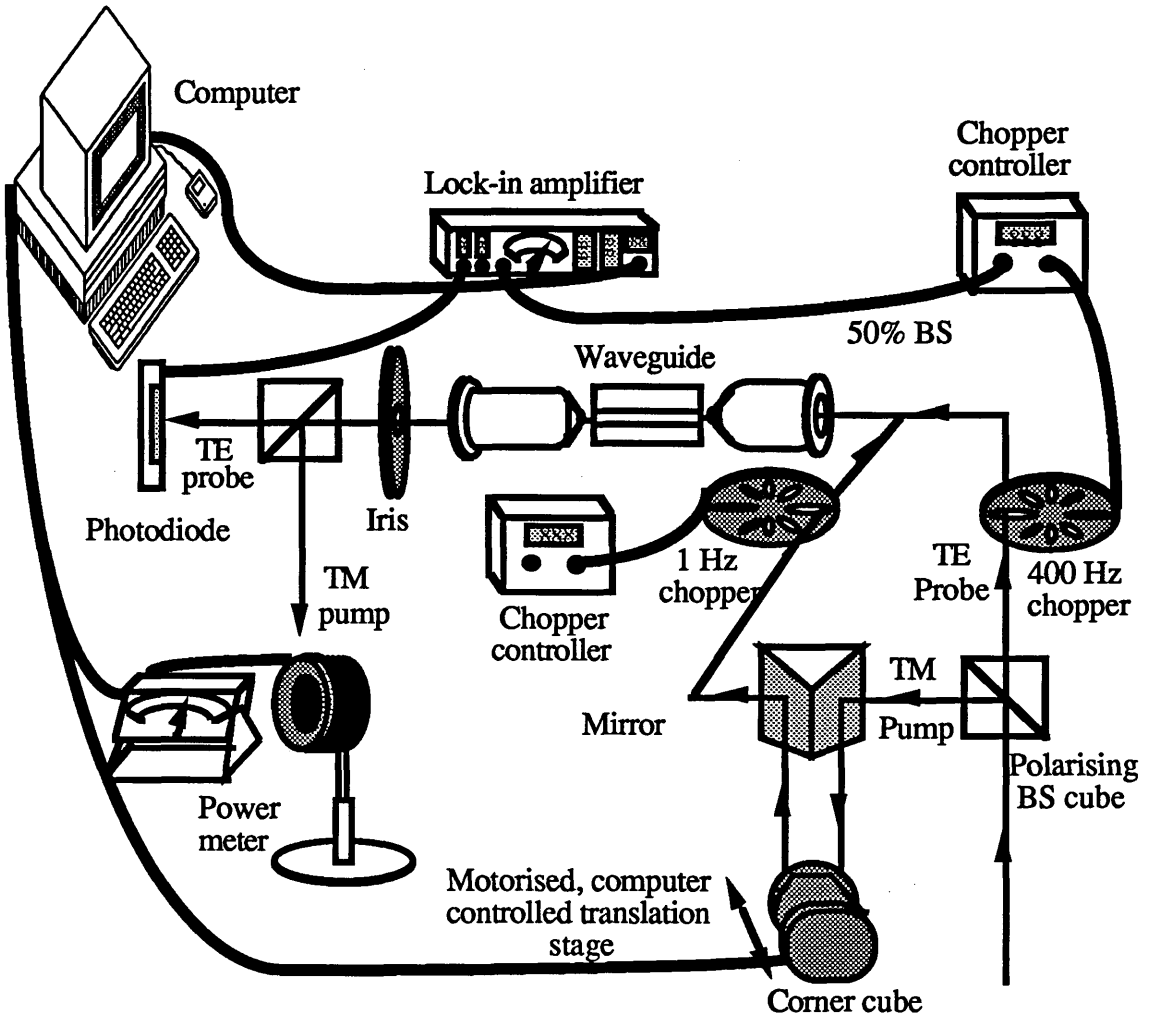

Figure 6.10 Experimental set-up for pump-probe nonlinear absorption experiment with fixed pump intensity and variable pump-probe delay time

6.3.2 EXPERIMENTAL RESULTS

It was found that the output intensity of the probe beam varied at 1 Hz in the presence of a 1 Hz pump beam, but 180° out of phase with the pump beam, so that the output probe intensity was lower when the pump was present, and higher when it was absent. This is because, when the pump beam is incident on the sample, the overlapping probe beam's intensity is added to that of the pump, and so the percentage transmitted decreases due to a combination of increased TPA and FCA.

Fig 6.11 shows the transmission of a probe beam of about 0.5 mW output power, in the presence of a pump beam whose output peak intensity is about 1.17×10^{11} Wm^{-2} in the rib (4 mW average power). The y-axis of this graph shows the difference between the percentage transmission of the probe beam when the pump beam is present and the percentage transmission of the probe when the pump is absent. It can be seen that as the time delay between the pump and probe is changed, the percentage

decrease in transmission of the probe in the presence of the pump changes. It can be seen that the graph is almost symmetrical about the point where the pump-probe delay time is zero. This implies that this pump intensity has created very few free carriers, so that TPA is the dominant mechanism for the nonlinear absorption changes.

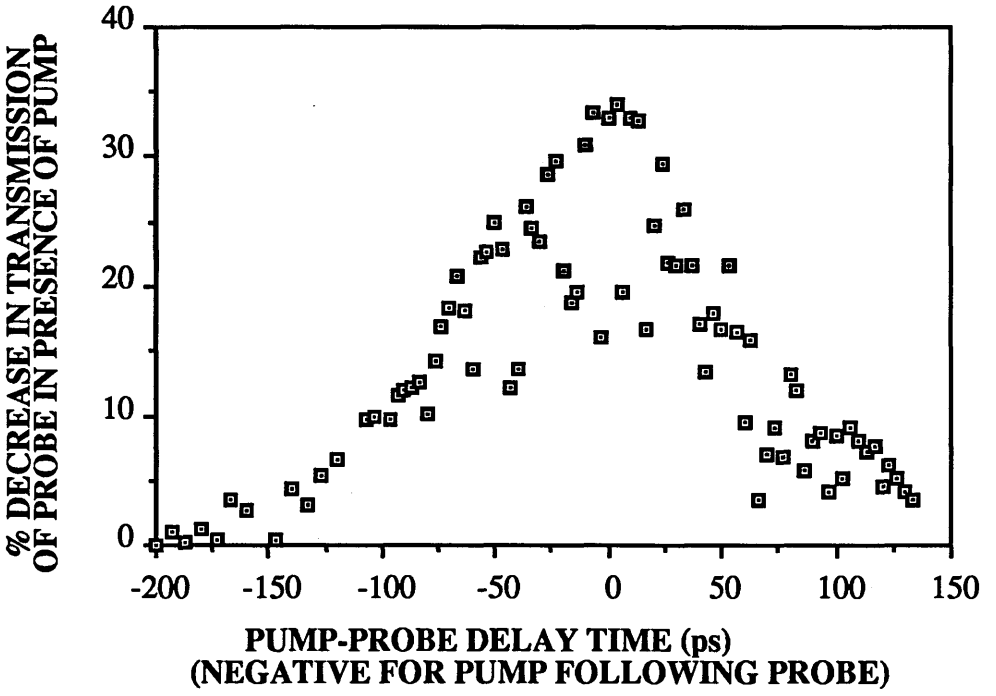

Figure 6.11 Time-resolved nonlinear absorption of TE probe due to a TM pump of peak input intensity 4.5×10^{11} Wm^{-2}.

When an identical experiment is carried out for a higher output peak pump intensity of about 2.16×10^{11} Wm^{-2} in the rib (about 7.5 mW average power), significantly different results are obtained (Fig. 6.12). It can be seen that the graph is now neither symmetrical nor Gaussian in shape, except when the pump and probe beams are very close to each other in time. When the pump enters the sample a long time (>100 ps) before the probe, there is still a considerable nonlinear absorption change for the probe. This is because the pump generates a significant number of free carriers, which absorb some of the probe beam. Similarly, when the pump enters the sample a long time (>100 ps) after the probe, there is a smaller, but still significant, nonlinear absorption change for the probe. This is due to the fraction of free carriers still remaining from the pump pulse 13 ns previously.

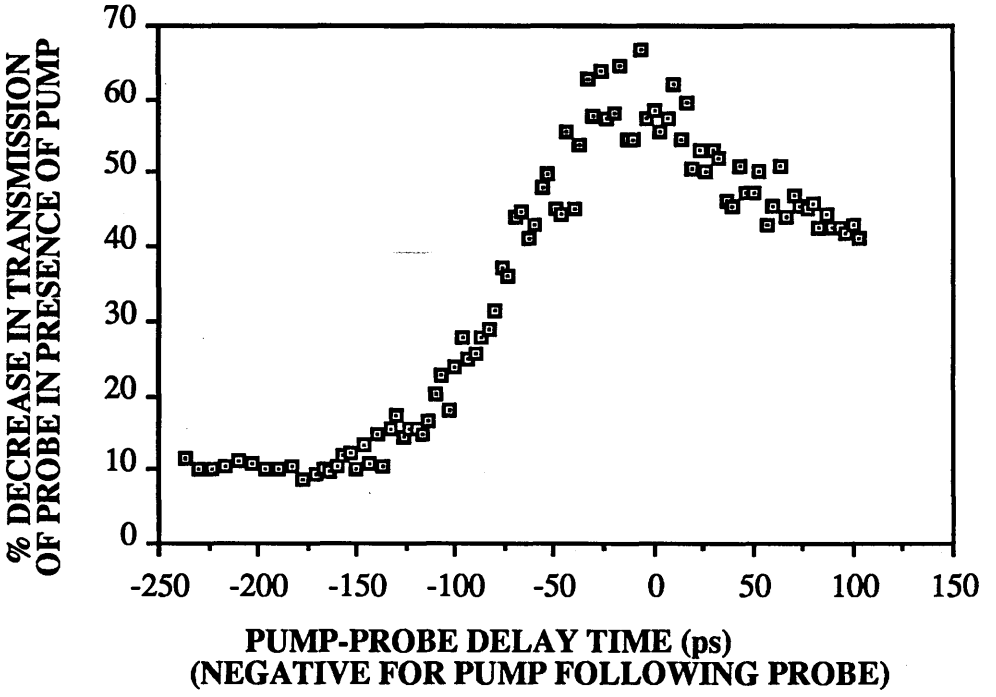

Figure 6.12 Time-resolved nonlinear absorption of TE probe due to a TM pump of peak input intensity 1.5×10^{12} Wm^{-2}.

6.3.3 FITTING OF RESULTS TO THEORETICAL MODEL

The experimental results shown in Figs. 6.11 and 6.12 can be fitted to the theoretical model described in Section 5.3. The input peak pump and probe intensities are substituted into Eqn. 5.47 together with the other experimental parameters such as α=125 m^{-1}, β=1.3×10^{-10} m W^{-1}, τ=35 ns, T=75 ps and L=0.01 m. This equation is then integrated numerically using Simpson's Rule, and the resulting fits to the experimental data of Figs. 6.11 and 6.12 are shown in Figs. 6.13 and 6.14 respectively.

The value of the carrier lifetime τ was varied, and the optimum fit to the experimental data, as shown in Figs. 6.13 and 6.14, was obtained when τ was taken as 35 ns. This figure for the carrier lifetime is in excellent agreement with the measurement using time-resolved photoluminescence (see Section 5.1.3). The accuracy of the fit to the theoretical model is perhaps surprising, as no account of carrier diffusion has been made in the model. The speed of the carrier diffusion is dominated by that of the slower holes, and a typical diffusivity for holes is about 10 cm^{2}s^{-1} *(Sze 1985)*. The time taken for the holes to diffuse a distance of 2 μm (the distance from the centre of the mode in the waveguide to the half-intensity point) is therefore about 4 ns. This is much shorter than the carrier lifetime, so that diffusion would be expected to lead to an apparently much shorter lifetime. However, Fig. 6.14 shows that this is not the case.

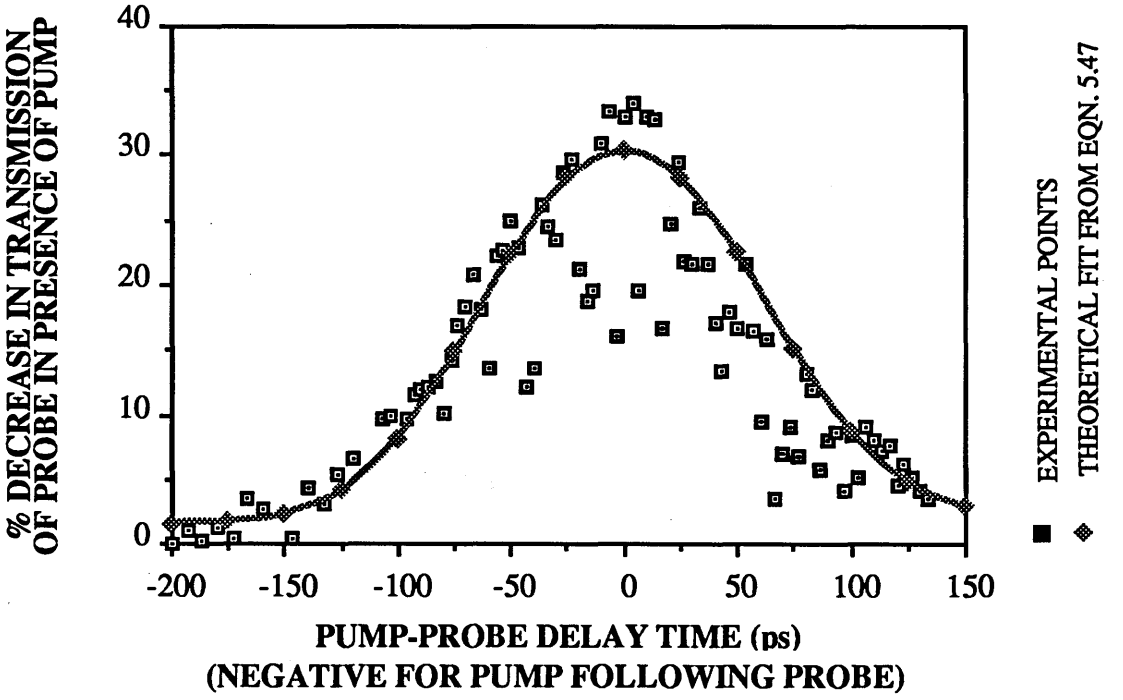

Figure 6.13 Time-resolved nonlinear absorption of TE probe due to a TM pump of peak input intensity 4.5×10^{11} Wm^{-2} fitted to theory. The solid line is the theoretical fit.

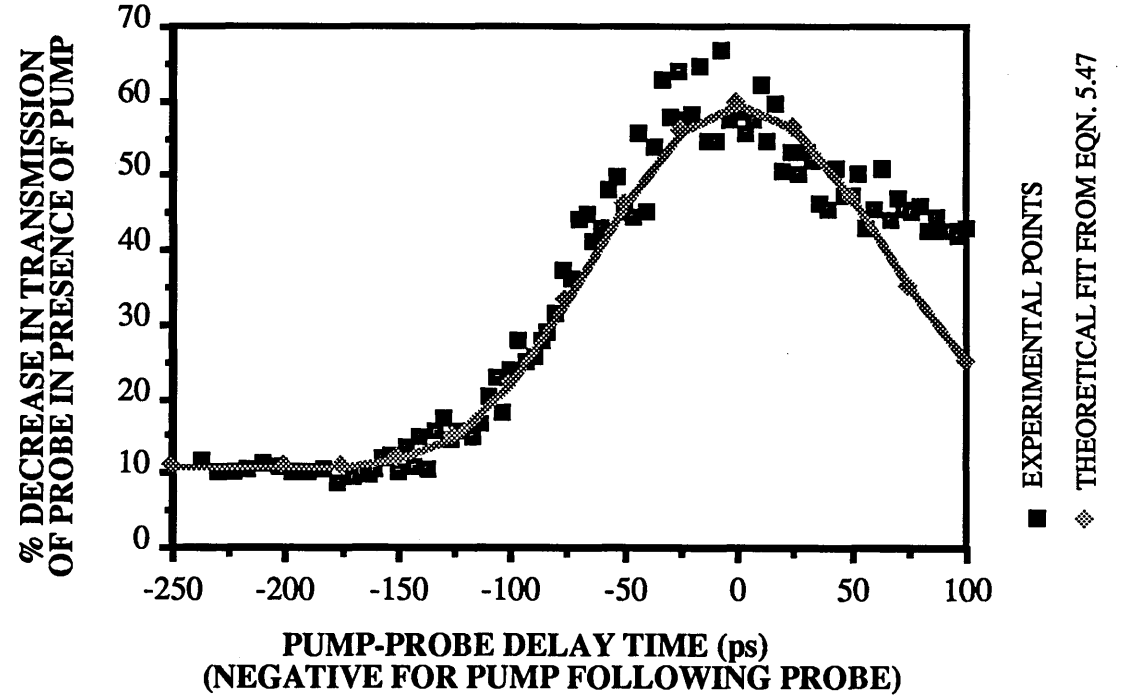

Figure 6.14 Time-resolved nonlinear absorption of TE probe due to a TM pump of peak input intensity 1.5×10^{12} Wm^{-2} fitted to theory. The solid line is the theoretical fit.

6.4. PUMP-PROBE NONLINEAR ABSORPTION EXPERIMENTS - CHANGE IN PUMP INTENSITY FOR FIXED PUMP-PROBE DELAY TIME

In these experiments, the relative delay between the pump and probe pulses was kept constant and a continuously variable attenuator wheel was put in the path of the pump beam instead of the 1 Hz chopper. In this case, the pump beam's intensity was varied, although it was always kept at least as intense as the probe, and the effect of the pump's intensity on the probe's transmission was measured.

6.4.1 EXPERIMENTAL RESULTS

Fig. 6.15 contains three plots showing the change in transmission of the probe for various peak pump intensities. In one of these plots the pump and probe are exactly overlapped temporally (t_d=0 ps), in another the pump pulse travels through the waveguide 120 ps before the probe pulse (t_d=120 ps), and in the third the pump pulse is 220 ps after the probe pulse (t_d=-220 ps). It may be seen for low pump intensities, the percentage decrease in transmission of the probe is similar when t_d=120 ps to that when t_d=-220 ps. For high pump intensities, however, the percentage decrease in transmission of the probe when t_d=120 ps is considerably higher than that when t_d=-220 ps, and almost equal to that when t_d=0 ps. This is because for high pump intensities, the effect of FCA becomes much more important.

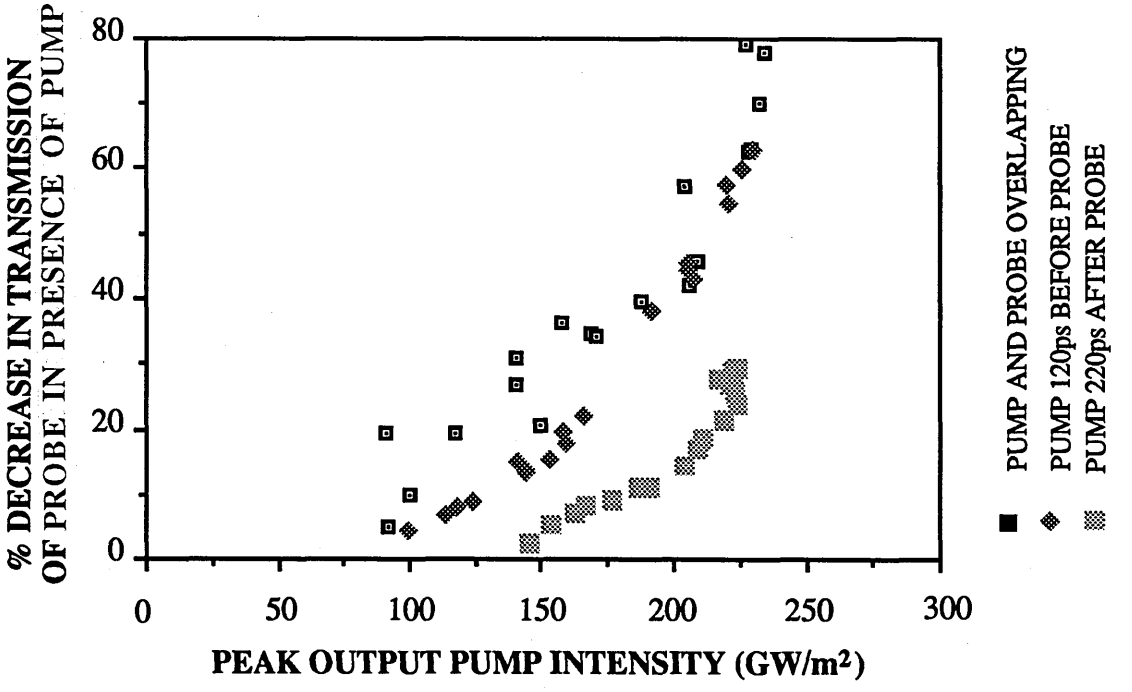

Figure 6.15 Time-resolved nonlinear absorption of TE probe due to a TM pump beam of various intensities.

6.4.2 THEORETICAL FITTING OF RESULTS

Fig. 6.15 can be fitted to the theoretical model of Section 5.3 by numerically integrating Eqns. 5.47 and 5.48 for various peak pump intensities and pump-probe delay times. The results of this are shown in Figs. 6.16-6.18.

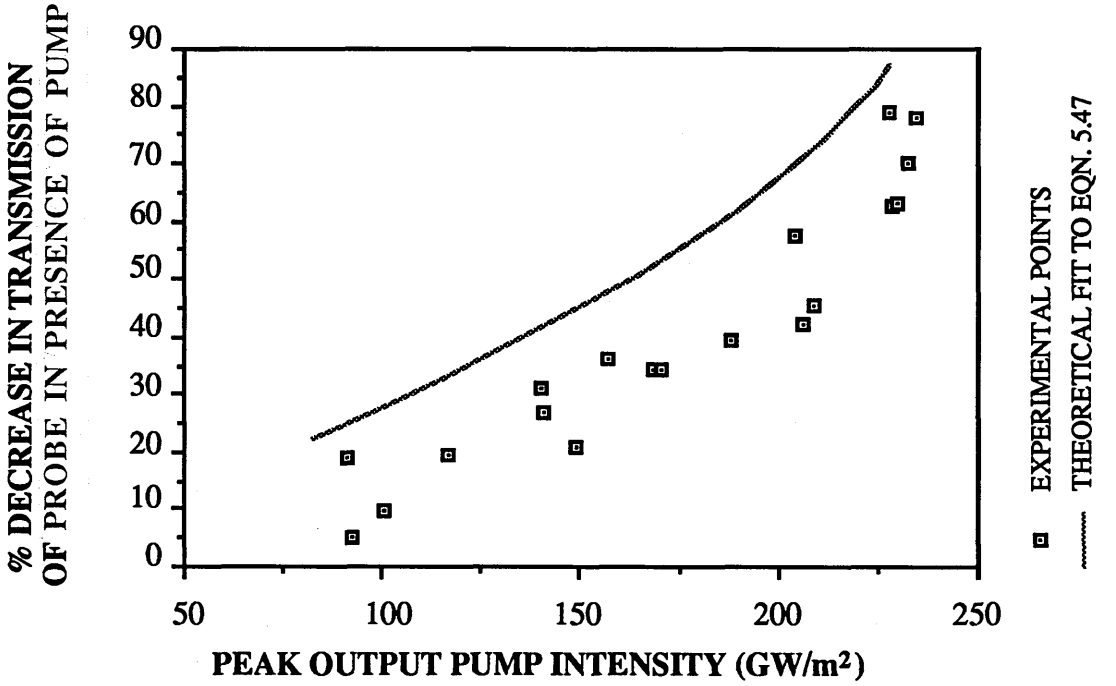

Figure 6.16 Nonlinear absorption of TE probe due to a temporally overlapping TM pump of varying intensity. The solid line is the theoretical fit from Eqn. 5.47.

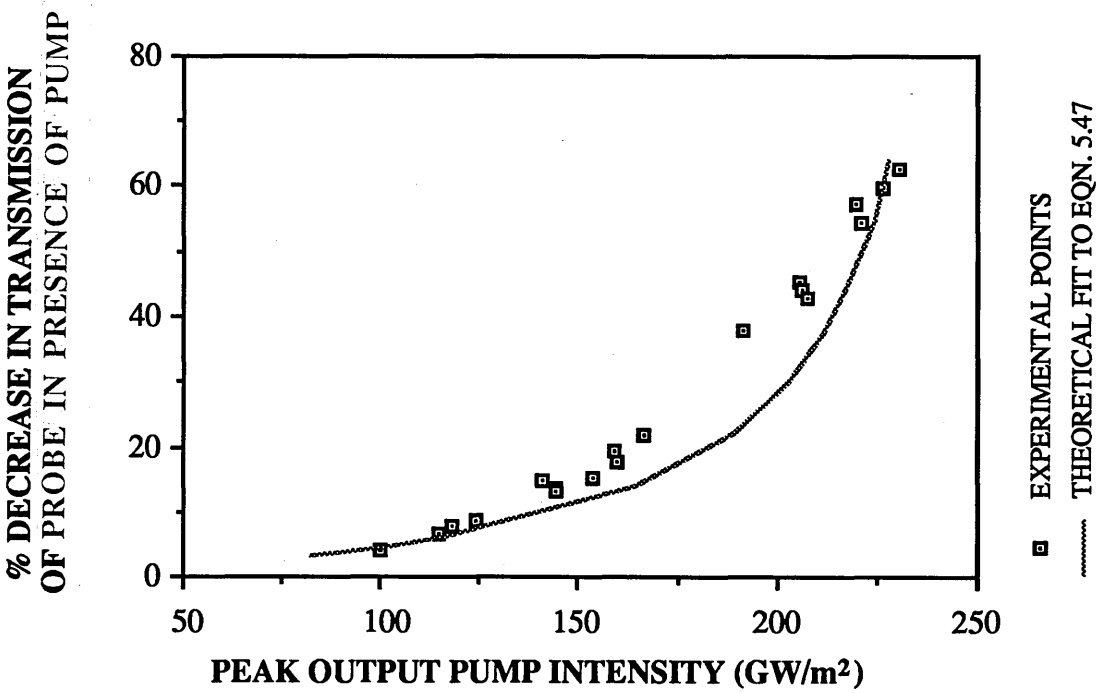

Figure 6.17 Nonlinear absorption of TE probe due to a TM pump of varying intensity preceding the probe by 120 ps. The solid line is the theoretical fit from Eqn. 5.47.

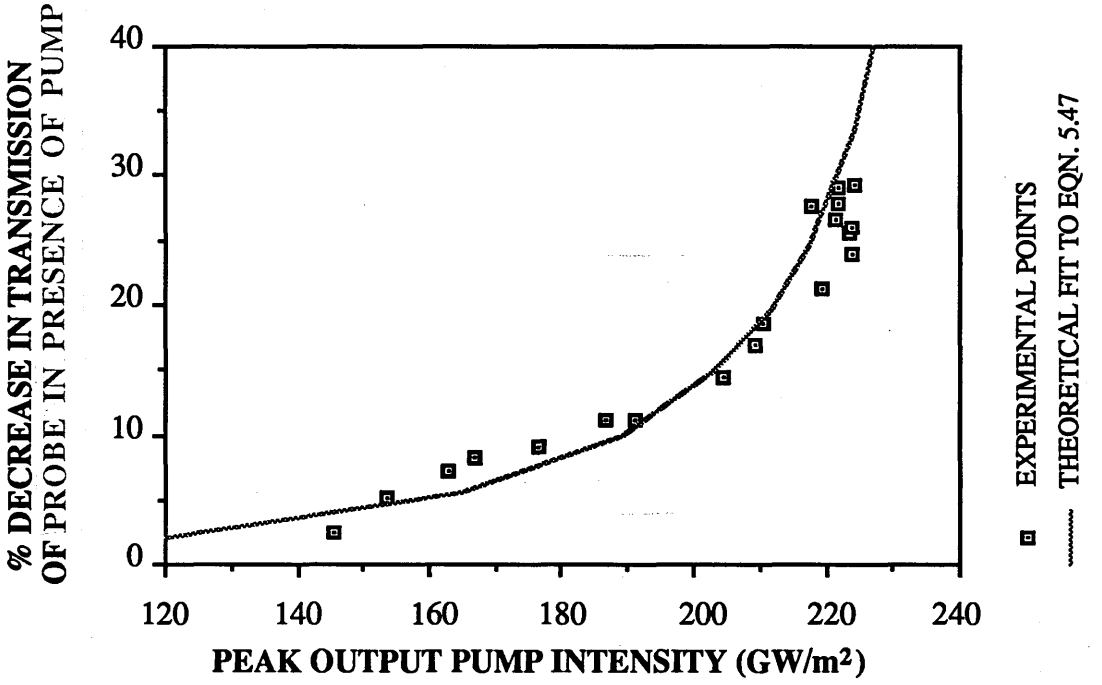

Figure 6.18 Nonlinear absorption of TE probe due to a TM pump of varying intensity which follows the probe by 220 ps. The solid line is the theoretical fit from Eqn. 5.47.

6.5 SUMMARY OF CHAPTER SIX

Chapter Six described nonlinear absorption experiments performed in GaAs/AlGaAs MQW waveguides at 1.06 μm, beginning with experiments with a single beam . When the experiments were analysed in the usual way, neglecting the effect of FCA, the TPA coefficient β was found to be about 2.2×10^{-10} m W^{-1} for TM polarised light, and 2.7×10^{-10} m W^{-1} for TE polarisation. When the theoretical model of Section 5.1.3 was used to include FCA, β was found to be about 1.3×10^{-10} m W^{-1} for TM polarisation and 2.0×10^{-10} m W^{-1} for TE light. All values for β have uncertainties of about 40% and, taking this into account, are in good agreement with other published values for β in GaAs/AlGaAs MQW material *(White et al. 1990* and *Le 1990).*

Pump-probe experiments were carried out, and it was found that an input pump intensity of 4.5×10^{11} Wm^{-2} led to a decrease in the probe transmission of about 30%, while a input pump intensity of 1.5×10^{12} Wm^{-2} led to a decrease of about 65%. For the lower intensity case, the symmetry of the graph of the probe transmission against pump-probe delay time indicated that the nonlinearity was caused by TPA rather than FCA. The persistence of the decrease in probe transmission at large pump-probe delay times showed that the nonlinearity of the higher intensity case was due to both TPA and FCA. Similar graphs were also shown of the probe transmission against pump intensity, and all these graphs were then successfully fitted to the theoretical model of Section 5.3.

CHAPTER SEVEN

NONLINEAR REFRACTIVE INDEX EXPERIMENTS

7.1 CALCULATION OF REFRACTIVE INDEX CHANGE DUE TO TWO PHOTON ABSORPTION

There are various causes of the change in refractive index of a waveguide. The refractive index of a semiconductor has a thermal dependence, so that if the semiconductor absorbs energy from a laser beam, it will heat up, and the band gap will decrease due to the change in lattice constant. Because of this change in the band gap, the refractive index will increase. Another cause arising from real transitions in the semiconductor is that any change in the number of free carriers generated by absorption will modify the plasma frequency, and hence the refractive index of the semiconductor. Thirdly, effects arising from virtual transitions in the semiconductor, such as the ac Quantum Confined Stark Effect, cause a shift in the absorption spectrum and hence, by the Kramers-Krönig Relations, a corresponding shift in the refractive index spectrum.

The experiments which were performed to measure the changes in refractive index involved placing a 1 Hz chopper in the path of the pump beam in order to turn the pump on or off periodically in the waveguide. The shift in fringes of the interferometer was measured as the pump beam was chopped. In this way, the difference in refractive index was measured between the times when the pump was either present in or absent from the waveguide. Because the time constant of the Peltier temperature controller was of the order of milliseconds, and hence much faster than the period of the pump chopper, it was assumed that the temperature of the waveguide remained constant whether the pump beam was on or off. This meant that changes in refractive index due to thermal effects were neglected.

The changes in absorption or refractive index due to real transitions are much greater than those due to virtual transitions, and so it was first assumed that any changes in refractive index were mainly due to electronic effects. The optical dielectric constant is given by *(Kittel 1976)*

$$\varepsilon = 1 - \frac{Ne^2}{\varepsilon_0 m\omega^2} \qquad (7.1)$$

where N is the free carrier density, e is the electronic charge, ω is the band gap frequency and m is the free carrier mass. The refractive index n is equal to the square root of ε, so that if we consider that ΔN free carriers are now created, then it can be shown that the change in refractive index Δn is given by

$$\Delta n = -\frac{\Delta N e^2}{2\varepsilon_0 n m\omega^2} \tag{7.2}$$

where n is the linear refractive index. If it is assumed that all the carriers are generated by two-photon absorption then, as has already been shown in Section 5.1.3(ii), the density of carriers generated per laser pulse is given by

$$N_p = \frac{\beta\sqrt{\pi}\, T I_0^2}{4\hbar\omega} \tag{7.3}$$

where β is the two-photon absorption coefficient, I_0 is the peak intensity of the Gaussian laser pulse, $\hbar\omega$ is the photon energy, and the full pulsewidth at 1/e of the maximum intensity is given by $\sqrt{2}\,T$. Consider two beams present in the waveguide, a strong pump pulse which generates free carriers by two-photon absorption, and hence changes the refractive index, and a weaker probe pulse which monitors this change in refractive index. The density of carriers seen in the waveguide by the probe is $N=FN_p$, where F is the factor depending on the time delay between the pump and probe pulses and also on the carrier lifetime (defined in Section 5.1.3(ii)). The change in refractive index seen by the probe due to the pump is therefore given by

$$\Delta n = -\frac{F\beta\sqrt{\pi}\, T e^2 I_0^2}{8\hbar\omega^3\varepsilon_0 n m} \tag{7.4}$$

If typical experimental values are inserted into (7.3) and (7.4), and if an estimate of the averaged peak pump intensity is used, then it is found that the average carrier density created in the waveguide per pump pulse is about $5\times10^{22}\ m^{-3}$, and the corresponding change in refractive index is about 1×10^{-4}. In order to calculate the phase change in the waveguide more accurately, it is necessary to consider the rate of decay of the pump intensity as it travels through the waveguide. The phase change through the waveguide due to the presence of the pump pulse is given by

$$\Delta\psi = \frac{2\pi}{\lambda}\int_0^L \Delta n\, dz = -\frac{2\pi}{\lambda}\int_0^L \frac{F\beta\sqrt{\pi}\, T e^2}{8\hbar\omega^3\varepsilon_0 n m} I_0^2\, dz = \int_0^L \theta I_0^2\, dz \tag{7.5}$$

If we consider linear and two-photon absorption only, and neglect free carrier absorption, then we can write the phase change as

$$\Delta\psi = -\theta \int_0^L \left[\frac{\alpha}{\beta} I_0 + \frac{1}{\beta} \frac{dI_0}{dz} \right] dz \tag{7.6}$$

$$\Delta\psi = -\frac{\theta\alpha}{\beta} \int_0^L I_0 \, dz - \frac{\theta}{\beta} \int_{I_0(0)}^{I_0(L)} dI_0 \tag{7.7}$$

where L is the waveguide length of about 10 mm. As shown in Appendix Two,

$$\int_0^L I_0 \, dz = \frac{1}{\beta} \ln \left[\frac{\alpha + \beta I_0(0)(1 - e^{-\alpha L})}{\alpha} \right] \tag{7.8}$$

and hence the change in phase of the probe beam due to the pump beam is

$$\Delta\psi = -\frac{\theta\alpha}{\beta^2} \ln \left[\frac{\alpha + \beta I_0(0)(1 - e^{-\alpha L})}{\alpha} \right] + \frac{\theta}{\beta} [I_0(0) - I_0(L)] \tag{7.9}$$

$$\text{where } \theta = -\frac{2\pi}{\lambda} \frac{F \beta \sqrt{\pi} \, T e^2}{8 \hbar \omega^3 \varepsilon_0 n m} \tag{7.10}$$

If typical experimental values are inserted into Eqn. 7.9 for the pump and probe pulses approximately overlapping in time, i.e. α=125 m^{-1}, β=1.3x10^{-10} mW^{-1}, F=3, T=100 ps, L=0.01 m, $\hbar\omega$=1.167 eV, $I_0(0)$=2x10^{12} Wm^{-2}, $I_0(L)$=2x10^{11} Wm^{-2}, then the change in phase is found to be about –0.5 radians, which is equivalent to a change in refractive index of about –10^{-5}.

7.2 INTERFEROMETER ARRANGEMENT

7.2.1 MACH-ZEHNDER INTERFEROMETER

The Mach-Zehnder interferometer is related to the Michelson interferometer, as used in the autocorrelator (see Fig.4.1). It was developed independently by Mach and Zehnder in 1891, and was used extensively in Germany during the Second World War to study air-flow round aeroplanes *(Tolansky 1955)*. Fig. 7.1 shows a Mach-Zehnder interferometer as used to measure the nonlinear refractive index change in a waveguide from the shift in the fringes.

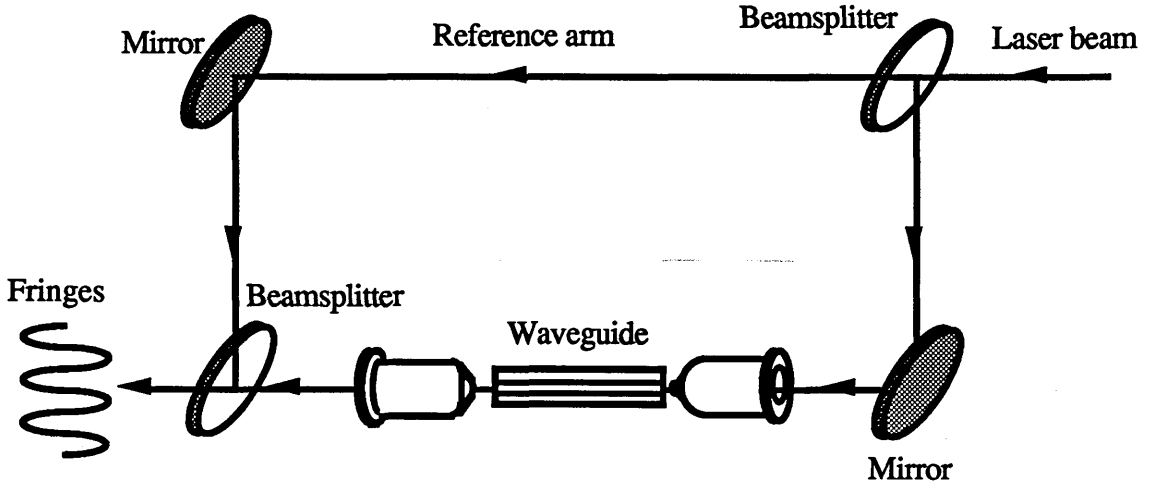

Fig. 7.1 Single-beam Mach-Zehnder interferometer.

When the refractive index of the waveguide changes, the optical length of the waveguide arm changes relative to the reference arm, and there is a shift in the fringe pattern. If the fringe shift in radians is $\Delta\varphi$, the wavelength is λ and the length of the waveguide is L, then the change in refractive index is given by

$$\Delta n = \frac{\lambda \, \Delta\varphi}{2\pi L} \tag{7.11}$$

The interferometer can be used either with a single beam, as shown in Fig. 7.1, or with two beams in a pump-probe configuration. In the single beam case, the intensity or wavelength of the beam could be changed, and the corresponding fringe shift, and hence the refractive index change, would be measured. The interferometer as it would be used with pump and probe beams is shown in Fig. 7.2.

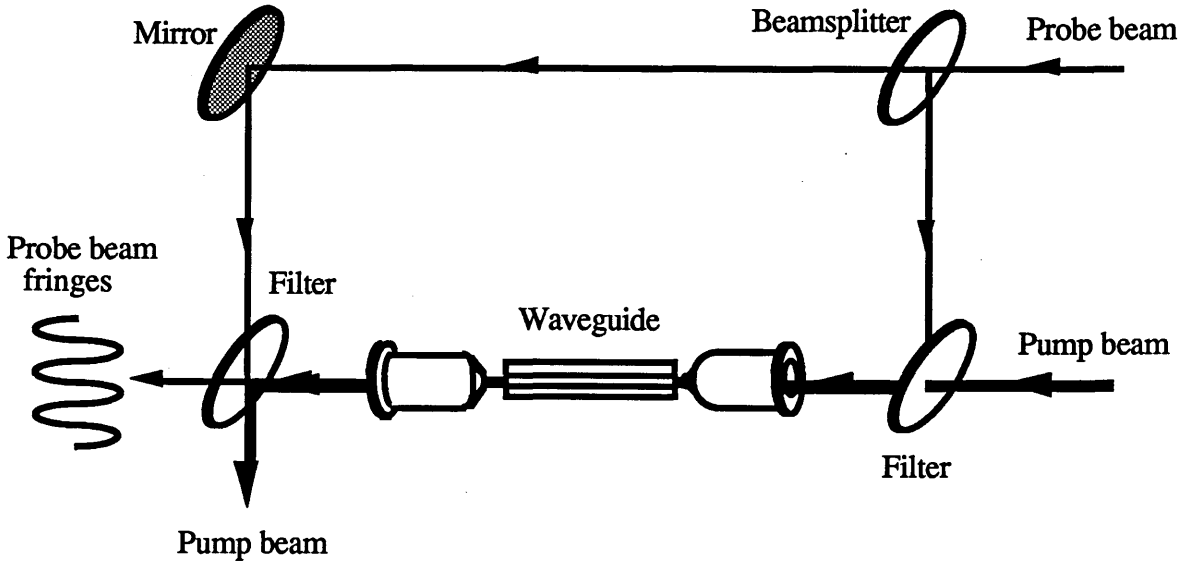

Fig. 7.2 Pump-probe Mach-Zehnder interferometer

In this case, it is assumed that the pump is of high enough intensity that it affects the waveguide's refractive index, while the probe is too weak to do so. The probe sees the change in refractive index caused by the pump, and this results in a shift in the fringe pattern of the probe. The pump can be removed by a filter (as shown in Fig. 7.2) if the pump and probe beams are at different wavelengths, or by a polariser if they are orthogonally polarised. When the intensity or wavelength of the pump is altered, the resultant change in refractive index can therefore be measured at the probe wavelength. If the wavelength of the probe can be altered, then the refractive index change spectrum can be measured. If the beams are pulsed and the pump-probe delay time is changed, then the dynamics of any refractive index changes can be studied, and hence their causes can be deduced.

7.2.2 INTERFEROMETRY EXPERIMENTS USING A PROBE BEAM OF WAVELENGTH CLOSE TO THE EXCITONIC RESONANCE

It was initially hoped to carry out experiments with an intense pump beam at 1.06 μm and a weaker, tunable probe continuum near the band edge. In this way, it would be possible to obtain a spectrum of the refractive index change, and it would be easier to measure the larger changes in refractive index near the exciton resonance. Experiments were considered using a semiconductor laser as the probe, but this was not tunable. It would also not have been easy to time-resolve any effect leading to a change in refractive index, as the pump and probe lasers could not be synchronously pumped.

The second method considered to obtain a tunable probe beam near the excitonic resonance was to generate a continuum in an optical fibre. This was done by frequency doubling part of the YAG laser beam in the optical fibre to 532 nm, and this green light was then scattered to longer wavelengths by means of thermal phonons. Fig. 7.3(a) shows the optical fibre used for this purpose. Green light can be seen at the top of the drum, where the light at 1.06 μm entered the fibre, and there is yellow light leaving the fibre, after the green had been scattered to longer wavelengths. The photograph in Fig. 7.3(b) shows the spectrum of the visible light diffracted from one of the gratings inside the monochromator. Figs. 7.4(a) and (b) show spectra of the light leaving the fibre over different wavelength ranges. The visible spectrum was measured with a photomultiplier tube with an S-5 response (185-650 nm range), and the infrared spectrum with a Germanium photodiode. There is seen to be a small amount of light around the exciton resonance. However, after filtering to obtain a probe of sufficiently narrow wavelength range, splitting it at the beamsplitter and coupling into the guide, it was found that the output intensity from the waveguide was too small to be useful.

(a)

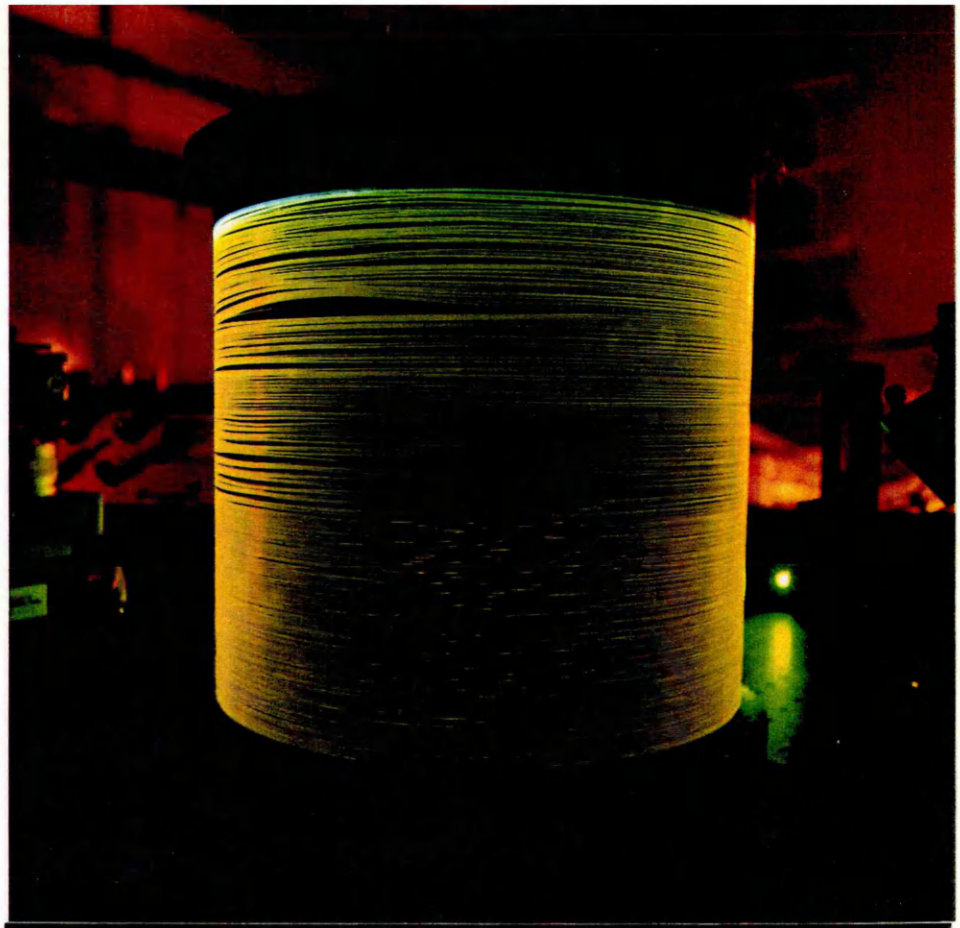

(b)

Fig. 7.3 Photographs of **(a)** the optical fibre used to frequency double the YAG laser beam and **(b)** the spectrum of the visible light leaving the fibre diffracted from one of the gratings inside the monochromator

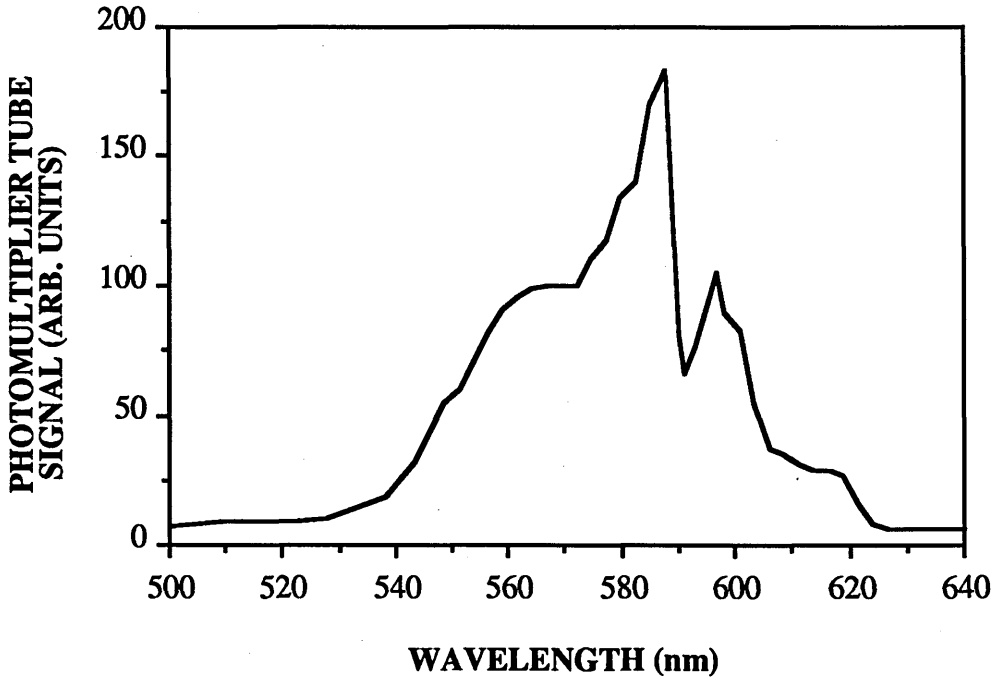

Fig. 7.4(a) Visible spectrum of the light leaving the fibre for a modelocked and Q-switched YAG laser beam at 1.06 μm as measured by a photomultiplier tube

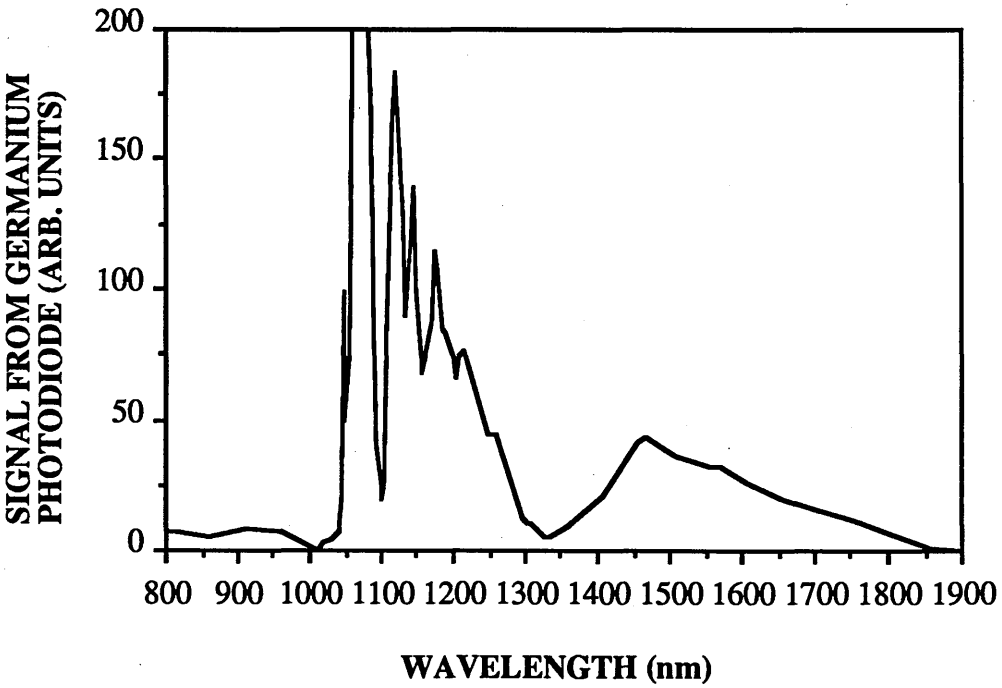

Fig. 7.4(b) Infrared spectrum of the light leaving the fibre for a modelocked and Q-switched YAG laser beam at 1.06 μm as measured by a Germanium photodiode

The other difficulty with this method was that it was necessary to use the YAG laser modelocked and Q-switched, because second-harmonic generation in silica fibres (see Section 1.8.3) is such a weak process *(Farries et al. 1987)*. This meant that the peak intensity of the modelocked pulses was not constant, but varied periodically. This would have resulted in difficulties when analysing any fringe shifts.

Because of the problems mentioned above, it was decided to use light at 1.064 μm for both the pump and probe beams, at least initially. At first, the interferometer was set up as in Fig. 7.2 in order to measure the change in refractive index in the waveguides used for the nonlinear absorption experiments of Chapter 5. The pump and probe beams were both at 1.064 μm and orthogonally polarised, and they were separated by a polarising beam-splitter cube. The two arms of the interferometer were aligned very carefully, and one of the mirrors was mounted on a translation stage. This was then adjusted so that the probe pulses travelled exactly the same distance through each arm, in order to optimise the fringe contrast. The output objective lens was defocussed, so that the image of the guided mode from the waveguide was about the same area and intensity as the beam which travelled through the other arm of the interferometer, as this also resulted in the maximum fringe contrast. The optical components were carefully mounted so as to be as stable as possible, and the table was pneumatically isolated from vibrations in the floor. It was also found to be necessary to suspend any choppers used so that they did not touch the optical table, as they caused vibrations in the apparatus.

7.2.3 MEASUREMENT OF FRINGE SHIFTS

There are several ways of measuring fringe shifts. An infra-red camera can be used to view the fringes, and the position of the fringes can be marked on the monitor both with and without the pump beam. This is very straightforward (if time-consuming), but it is not an accurate method for measuring the refractive index, and small fringe shifts cannot be measured, due to fringe instability.

The second method was to incorporate an electronic feedback loop into the interferometer, in order to stabilise the fringes and to measure the fringe shifts more accurately. This method has already been used successfully to determine both the magnitude and sign of refractive index changes *(Cotter et al. 1989* and *Jennings 1990)*. The control system as applied to the Mach-Zehnder interferometer is shown in Fig. 7.5.

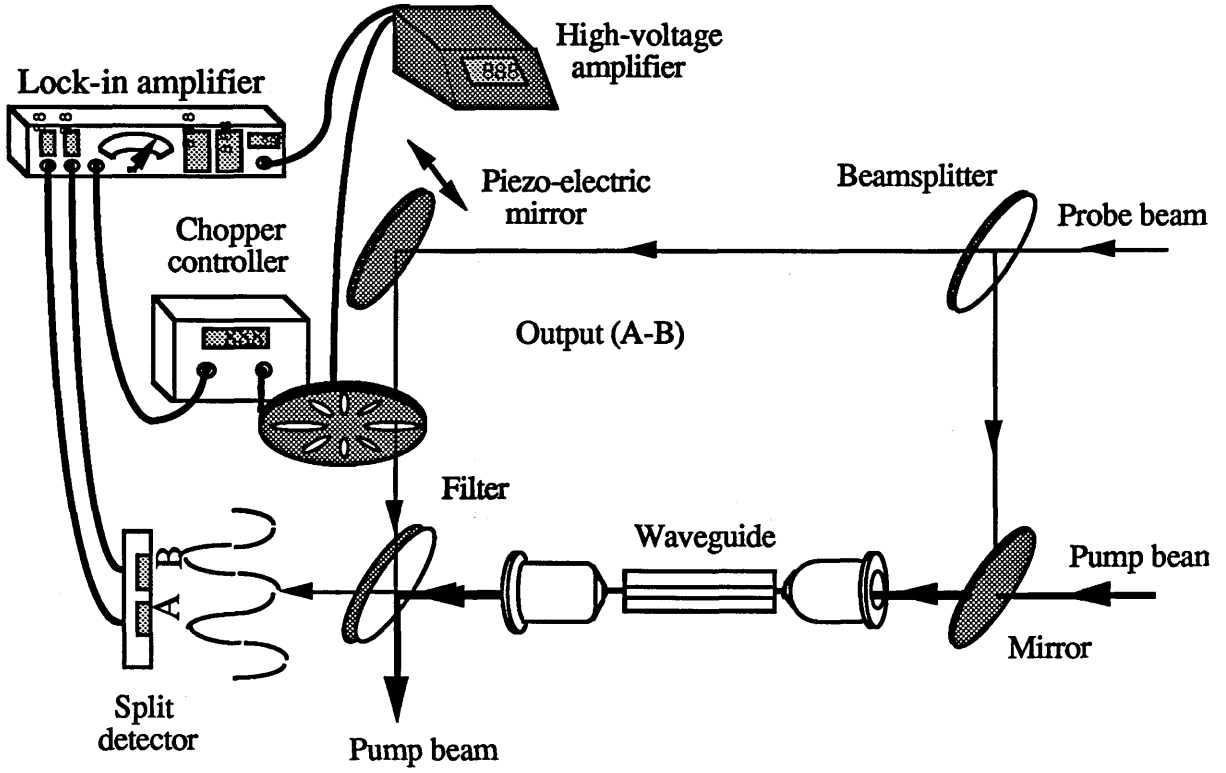

Fig. 7.5 Pump-probe Mach-Zehnder interferometer with feedback control loop

The split detector was a silicon photodiode, which consisted of two elements separated by 50 μm. The fringes were expanded onto this using a microscope objective so that adjacent maxima of the fringe pattern were positioned approximately at the outside edges of the two detectors, as shown in Fig. 7.5. This resulted in the maximum sensitivity of the circuit to any fringe shift *(Jennings 1990)*. The difference signal between the two detectors was first amplified with a lock-in amplifier, which also acted to eliminate any of the pump beam which might have been transmitted by the filter or polariser. This signal was then passed to the amplifier for the piezo-electric mirror control.

The detector was initially set up as in Fig. 7.5, so that the difference signal was A-B=0. If the fringe pattern moved, either due to a refractive index change in the waveguide or else due to random vibrations, then the difference signal became finite. This signal was amplified and fed back to the piezo-electric mirror, causing it to move in or out. This in turn affected the fringe pattern, and so altered the signal applied to the mirror. This process would continue until the difference signal from the detectors became zero again. The difference in path length of the reference arm of the interferometer must be equal to the difference in path length in the waveguide arm due to any change in refractive index. By measuring the difference voltage A-B applied to the piezo-electric mirror, the change in path length could be calculated, and hence the change in refractive index of the waveguide.

However, despite the control loop, there were still several problems with this type of interferometer. When a very intense pump pulse entered the waveguide, the fringe shift due to the thermal refractive index change was so large (of the order of 4π) that the feedback loop could not hold the fringe pattern steady, and jumped randomly between stable positions. There was also concern that an intense pump beam might warm up the objective lenses and the waveguide and so cause the coupling coefficient of the probe beam into the waveguide to be changed. This might lead to a change in the fringe pattern which would erroneously appear to be due to a change in the refractive index of the waveguide. Because of these considerations, it was decided to use time-division interferometry instead.

7.2.4 TIME-DIVISION INTERFEROMETRY

Time-division interferometry is a relatively novel technique for measuring refractive index changes *(LaGasse et al. 1989)*. In Fig. 7.5 the reference beam, which had been incident on the piezo-electric mirror, travelled through space, but in the time-division interferometer it travels through the waveguide, just like the pump and probe beams. In order for the pump to cause a shift in the fringes, the beams must all be pulsed, and the reference pulse must be well separated in time from the pump pulse. In this way, the reference beam is unaffected by the pump, and always sees the unperturbed refractive index of the waveguide. The pump and probe pulses overlap each other in time, so that the refractive index seen in the waveguide by the low-intensity probe is dependent on the intensity or relative temporal position of the pump pulse. In order to separate the beams from each other, the pump and reference are of the same polarisation, and the probe is orthogonally polarised.

Fig. 7.6 shows the interferometer as it was eventually used. At first, problems were encountered because the polarising beam-splitter cubes were only 99% efficient, so that some of the pump beam was incident on the split detector. Because the intensity of the pump was so much greater than that of the probe or reference, there was some nonlinear absorption in the photodiode itself, despite it being reverse-biased. This was discovered when the waveguide was removed from the end-fire rig, and the pump intensity was changed. There was an apparent shift in the fringes, but this was caused by the photodiode signal changing due to nonlinear absorption in the diode, not because of a real fringe shift.

In order to overcome this, the angle at which the reference entered the input objective was slightly altered, so that the reference beam was coupled into a rib adjacent

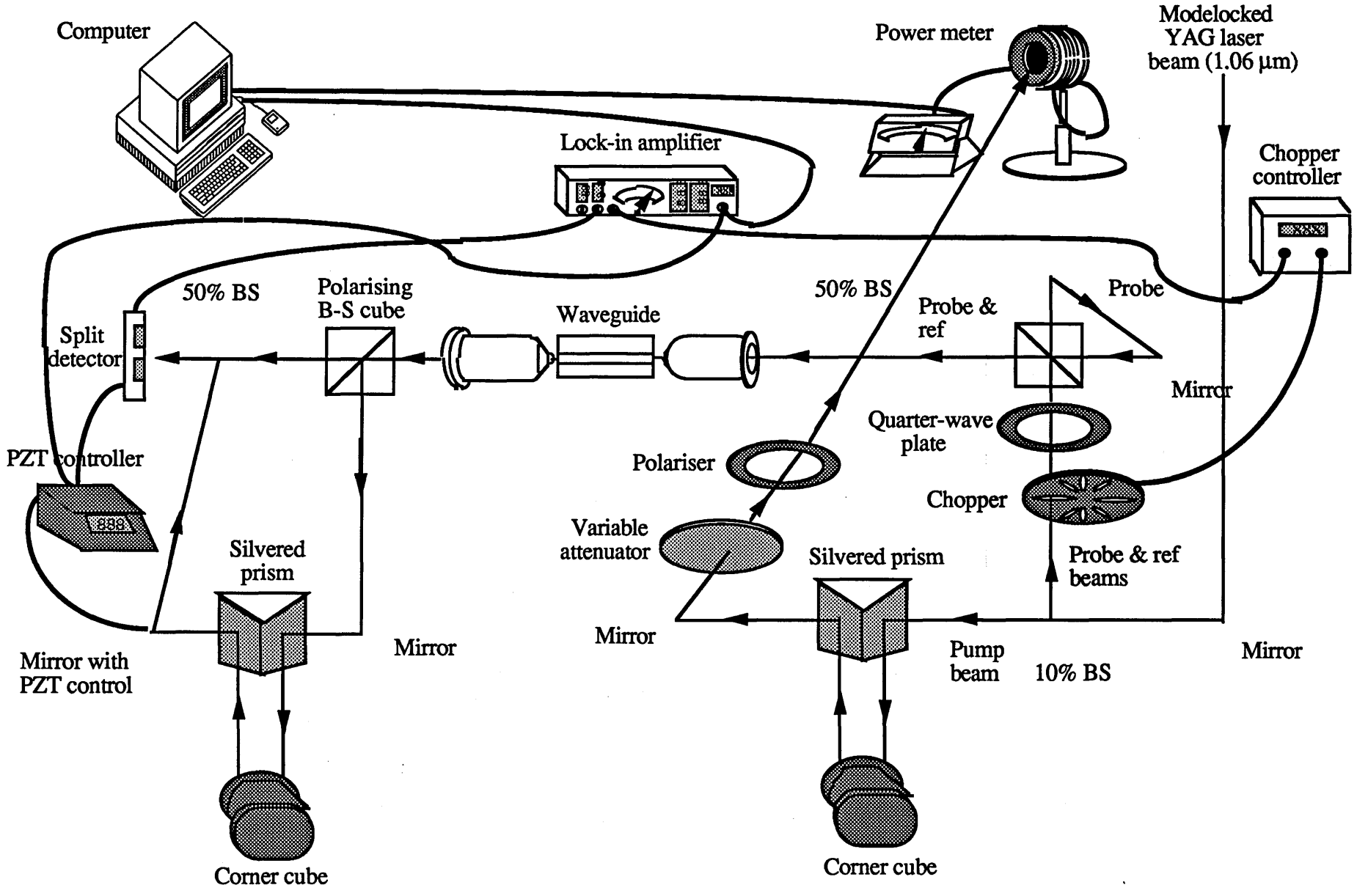
Computer
Power meter
Modelocked
YAG laser
beam (1.06 μm)
Lock-in amplifier
Chopper
controller
50% BS
Polarising
B-S cube
Waveguide
50% BS
Probe
Probe &
ref
Split
detector
Mirror
Quarter-wave
plate
PZT controller
Polariser
Chopper
Variable
attenuator
Silvered
prism
Silvered prism
Probe & ref
beams
Mirror
Mirror
Pump
beam
10% BS
Mirror
Mirror with
PZT control
Corner cube
Corner cube

to the rib into which the pump and probe beams were coupled. When the pump and reference beams were reflected by the polarising beam-splitter cube at the output of the waveguide, they were then spatially separated, and the pump spot could be deflected. There was still a small fraction of the pump beam which was coupled via slab guiding between the ribs into the guided mode of the reference beam's rib, but filters could be placed before the photodiode in order to reduce its intensity until the nonlinear effects in the photodiode were eliminated.

7.3 NONLINEAR REFRACTIVE INDEX MEASUREMENTS

In order to measure the change in refractive index due to the pump pulse, the experiment shown in Fig. 7.6 was set up. A 1 Hz chopper was placed in the pump beam, and so the refractive index in the waveguide varied with a frequency of 1 Hz. The pump intensity was measured at the output of the waveguide, and the photodiode difference signal A-B was also measured, as this is proportional to the fringe shift. It was found that the difference signal also had a periodic frequency of 1 Hz, but that it was out of phase with the pump intensity, i.e. as the pump turned on, the difference signal fell, and vice versa.

The probe chopper operated at about 400 Hz, and the lock-in amplifier was set with a time constant of 30 ms, and maximum amplitude 100 μV. The time constant and gain of the lock-in amplifier were found to be critical in order to avoid the two extremes of either the feedback loop not responding quickly enough to the pump, or the fringe pattern becoming unstable and oscillating. The computer was used to measure simultaneously the pump signal and the photodiode difference signal. After a reading had been taken, the delay line was moved by 0.5 mm, and another reading taken. This process was repeated for the entire 50 mm of the delay line. Fig. 7.7 shows an example of the raw data from this process.

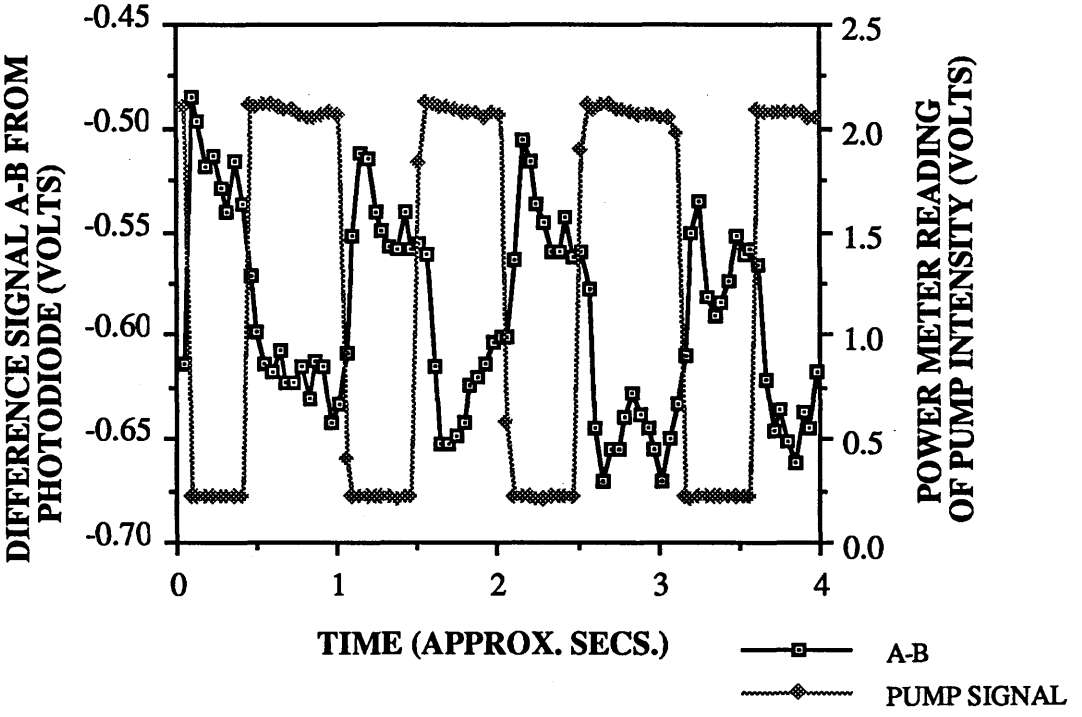

Fig. 7.7 Graph of the pump intensity and the photodiode difference signal as a function of time

In order to convert this data to the change in refractive index, the feedback loop was disconnected. An external varying voltage was applied directly to the piezo-electric amplifier, in exactly the same way that the photodiode difference signal had been applied during the experiments. The lock-in amplifier was used to measure just one of the two detectors, so that the intensity of the fringe pattern was constantly monitored at that position. As the external voltage was ramped, the piezo-electric mirror moved in and out, so that the fringe pattern moved across the photodiode. Both the photodiode voltage which monitored this fringe pattern shift and the external applied voltage were simultaneously measured by the computer. The resulting plots are shown in Figs. 7.8 and 7.9, and it can be seen that the phase change in the fringe pattern is proportional to the voltage applied to the piezo-electric amplifier.

When the pump beam was turned on, it was seen that the difference voltage A-B, which was applied to the piezo-electric amplifier in order to restore the fringe pattern to its original position, decreased. The piezo-electric amplifier was designed such that when the voltage applied to it decreased, the mirror moved out. This means that the feedback loop acted in such a way as to decrease the path length in that interferometer arm. Hence, when the pump beam was turned on, the refractive index of the waveguide decreased.

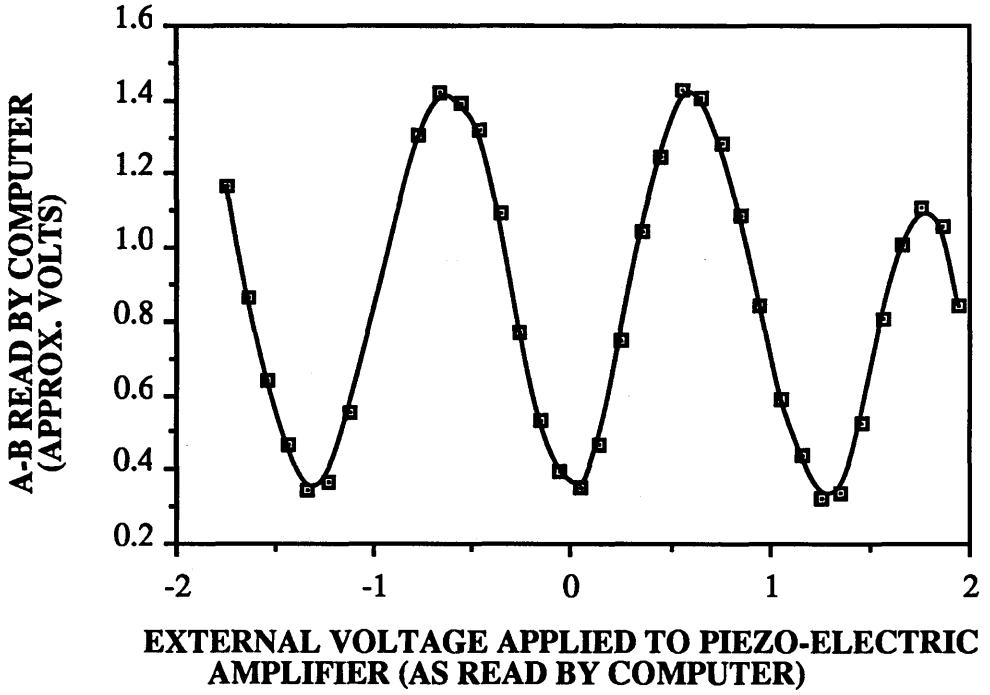

Fig. 7.8 Calibration plot for an external voltage applied to the piezo-electric amplifier.

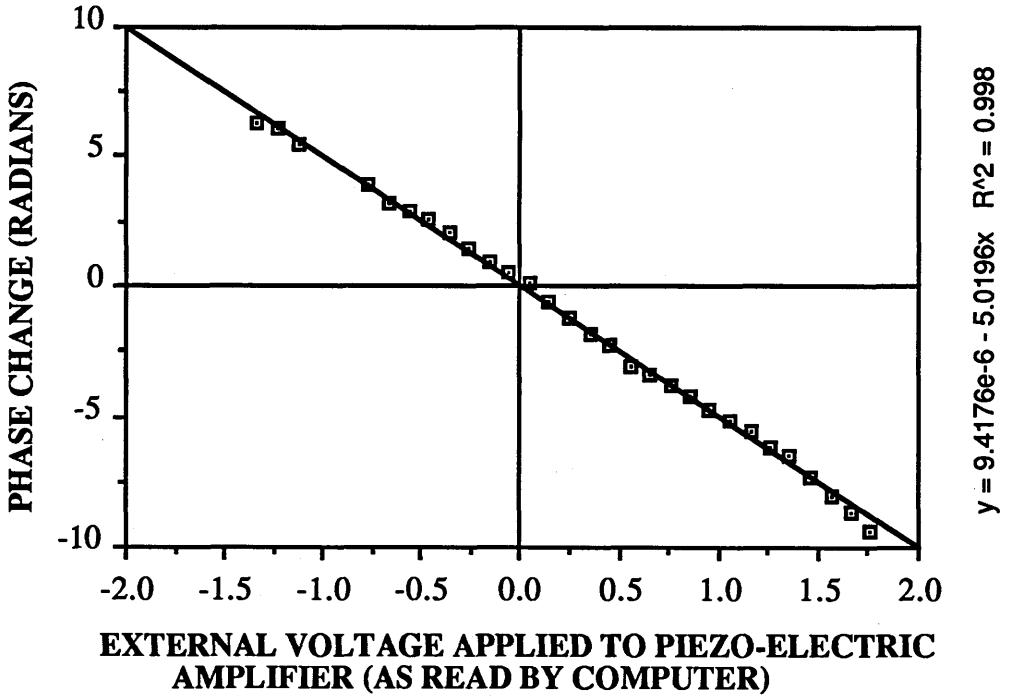

Fig. 7.9 Calibration plot of external applied voltage against phase for the piezo-electric amplifier

Fig. 7.10 shows the resulting plot of the nonlinear phase change $\Delta\psi$ as a function of the pump-probe delay time for a peak input pump intensity of about $1.5\text{x}10^{12}$ Wm^{-2}.

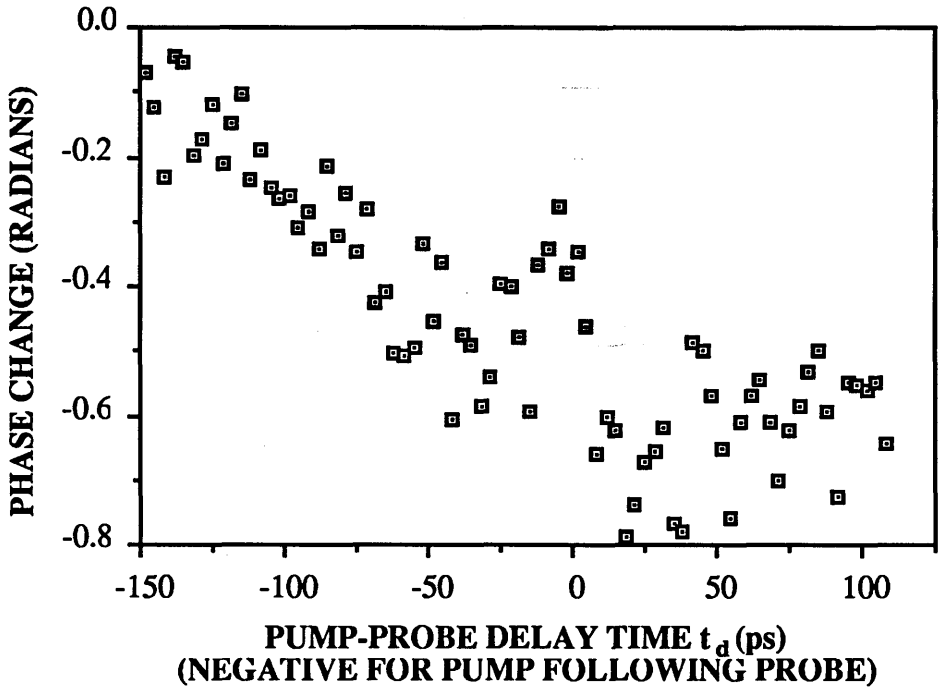

Fig 7.10 Nonlinear phase change for a peak input pump intensity of $1.5\text{x}10^{12}$ Wm^{-2}.

When the pump follows the probe by about 150 ps, the nonlinear refractive index change is very small, and as t_d becomes less negative, the magnitude of the nonlinear phase change $|\Delta\psi|$ increases until $t_d \approx -25$ ps. At this point, $|\Delta\psi|$ begins to decrease, and continues to do so until the pump and probe beams exactly overlap in time. As t_d becomes positive, $|\Delta\psi|$ at first increases and then falls off for $t_d > 25$ ps. The maximum nonlinear phase change was about –0.8 rad, which corresponds to a nonlinear intensity-dependent refractive index of $n_2 \approx -3\text{x}10^{-17}$ m^2W^{-1} if an average peak pump intensity in the waveguide of about $5\text{x}10^{11}$ Wm^{-2} is assumed.

It had been assumed initially in Section 7.1 that any nonlinear refractive index changes were due solely to the change in plasma frequency caused by the free carriers generated by the pump beam. To test the validity of this assumption, Fig. 7.11 shows the graph of Fig. 7.10 replotted with a graph overlaid on it of $\Delta\psi$ against t_d, as calculated from Eqn. 7.9. To obtain this plot, the typical experimental values quoted in Section 7.1 were inserted into Eqn. 7.9, and it was found that $\Delta\psi \approx -0.145F$. The values used for the carrier lifetime and pulse separation were 35 ns and 13 ns respectively,

and by inserting these into Eqn. 5.30 or 5.32 to obtain values for F as a function of t_d, the dependence of $\Delta\psi$ on t_d could be calculated.

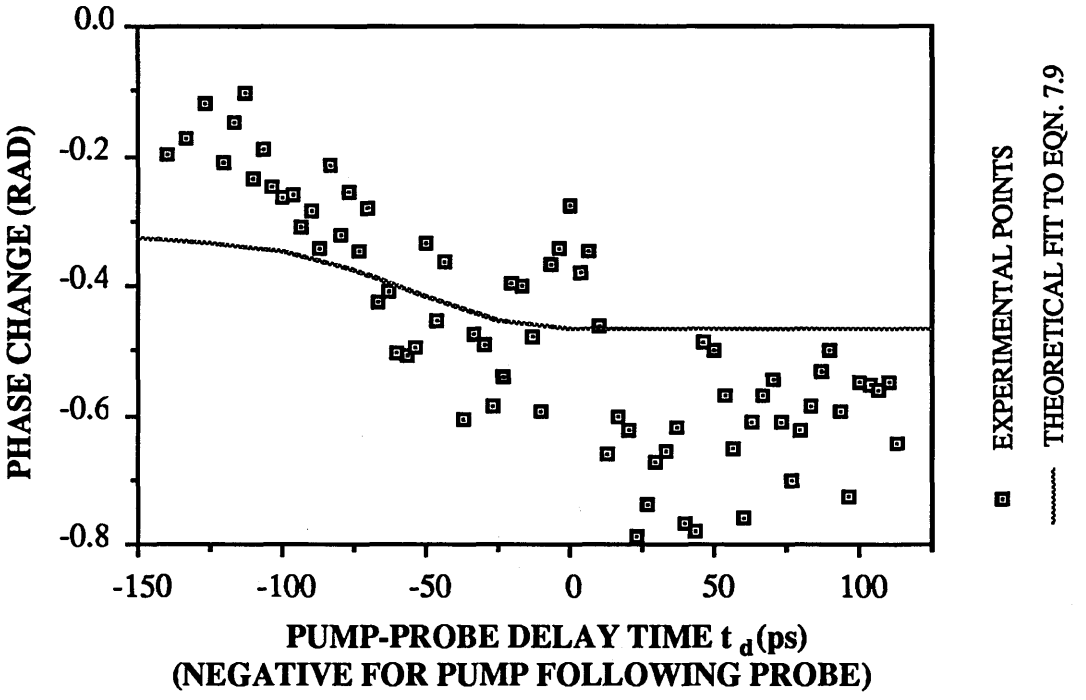

Fig. 7.11 Replot of Fig. 7.10 with the fit to Eqn. 7.9 overlaid

Fig. 7.11 shows that Eqn. 7.9 does not provide a good fit to Fig. 7.10, and so the assumption that $\Delta\psi$ is caused solely by the change in plasma frequency due to the photogenerated free carriers must be false. The other possible cause of $\Delta\psi$ mentioned in Section 7.1 is the Kramers-Krönig relations (see Section 1.4), which state that any change in absorption leads to a corresponding change in the refractive index. At any particular frequency, the change in refractive index will be proportional to the change in absorption coefficient. The proportionality factor will be a function of the integral of the change in absorption spectrum, and so cannot be evaluated for this experimental data, as the changes in absorption coefficient and refractive index are known only at a single photon frequency.

Fig. 7.12 shows the superimposition of the nonlinear phase change data of Fig. 7.10 onto the nonlinear absorption change data of Fig. 6.12, which has been divided by –80. Both sets of data were taken for a peak input pump intensity of 1.5×10^{12} Wm^{-2}.

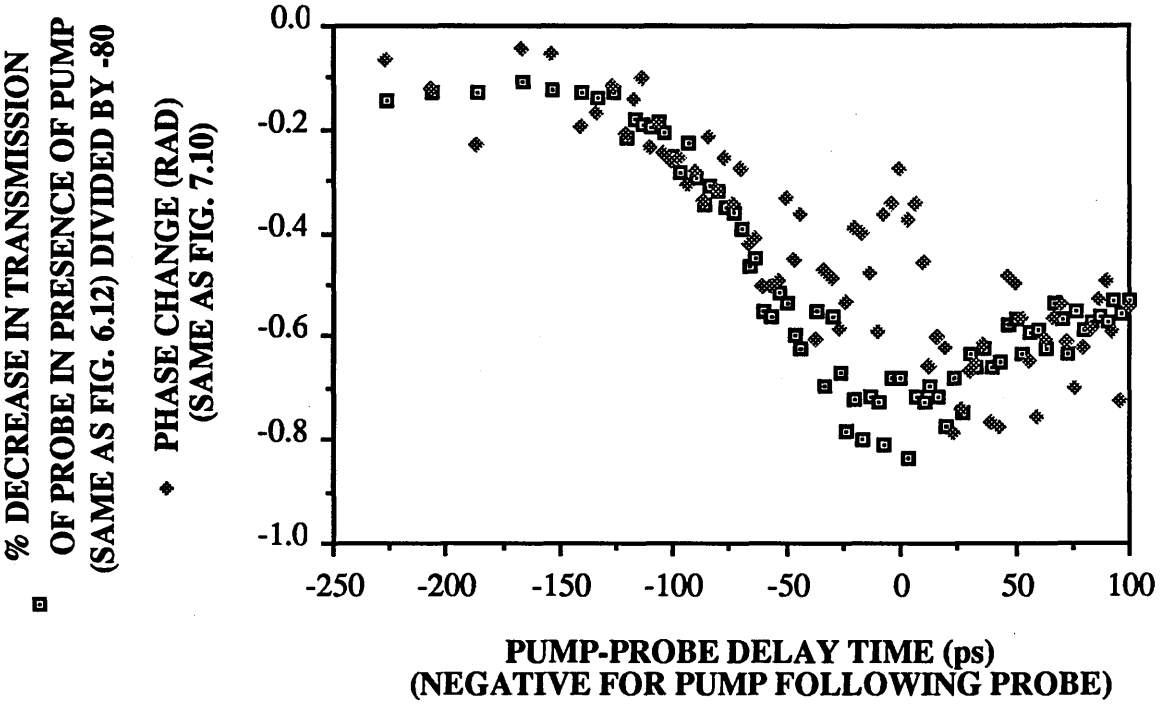

Fig. 7.12 Copy of Fig. 7.10 overlaid with the data of Fig. 6.12 divided by -80.

This graph shows that the nonlinear change in refractive index is proportional to the nonlinear change in absorption, except when the pump and probe pulses nearly overlap in time. This can be seen more clearly in Fig. 7.13, a graph of the difference between the sets of data points shown in Fig. 7.12 against the delay time between the pump and probe pulses.

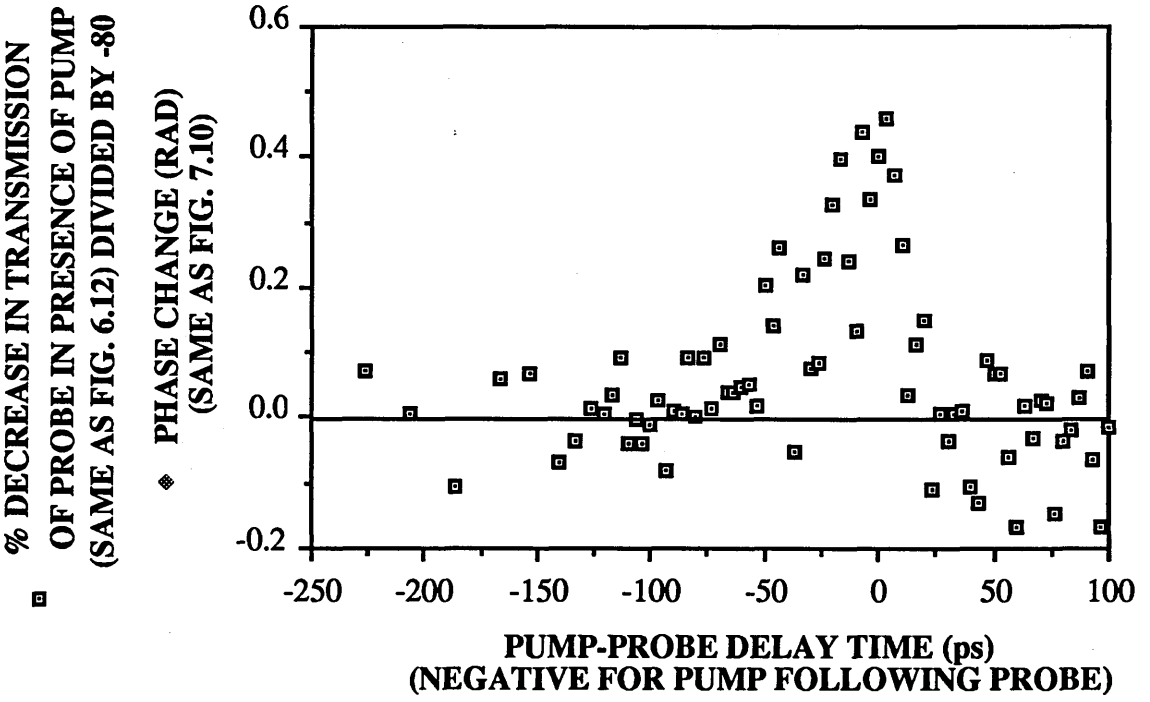

Fig. 7.13 Graph of the difference between the two sets of data points in Fig. 7.12.

When the pump and probe pulses are close together in time, there appears to be an additional positive component to the nonlinear phase change, which partially cancels out the negative nonlinear phase change due to the Kramers-Krönig transformation of the nonlinear absorption change. The maximum of this positive component occurs when the pump and probe pulses overlap. At this point, the nonlinear phase change is about 0.5 rad, implying that $n_2 \approx 2 \times 10^{-17}$ m^2W^{-1} if an average peak pump intensity in the waveguide of about 5×10^{11} Wm^{-2} is assumed.

There are several possible explanations for this positive component. It could be caused by coherence effects caused by the pump and probe pulses overlapping and interfering with each other inside the waveguide. Coherence effects are however unlikely to be the explanation, as the pump and probe beams were orthogonally polarised, and so would not interfere with each other. If the beams were interfering with each other, the nonlinear refractive index data would also be expected to be very noisy when the pump and probe pulses were close to each other in time, and it can be seen from Fig. 7.10 that this was not the case.

A second possible explanation is an ultrafast virtual effect, which leads to an increase in refractive index at small pump-probe delay times, such as the ac Quantum Confined Stark Effect (ac QCSE). This effect is seen as a blue shift in the exciton resonances and the Kramers-Krönig relations can be used to find the corresponding change in refractive index. This is given by

$$\Delta n(\omega) = \frac{c}{\pi} \wp \int_0^\infty \frac{\Delta\alpha(\Omega)}{\Omega^2 - \omega^2} d\Omega \qquad (7.12)$$

The spectrum of the nonlinear absorption change caused by the ac QCSE was not measured, and so the nonlinear refractive index change at 1.06 μm could not be calculated directly for these particular experimental conditions. It was hoped to make an estimate of the expected magnitude and sign of $\Delta\psi$ due to the ac QCSE from the experimental data of *Von Lehmen et al. 1986*. For the experiments in this paper, the pump photon energy was 31 meV below the heavy-hole exciton resonance energy and the pump intensity was about 2 MW cm^{-2}. The spectrum of $\Delta\alpha L$ can be calculated from the differential transmission spectrum given in the paper, and is shown in Fig. 7.14.

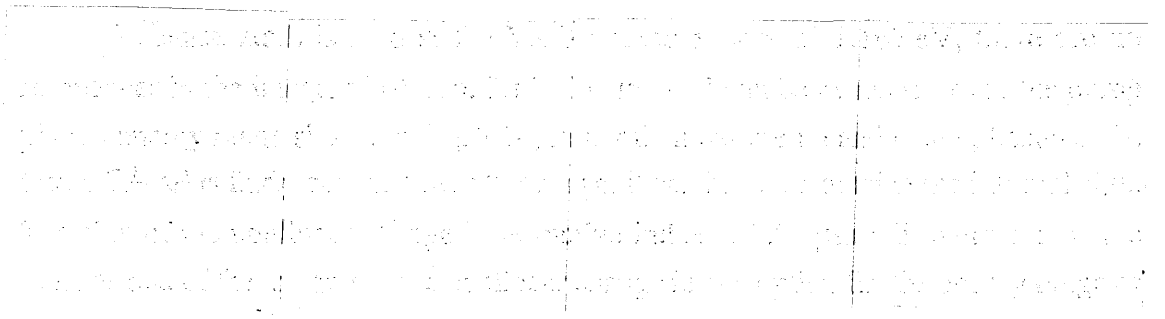

When Eqn. 7.12 was solved numerically using Simpson's Rule, it was found that for a YAG laser at 1.06 μm as both the pump and probe laser, and assuming an average intensity in the waveguide of $5x10^{11}$ Wm^{-2}, the expected intensity-dependent refractive index would be $n_2 \approx -2x10^{-17}$ m^2W^{-1}. This value is remarkable in the agreement between its magnitude and that of the positive component of the change in refractive index, but the sign is opposite.

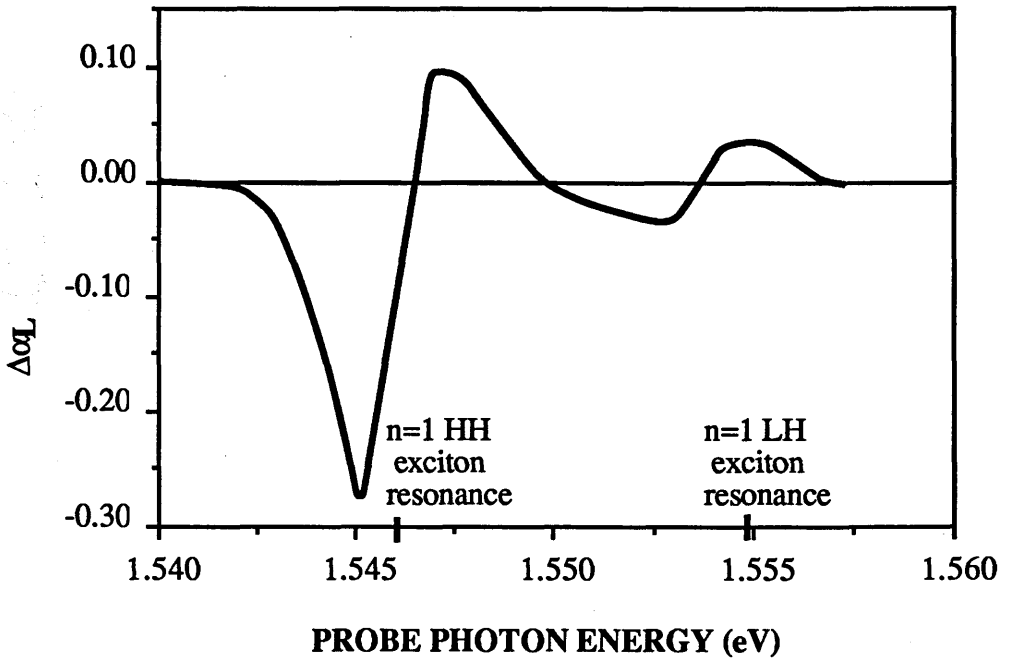

Fig. 7.14 Spectrum of the nonlinear absorption change ΔαL as calculated from the experimental data of *Von Lehmen et al.*

Since the ac QCSE leads to a blue shift in the exciton resonances, it always causes a negative change in the nonlinear refractive index for photon energies below the band gap. Therefore the positive component to the nonlinear change in refractive index in the experiments of this thesis could not be due to the ac QCSE.

Another possibility for the cause of the fast positive component is that there are two components to the nonlinear absorption change data of Fig. 6.12, that is the fast TPA (as seen in Fig. 6.11) and the longer lived effects of FCA, which only become apparent for higher intensities. It is quite possible that the proportionality factor linking the change in refractive index to the change in absorption coefficient spectrum would be different for TPA and FCA, and that the signs of these proportionality factors could be different. In this way, the intensity-dependent refractive index n_2 obtained from a Kramers-Krönig transform of the change in absorption coefficient spectrum for FCA could be negative, while that obtained for TPA could be positive.

Lastly, there will be intermediate states in the energy gap, such as the $EL2^+$ level, and it is not known what effect these energy levels might have on the intensity-dependent refractive index.

In order to ascertain the cause of the positive nonlinear refractive index change at small pump-probe delay times, it would be necessary to carry out further experiments using shorter laser pulses and different pump photon energies and intensities. In this way, the different responses of the longer-lived negative component and the shorter positive component of the nonlinear refractive index change could be distinguished, and the cause of the positive component identified.

7.4. SUMMARY OF CHAPTER SEVEN

A conventional Mach-Zehnder interferometer was set up to measure nonlinear refractive index changes, but was found to be too unstable to measure small fringe shifts. An electronic feedback control loop was added but was also found to be unstable because the thermal refractive index changes in the waveguide were very large and the feedback loop caused the fringe pattern to jump randomly between stable positions.

Time-division interferometry experiments were then carried out, and the nonlinear refractive index change in the waveguide was time-resolved. It was found that the nonlinear refractive index change was negative and that, when the pump and probe pulses were separated in time by more than about 25 ps, it was proportional to the nonlinear absorption change for the same pump intensity. This implies that the nonlinear

refractive index change is related to the Kramers-Krönig transform of the nonlinear absorption change except at small pump-probe delay times.

When the pump and probe pulses are close together in time, it was found that the nonlinear refractive index change was positive. The positive and negative components to the nonlinear change in refractive index were separated and were found to be $n_2 \approx 2 \times 10^{-17}$ m^2W^{-1} and $n_2 \approx -3 \times 10^{-17}$ m^2W^{-1} respectively. Several possibilities were suggested for this positive component to the intensity-dependent refractive index change, but it was not possible to come to any firm conclusions as to its origin without carrying out further experiments.

CHAPTER EIGHT
SUMMARY AND CONCLUSIONS

The original intention for this work was to investigate nonlinear refractive index changes in GaAs/AlGaAs MQW waveguides, using a Nd^{3+}:YAG laser at 1.06 μm. This was because very few free carriers are photogenerated by one-photon absorption at this wavelength, so that nonlinearities involving virtual transitions dominate. The particular nonlinearity of interest was the ac Quantum Confined Stark Effect, as this is an ultrafast effect, and it was hoped that phase modulation could be observed with very little insertion loss.

However, when experiments were carried out, it was found that there was very strong two-photon absorption and free carrier absorption in the waveguides. Nonlinear transmission experiments were performed both for a single beam and for pump and probe beams, which enabled any nonlinear absorption changes to be time-resolved. A theoretical nonlinear absorption model was derived, to which the experimental results were found to fit closely.

Nonlinear phase modulation was also observed and it was concluded that the observed negative refractive index change was the Kramers-Krönig transform of the nonlinear absorption change, except for those delay times for which the pump and probe pulses were very close to each other in time. The maximum negative intensity-dependent refractive index was found to be $n_2 \approx -3 \times 10^{-17}$ m^2W^{-1}. When the delay time was very small there was a positive refractive index change, which had a maximum value of about $+9 \times 10^{-6}$. This corresponded to a value for the nonlinear refractive index coefficient of $n_2 \approx 2 \times 10^{-17}$ m^2W^{-1}. The cause of this positive nonlinearity was discussed but it was not possible to identify this with certainty without repeating the nonlinear refractive index experiments for different pump intensities, for the orthogonal pump polarisation and for shorter pump and probe pulses.

Two-photon absorption is generally cited as a problem for nonlinear switching devices *(Aitchison et al. 1990)*, but it has been seen in Fig. 6.11 that, for moderate input pump intensities of about 4.5×10^{11} Wm^{-2}, it is possible to obtain intensity modulation whose speed is limited only by the laser pulsewidth, not by the carrier lifetime. When the input pump intensity was about 1.5×10^{12} Wm^{-2}, the intensity modulation of the probe beam was greater, but the speed of the modulation was now much slower, as the higher pump intensity led to a much higher density of free carriers in the waveguide.

One possible device which could be envisaged to use two-photon absorption is a two-photon autocorrelator, which is shown in Fig. 8.1.

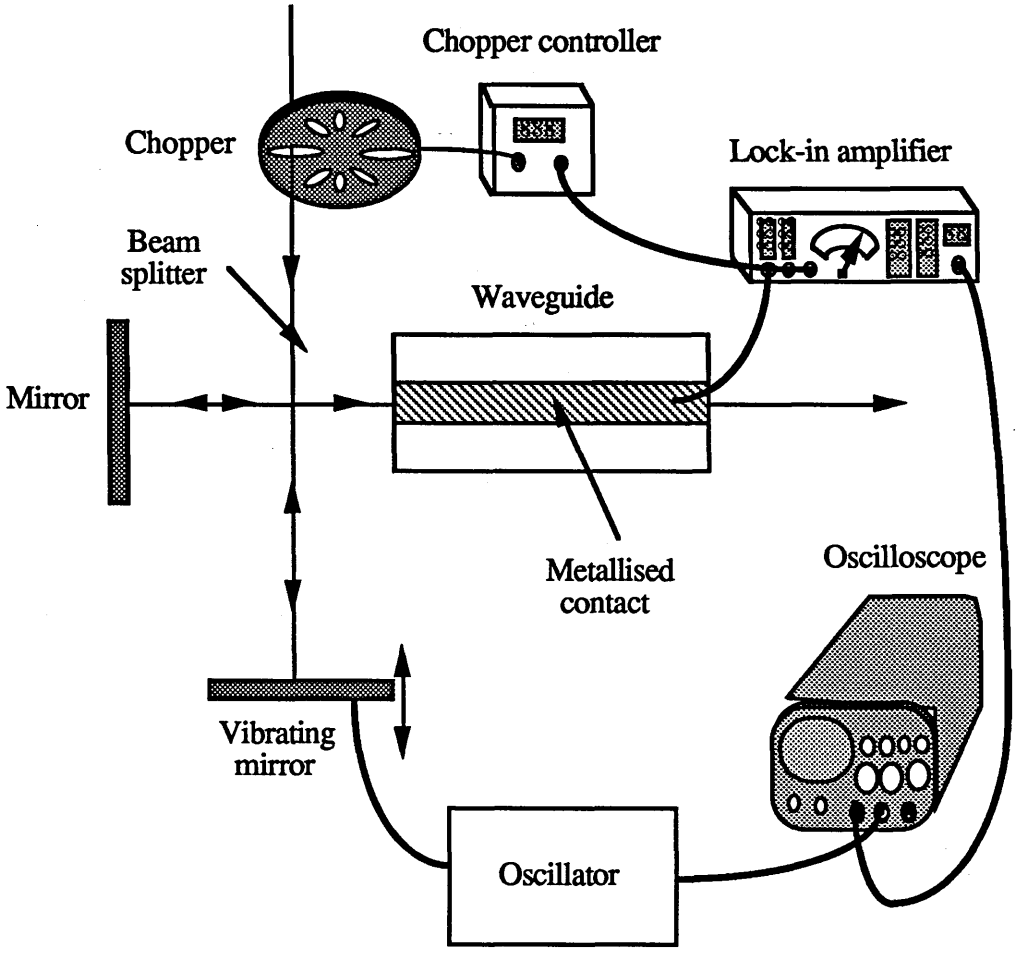

Fig. 8.1 Schematic of a two-photon autocorrelator

As the vibrating mirror moves in and out, the time delay between the pulses in each arm of the autocorrelator changes. The magnitude of the two-photon absorption in the waveguide is dependent on the instantaneous peak intensity present, and will be greatest when the two pulses exactly overlap. Since the number of free carriers in the waveguide is dependent on the amount of two-photon absorption, the photocurrent measured by the lock-in amplifier will also vary depending on the time delay between the pulses in each arm. The oscilloscope could be triggered by the oscillator used to vibrate the mirror, so that as the mirror moved in and out, a trace of the varying photocurrent could be displayed in real time on the oscilloscope. This trace would have the same shape as Fig. 6.11, and the laser pulsewidth could be determined from the width of the trace.

Further experiments in nonresonant optical nonlinearities could be carried out using an F-centre laser for which the photon energy is less than half the band gap, so

that there will be no two-photon absorption. In this case, the magnitude of n_2 will be similar to that seen at 1.06 μm but its sign will be positive *(Sheik-Bahae et al.1990)*. This is a very promising area for research, as the lack of two-photon absorption implies a lack of free carriers in the waveguide. This means that potentially large nonlinear refractive index changes could be achieved without any accompanying nonlinear absorption changes at this wavelength. Because there would be very few free carriers, the nonlinear refractive index changes could be very fast, as their speed would not be dependent on the carrier lifetime.

APPENDIX ONE

If there are two Gaussian pulses present in the waveguide, a pump and a probe then, as shown in Eqn. 5.24, the rate of change of intensity of the probe is given by

$$\frac{dI_{probe}}{dz} = -\alpha I_{probe} - \beta I_{probe}^2 - \beta I_{probe} I_{pump}(t_d) \tag{A1.1}$$

where I_{probe} is the intensity of the probe pulse and $I_{pump}(t_d)$ is the intensity of the pump beam as experienced by the probe beam which is separated from the pump by a time t_d. This pump beam intensity is an unknown function of both the peak intensity of the pump pulse and also the delay time between the pump and probe pulses. The purpose of this appendix is to find the form of this dependence, and this can be done by integrating the product of the pump and probe beams over time as shown below

$$\int_{-\infty}^{\infty} I_{pump}\, I_{probe}\, dt = \int_{-\infty}^{\infty} I'_{pump} \exp\left(\frac{-2\left(t-t_d^2\right)}{T^2}\right) I'_{probe} \exp\left(\frac{-2t^2}{T^2}\right) dt \tag{A1.2}$$

$$= I'_{pump}\, I'_{probe} \int_{-\infty}^{\infty} \exp\left(\frac{-2\left(\sqrt{2}\,t - \frac{1}{2}t_d\right)^2}{T^2}\right) \exp\left(\frac{-t_d^2}{T^2}\right) dt \tag{A1.3}$$

$$= \frac{\sqrt{\pi}}{2} T\, I'_{pump}\, I'_{probe} \exp\left(\frac{-t_d^2}{T^2}\right) \tag{A1.4}$$

As for the case of the nonlinear absorption of a single pulse, we assume that the probe intensity in Eqn. A1.1 can be written as the peak probe intensity I'_{probe}. Similarly, when $t_d=0$, we also assume that the pump intensity can be written as the peak pump intensity I'_{pump}. So when $t_d=0$, the rate of change of intensity of the probe is given by

$$\frac{dI'_{probe}}{dz} = -\alpha I'_{probe} - \beta I'^2_{probe} - \beta I'_{probe} I'_{pump} \tag{A1.5}$$

As seen from Eqn. A1.4, the product of the pump and probe intensities decays exponentially with delay time, so that for a delay time t_d between the pump and probe pulses, the rate of change of intensity of the probe beam can be written as

$$\frac{dI'_{probe}}{dz} = -\alpha I'_{probe} - \beta I'^{2}_{probe} - \beta I'_{probe} I'_{pump} \exp\left(\frac{-t_d^2}{T^2}\right) \qquad \text{(A1.6)}$$

This equation can then be integrated so that, if the peak input probe intensity is known, then the output probe intensity can be calculated as a function of either the peak pump intensity or the delay time between the pump and probe pulses.

APPENDIX TWO

The purpose of this appendix is to describe the working needed to solve the integral of Eqn. 5.41.

$$\text{Int} = \int \left(\alpha + \beta \, I'_{pump}(z) \exp\left(\frac{-t_d^2}{T^2}\right) + \gamma_1 \, I'^{2}_{pump}(z) \right) dz \tag{A2.1}$$

The first term can be easily solved:

$$\int \alpha \, dz = \alpha \, z \tag{A2.2}$$

The third term can be solved by assuming that the pump beam intensity decays due to linear and two-photon absorption only, so that there is no free carrier absorption. In this case,

$$\frac{dI'_{pump}(z)}{dz} = -\alpha I'_{pump}(z) - \beta I'^{2}_{pump}(z) \tag{A2.3}$$

so that the third term of the integral in Eqn. A2.1 can be written as

$$\int \gamma_1 \, I'^{2}_{pump}(z) \, dz = \int \gamma_1 \left(-\frac{1}{\beta} \frac{d \, I'_{pump}(z)}{dz} - \frac{\alpha}{\beta} I'_{pump}(z) \right) dz \tag{A2.4}$$

$$= -\frac{\gamma_1}{\beta} \int dI'_{pump}(z) - \frac{\gamma_1 \alpha}{\beta} \int I'_{pump}(z) \, dz \tag{A2.5}$$

$$= -\frac{\gamma_1}{\beta} I'_{pump}(z) - \frac{\gamma_1 \alpha}{\beta} \int I'_{pump}(z) \, dz \tag{A2.6}$$

The complete integral can now be written as

$$\text{Int} = \alpha z - \frac{\gamma_1}{\beta} I'_{pump}(z) - \left[\frac{\gamma_1 \alpha}{\beta} - \beta \exp\left(\frac{-t_d^2}{T^2}\right) \right] \int I'_{pump}(z) \, dz \tag{A2.7}$$

As we are assuming that the pump beam intensity decays only due to linear and two-photon absorption, it can be written as

$$I'_{pump}(z) = \frac{I'_{pump}(0) \; \alpha \; e^{-\alpha z}}{\alpha + \beta I'_{pump}(0) \; (1 - e^{-\alpha z})} \tag{A2.8}$$

By making a substitution $x=e^{-\alpha z}$ in the integral, it can therefore be shown that

$$\int I'_{pump}(z)\,dz = \frac{1}{\beta}\ln\left[\alpha + \beta I'_{pump}(0)\left(1-e^{-\alpha z}\right)\right] \tag{A2.9}$$

The full solution to the integral of Eqn. A2.1 has therefore been shown to be

$$Int = \alpha z - \frac{\gamma_1}{\beta} I'_{pump}(z) - \left[\frac{\gamma_1 \alpha}{\beta^2} - \exp\left(\frac{-t_d^2}{T^2}\right)\right] \ln\left[\alpha + \beta I'_{pump}(0)\left(1-e^{-\alpha z}\right)\right] \tag{A2.10}$$

This can then be substituted into the working of Chapter Five in order to solve the equations for the nonlinear absorption of a probe pulse due to the presence of a pump pulse.

REFERENCES

A. Abragam (1961), *Principles of Nuclear Magnetism*, Clarendon.

S. Adachi (1985), "GaAs, AlAs and $Al_xGa_{1-x}As$: Material parameters for use in research and device applications", *J. Appl. Phys. 58*, p. R1.

M.A. Afromowitz (1974), "Refractive index of $Ga_{1-x}Al_xAs$", *Solid State Commun 15*, p. 59.

J.S. Aitchison, M.K. Oliver, E. Kapon, E. Colas and P.W.E. Smith (1990), "Role of two-photon absorption in ultrafast semiconductor optical switching devices", *Appl. Phys. Lett. 56*, p. 1305.

B.J. Ainslie, H.P. Girdlestone and D. Cotter (1987), "Semiconductor-doped fibre waveguides exhibiting picosecond optical nonlinearity", *Electron. Lett. 23*, p. 405.

S.M. Al-Shukri, J. Duffy, R.M. De La Rue, M.N. Armenise, C. Canali and A. Carnera (1985), "Proton-exchange optical waveguides on lithium niobate: devices, characterisation and future prospects, *SPIE Vol. 578 Integrated Optical Circuit Engineering II*, p. 2.

D.E. Aspnes, S.M. Kelso, R.A. Logan and R. Bhat (1986), "Optical properties of $Al_xGa_{1-x}As$", *J. Appl. Phys. 60*, p. 754.

L.V. Azaroff and J.J. Brophy (1963), *Electronic processes in materials*, McGraw-Hill Book Company.

W.C. Banyai, N. Finlayson, C.T. Seaton, G.I. Stegeman, M. O'Neill, T.J. Cullen and C.N. Ironside (1989), "Saturation of the nonlinear refractive-index change in a semiconductor-doped glass channel waveguide", *Appl. Phys. Lett. 54*, p. 481.

G. Bastard, E.E. Mendez, L.L. Chang and L. Esaki (1982), "Exciton binding energy in quantum wells", *Phys. Rev. B. 26*, p. 1974.

J.H. Bechtel and W.L. Smith (1976), "Two-photon absorption in semiconductors with picosecond laser pulses", *Phys. Rev. B 13*, p. 3515.

P.R. Berger, Y. Chen, P. Bhattacharya, J. Pamulapati and G.C. Vezzoli (1988), "Demonstration of all-optical modulation in a vertical guided-wave nonlinear coupler", *Appl. Phys. Lett. 52*, p. 1125.

B.S. Bhumbra (1990), *Nonlinear optical waveguide devices in GaAs/AlGaAs*, Ph.D. thesis, Dept. of Electronics and Electrical Engineering, University of Glasgow.

A.M. Bonch-Bruevich and V.A. Khodovoi (1968), "Current methods for the study of the Stark Effect in atoms", *Sov. Phys. Usp.* ***10***, p. 71.

R.W. Boyd and M. Sargent (1988), "Population pulsations and the dynamic Stark effect", *J. Opt. Soc. Am.* ***5***, p. 99.

A.C. Bryce, J.H. Marsh, L.L.Taylor, S.J. Bass and D.R.P. Guy (1991), "Large modulation depth single-moded quantum well waveguide modulator operating around 1.57 μm", *Electron. Lett.* ***27***, p. 304.

K.C. Byron (1987), "Kerr modulation of signals at 1.3 and 1.5 μm in polarisation-maintaining fibres pumped at 1.06 μm", *Electron. Lett.* ***23***, p. 1324.

G.M. Carter, Y.J. Chen and S.K. Tripathy (1985), "Intensity dependent index of refraction in organic materials", *Optical Eng.* ***24***, p. 609.

H.C. Casey Jr., D.D. Sell and M.B. Panish (1974), "Refractive index of $Al_xGa_{1-x}As$ between 1.2 and 1.8 eV", *Appl. Phys. Lett.* ***24***, p. 63.

D.S. Chemla, D.A.B. Miller, P.W. Smith, A.C. Gossard and W. Wiegmann (1984), "Room temperature excitonic nonlinear absorption and refraction in GaAs/AlGaAs Multiple Quantum Well structures", *IEEE J. Quant. Electron.* ***QE-20***, p. 265.

D.S. Chemla and D.A.B. Miller (1985), "Room temperature excitonic nonlinear-optical effects in semiconductor quantum-well structures", *J. Opt. Soc. Am.* ***2***, p. 1155.

D.S. Chemla and D.A.B. Miller (1986), "Physics and applications of excitons confined in semiconductor quantum wells" in *Heterojunctions: Band discontinuities and device applications*, ed. G. Margaritondo and F. Capasso.

D.S. Chemla, S. Schmitt-Rink and D.A.B. Miller (1988), "Optical nonlinearities and instabilities in semiconductors", ed. H. Haug, New York: Academic.

Y.J. Chen, E.S. Koteles, B.S. Elman, S.W. Brown and G.J. Sonek (19??), "Multiple Quantum Well GaAs/AlGaAs waveguides for integrated optics", Proceedings of the 4th European Conference on Integrated Optics, Glasgow.

D. Cotter, C.N. Ironside, B.J. Ainslie and H.P. Girdlestone (1989), "Picosecond pump-probe interferometric measurement of optical nonlinearity in semiconductor-doped fibres", *Optics Lett.* ***14***, p. 31.

CRC Handbook of Chemistry and Physics, ed. R.C. Weast, S.M. Selby and C.D. Hodgman, Chemical Rubber Company.

T.J. Cullen, C.N. Ironside, C.T. Seaton and G.I. Stegeman (1986), "Semiconductor-doped glass ion-exchanged waveguides", *Appl. Phys. Lett.* ***49***, p. 1403.

R. Dalven (1980), *Introduction to Applied Solid State Physics*, Plenum Press.

U. Das, Y. Chen and P. Bhattacharya (1987), "Nonlinear effects in coplanar GaAs/InGaAs strained-layer superlattice directional couplers", *Appl. Phys. Lett.* ***51***, p. 1679.

J.H. Davies (1987), *Quantum mechanics course given to postgraduate students*, Dept. of Electronics and Electrical Engineering, University of Glasgow, to be published by the IOP.

J.H. Davies (1988), *Nonlinear Optics course given to M.Sc students*, Dept. of Electronics and Electrical Engineering, University of Glasgow, unpublished.

M. De Micheli and M. Papuchon (1985), "Nonlinear effects in $LiNbO_3$ waveguides", *SPIE Vol. 578 Integrated Optical Circuit Engineering II*, p. 150.

R.M. Eisberg (1964), *Fundamentals of Modern Physics*, John Wiley and Sons.

M.C. Farries, P. St. J. Russell, M.E. Fermann and D.N. Payne (1987), "Second-harmonic generation in an optical fibre by self-written $\chi^{(2)}$ grating", *Electron. Lett.* ***23***, p. 322.

N. Finlayson, W.C. Banyai, E.M. Wright, C.T.Seaton, G.I. Stegeman, T.J. Cullen and C.N. Ironside, "Picosecond switching induced by saturable absorption in a nonlinear directional coupler", *Appl. Phys. Lett.* ***53***, p. 1144.

A.P. French and E.F. Taylor (1979), *An introduction to quantum physics*, Thomas Nelson and Sons.

S.R. Friberg, Y. Silberberg, M.K. Oliver, M.J. Andrejco, M.A. Saifi and P.W. Smith (1987), "Ultrafast all-optical switching in a dual-core fibre nonlinear coupler", *Appl. Phys. Lett.* ***51***, p. 1135.

M. Goppert-Mayer (1931), "Über Elementarakte mit zwei Quantensprüngen", *Ann. Phys. (Leipz.)* ***9***, p. 273.

R.L. Greene and K.K. Baja (1983), "Binding energy of Wannier excitons in GaAs/$Al_xGa_{1-x}As$ Quantum Well structures", *Solid State Commun.* ***45***, p. 831.

N.J. Halas, D. Krökel and D. Grischkowsky (1987), "Ultrafast light-controlled optical-fibre modulator", *Appl. Phys. Lett.* ***50***, p. 886.

J.M. Hammer (1979), "Modulation and switching of light in dielectric waveguides" in *Integrated Optics*, ed. T. Tamir, Topics in Applied Physics, Springer-Verlag.

W.A. Harrison (1979), *Solid State Theory*, Dover Publications Inc.

H. Haug and S. Schmitt-Rink (1985), "Basic mechanisms of the optical nonlinearities of semiconductors near the band edge", *J. Opt. Soc. Am.* ***B2***, p. 1135.

H.A. Haus and N.A. Whitaker (1984), "All-optical logic in optical waveguides", *Phil. Trans. R. Soc. Lond.* ***A313***, p. 311.

H.A. Haus, N.A. Whitaker Jnr. and M.C. Gabriel (1985), "All-optical logic devices using Group III-V semiconductor waveguides", *SPIE Vol. 578 Integrated Optical Circuit Engineering II*, p. 122.

W.G. Herrenden-Harker and R.H. Williams (1986), "Epitaxial growth of GaAs: MBE and MOCVD" in *Gallium Arsenide for devices and integrated circuits*, ed. H. Thomas, D.V. Morgan, B. Thomas, J.E. Aubrey and G.B. Morgan, IEE Electrical and Electronic Materials and Devices Series 3.

V.P. Hinkov, R. Opitz and S. Sohler (1988), "Collinear acoustooptical TM-TE mode conversion in proton exchanged Ti:$LiNbO_3$ waveguide structures", *J. Lightwave Tech.* ***6***, p. 903.

J.N. Hodgson (1970), *Optical Absorption and Dispersion in Solids*, Chapman and Hall.

M. Jaros (1989), *Physics and Applications of Semiconductor Microstructures*, Oxford Science Publications.

J.A. Jennings (1990), *Electro-optic effects in MQW GaAs/AlGaAs stripe waveguides*, Ph.D. thesis, Dept. of Electronics and Electrical Engineering, University of Glasgow.

R. Jin, C.L. Chuang, H.M. Gibbs, S.W. Koch, J.N. Polky and G.A. Pubanz (1988), "Picosecond all-optical switching in single-mode GaAs/AlGaAs strip-loaded nonlinear directional couplers", *Appl. Phys. Lett.* ***53***, p. 1791.

R. Jin, J.P. Sokoloff, P.A. Harten, C.L. Chuang, S.G. Lee, M. Warren, H.M. Gibbs, N. Peyghambarian, J.N. Polky and G.A. Pubanz (1990), "Ultrafast modulation with subpicosecond recovery time in a GaAs/AlGaAs nonlinear directional coupler", *Appl. Phys. Lett.* ***56***, p. 993.

W. Kaiser and C.G.B. Garrett (1961), "Two-photon excitation in $CaF_2:Eu^{2+}$", *Phys. Rev. Lett.* ***7***, p. 229.

I.C. Khoo and Y.R. Shen (1985), "Liquid crystals: nonlinear optical properties and processes", *Optical Eng* ***24***, p. 579.

Y. Kimura, K.-I. Kitayama, N. Shibata and S. Seikai (1986), "All-fibre-optic logic 'AND' gate", *Electron. Lett.* ***22***, p. 277.

C. Kittel (1976), *Introduction to Solid State Physics, 5th Ed.,* John Wiley & Sons.

H. Kogelnik (1979), "Theory of dielectric waveguides" in *Integrated Optics*, ed. T. Tamir, Topics in Applied Physics, Springer-Verlag.

U. Koren, T.L. Koch, H. Presting and B.I. Miller (1987), "InGaAs/InP multiple quantum well waveguide phase modulator", *Appl. Phys. Lett.* ***50***, p. 368.

M.J. LaGasse, D. Liu-Wong, J.G. Fujimoto and H.A. Haus (1989), "Ultrafast switching with a single-fibre interferometer", *Optics Lett.* ***14***, p. 311.

M.J. LaGasse, K.K. Anderson, H.A. Haus and J.G. Fujimoto (1989), "Femtosecond all-optical switching in AlGaAs waveguides using a time division interferometer", *Appl. Phys. Lett.* ***54***, p. 2068.

K.T. Lau, N. Bar-Chaim, I. Ury and A. Yariv (1984), "Direct modulation of semiconductor lasers at f>10 GHz", *Appl. Phys. Lett.* ***44***, p. 273.

H.Q. Le, H.K. Choi and C.A. Wang (1990), "Measurement of the two-photon absorption coefficient in a GaAs/AlGaAs quantum well laser", *Appl. Phys. Lett* ***57***, p. 212.

D.L. Lee (1986), *Electromagnetic principles of integrated optics*, John Wiley & Sons.

P. Li Kam Wa, J.H. Marsh, P.N. Robson, J.S. Roberts and N.J. Mason (1985), "Nonlinear propagation in GaAs/AlGaAs multiple quantum well waveguides", *Proc. SPIE* ***578***, p. 110.

G.F. Lipscomb, A.F. Garito and R.S. Narang (1981), "Exceptionally large linear electro-optic effect in the organic solid MNA", *J. Chem. Phys.75*, p. 1509.

O. Madelung (1981), *"Introduction to Solid-State Theory"*, Springer-Verlag.

D. Marcuse and C. Lin (1981), "Low dispersion single-mode fibre transmission- the question of practical versus theoretical maximum transmission bandwidth", *IEEE J. Quant. Electron. QE-17*, p. 869.

A. Miller, D.A.B. Miller and S.D. Smith (1981), "Dynamic nonlinear optical processes in semiconductors", *Advances in Phys. 30*, p. 697.

V. Mizrahi, K.W. DeLong, G.I. Stegeman, M.A. Saifi and M.J. Andrejco, "Two-photon absorption as a limitation to all-optical switching", *Optics Lett. 14*, p. 1140.

T. Morioka, M. Saruwatari and A. Takada (1987), "Ultrafast optical multi/demultiplexer utilising Optical Kerr Effect in polarisation-maintaining single-mode fibres", *Electron. Lett. 23*, p. 453.

T.S. Moss, G.J. Burrell and B. Ellis (1973), "*Semiconductor opto-electronics*", Butterworths.

S. Ohke, T. Vmeda and Y. Cho (1985), "Optical waveguides using GaAs-AlGaAs Multiple Quantum Wells", *Optical Commun. 56*, p. 235.

M. Ali Omar (1975), *Elementary Solid State Physics*, Addison-Wesley.

M. Papuchon (1990), "High-speed modulators and switches in $LiNbO_3$", *Proceedings of the NATO ASI: International Summer School in Waveguide Optoelectronics, Glasgow*, to be published by Kluwer Academic Publications.

R.V. Penty, I.H. White and A.R.L. Travis (1988), "Nonlinear, two-moded, single-fibre, interferometric switch", *Electron. Lett. 24*, p. 1338.

N. Peyghambarian, H.M. Gibbs, J.L. Jewell, A. Antonetti, A. Migus, D. Hulin and A. Mysyrowicz (1984), "Blue shift of the exciton resonance due to exciton-exciton interactions in a Multiple-Quantum Well structure", *Phys. Rev. Lett. 53*, p. 2433.

RS Data Sheet (1987), *Peltier Effect heat pumps*, no. 7562.

H. Sakaki, H. Kurata and M. Yamanishi (1988), "Novel Quantum-Well optical bistability device with excellent on/off ratio and high speed capability", *Electron. Lett. 24*, p. 1.

K.L. Sala, G.A. Kenney-Wallace and G.E. Hall (1980), "CW autocorrelation measurements of picosecond laser pulses", *IEEE J. Quant. Electron.* ***QE-16***, p. 990.

L.I. Schiff (1968), *Quantum Mechanics*, McGraw-Hill.

S. Schmitt-Rink and D.S. Chemla (1986), "Collective excitations and the dynamical Stark Effect in a coherently driven exciton system", *Phys Rev Lett* ***57***, p. 2752.

S. Schmitt-Rink, D.S. Chemla and D.A.B. Miller (1989), "Linear and nonlinear optical properties of semiconductor quantum wells", *Advances in Physics* ***38***, p. 89.

M. Sheik-Bahae, D.J. Hagan and E.W. Van Stryland (1990), "Dispersion and band-gap scaling of the electronic Kerr effect in solids associated with two-photon absorption", *Phys. Rev. Lett.* ***65***, p.96.

Y.R. Shen (1984), *The Principles of Nonlinear Optics*, John Wiley and Sons.

K. Shimoda (1986), *Introduction to laser physics*, Springer-Verlag.

A.E. Siegman (1986), *Lasers*, University Science Books.

P.W. Smith (1984), "Applications of all-optical switching and logic", *Phil. Trans. R. Soc. Lond.* ***A313***, p. 349.

W. Sohler (1990), "Second Harmonic Generation in $LiNbO_3$ optical waveguides", *Proceedings of the NATO ASI: International Summer School in Waveguide Optoelectronics, Glasgow*, to be published by Kluwer Academic Publications.

J. Sonek, J.M. Ballantyne, Y.J. Chen, G.M. Carter, S.W. Brown, E.S. Koteles and J.P. Salerno (1986), "Dielectric properties of GaAs/AlGaAs Multiple Quantum Well material", *IEEE J. Quant. Electron.* ***QE-22***, p. 1015.

H.N. Spector (1987), "Two-photon absorption in semiconducting quantum-well structures", *Phys. Rev. B.* ***35***, p. 5876.

G.I. Stegeman and C.T. Seaton (1985), "Nonlinear integrated optics", *J. Appl. Phys.* ***58***, p. R57.

K. Tai, J. Hegarty and W.T. Tsang (1987), "Observation of the Optical Stark Effect in InGaAs/InP Multiple Quantum Wells", *Appl. Phys. Lett.* ***51***, p. 152.

M. Thakur and D.M. Krol (1990), "Demonstration of all-optical phase modulation in polydiacetylene waveguides", *Appl. Phys. Lett.* ***56***, p. 1213.

S. Tolansky (1955), *An Introduction to Interferometry*, Longmans.

P.D. Townsend, G.L. Baker, N.E. Schlotter, C.F. Klausner and S. Eternad (1988), "Waveguiding in spun films of soluble polydiacetylenes", *Appl. Phys. Lett.* ***53***, p. 1782.

H.K. Tsang and I.H. White (1990), "Efficient InGaAsP/InP Multiple Quantum Well waveguide optical phase modulator", *Appl. Phys. Lett.* ***22***, p. 2285.

F. Urbach (1953), "The long-wavelength edge of photographic sensitivity and of the electronic absorption of solids", *Phys Rev.* ***92***, p. 1324.

G.C. Valley, T.F. Boggess, J. Dubard and A.L. Smirl (1989), "Picosecond pump-probe technique to measure deep-level, free-carrier and two photon cross sections in GaAs", *J. Appl. Phys.* ***66***, p. 2407.

E.W. Van Stryland, H. Vanherzeele, M.A. Woodall, M.J. Soileau, A.L. Smirl, S. Guha and T.F. Boggess (1985), "Two-photon absorption, nonlinear refraction, and optical limiting in semiconductors", *Opt. Eng.* ***24***, p. 613.

A. Villeneuve, M. Sundheimer, N. Finlayson, G.I. Stegeman, S. Morasca, C. Rigo, R. Calvani and C. DeBernardi (1990), "Two-photon absorption in InGaAlAs/InP waveguides at communications wavelengths", *Appl. Phys. Lett.* ***56***, p. 1865.

A. Von Lehmen, D.S. Chemla, J.E. Zucker and J.P. Heritage (1986), "Optical Stark Effect on excitons in GaAs quantum wells", *Opt. Lett.* ***11***, p. 609.

R.G. Walker (1985), "Simple and accurate loss measurement technique for semiconductor optical waveguides", *Electron. Lett.* ***21***, p. 581.

C. Weisbuch, R. Dingle, A.C. Gossard and W. Wiegmann (1981), "Optical characterisation of interface disorder in GaAs/AlGaAs multi-quantum well structures", *Solid State Commun.* ***38***, p. 709.

I.H. White, R.V. Penty and R.E. Epworth (1988), "Demonstration of the Optical Kerr Effect in an all-fibre Mach-Zehnder interferometer at laser diode powers", *Electron. Lett.* ***24***, p. 340.

I.H. White, H.K. Tsang and R.V. Penty (1990), "Measurement of polarisation dependent all-optical nonlinearity in GaAs/AlGaAs quantum well waveguides far from the bandedge", *Proc. SPIE **1216***, p. 20.

J. Wilson and J.F.B. Hawkes (1983), *Optoelectronics: An introduction*, Prentice-Hall International Series in Optoelectronics.

T. Wood (1990), "Electroabsorption modulators", *Proceedings of the NATO ASI: International Summer School in Waveguide Optoelectronics, Glasgow*, to be published by Kluwer Academic Publications.

A. Yariv (1985), *Optical Electronics*, Holt-Saunders.